INLAND INTENSIFICATION OF TROPICAL CYCLONES: THEORY, MODELING, AND CLIMATOLOGY

by

ANDREW MICHAEL THOMAS

(Under the Direction of JAMES MARSHALL SHEPHERD)

ABSTRACT

On occasion, tropical cyclones (TCs) have been shown to strengthen over land, provided that the land is warm and moist. The emergent hypothesis is that the moist surface provides sustaining latent heat flux (LHF) reminiscent of an oceanic environment (the "Brown Ocean Effect" or BOE). Chapter 1 provides a review of mechanisms associated with TC intensification over land and tests the BOE hypothesis using numerical simulations of idealized TCs with different levels of soil moisture availability (SMA). Afterwards, a more sophisticated experiment was conducted with additional SMA profiles and different roughness lengths (Chapter 2). SMA gradients are shown to have a large influence on precipitation. The sensitivity of accumulated precipitation to SMA is larger with enhanced friction. The maximum wind speed is more sensitive to differences in SMA under lower surface roughness.

In Chapter 3, the idealized simulations are reexamined to evaluate the structure, intensity, and precipitation mechanisms. Vortical hot towers and Vortex Rossby Waves are identified and describe the radial pattern of local wind maxima but fail to describe the steady state patterns. The wind-induced surface heat exchange (WISHE), while appealing as an explanation, needs to be modified to describe the BOE. It is shown that the BOE is a semi-stable state with condensational warming causing structural degradation to the outflow but maintaining the warm-core structure. The increase in LHF also enhances the precipitation.

TC Maintenance and Intensification (TCMI) is a generalized definition of TCs that strengthen or maintain intensity inland. While extratropical transition is a well-studied explanation for many cases, the BOE is a relatively new explanatory hypothesis for certain storms. In Chapter 4, a novel methodology is proposed to examine the TC record to improve climatological representation of such cases. Using IBTrACS, individual times of inland TCs were classified into TCMI and non-TCMI (weakening) events. The MERRA-2 dataset was applied to develop a prototypical machine-learning model to help diagnose future TCMI events. A list of possible TCMI storms for case studies in future analyses is provided. Two of these storms were examined for BOE attributes.

INDEX WORDS: tropical cyclones, brown ocean effect, WRF, climatology

INLAND INTENSIFICATION OF TROPICAL CYCLONES: THEORY, MODELING, AND CLIMATOLOGY

by

ANDREW MICHAEL THOMAS

BS, The Pennsylvania State University, 2015

MS, The Pennsylvania State University, 2017

A Dissertation Submitted to the Graduate Faculty of The University of Georgia in Partial Fulfillment of the Requirements for the Degree

DOCTOR OF PHILOSOPHY

ATHENS, GEORGIA

2021

INLAND INTENSIFICATION OF TROPICAL CYCLONES: THEORY, MODELING, AND CLIMATOLOGY

by

ANDREW MICHAEL THOMAS

Major Professor: J. Marshall Shepherd
Committee: Joseph A. Santanello
John A. Knox
Gabriel J. Kooperman

Electronic Version Approved:

Ron Walcott
Dean of the Graduate School
The University of Georgia
May 2021

DEDICATION

"Surely God is great, and we do not know him; the number of his years is unsearchable. For he draws up the drops of water; he distills his mist in rain, which the skies pour down and drop upon mortals abundantly."- Elihu

I would like to dedicate this dissertation to God, and let my work honor him more than it honors me. Amen.

ACKNOWLEDGEMENTS

Firstly, I would like to acknowledge my adviser, Dr. Shepherd, who brought me here to UGA under the NASA Modeling, Analysis, and Prediction (MAP) program (16-MAP16-013) grant, which I am thankful for. I would then like to thank my committee members, Dr. Santanello, Dr. Kooperman, and Dr. Knox, for agreeing to be on the committee and doing all of the work associated. Following the theme of advisors and teachers, I would like to thank all of my advisers, mentors, professors, and teachers, all the way from the Pocono Mountain School District to Penn State, to here at the University of Georgia that I have not mentioned. Perhaps I could write another dissertation on how you all helped me grow (but I doubt I could get that funding).

To my family, thank you so, so much. I know communication with me is not easy. Thank you for supporting me and my decision to move almost ~800 miles away and see me in person occasionally so that I could make it to this point. And this is not just immediate family, but also extended family, who I get to see even more sparingly nowadays.

I would also be remiss to not acknowledge those that I met here in Athens. These include (but are not limited to) those I met at UGA Wesley, Tuckston United Methodist Church, and here in the Geography department. You all have made my time here in Athens so much more bearable.

Table of Contents

LIST OF TABLES

Page

LIST OF FIGURES

Page

CHAPTER 1

Introduction

A. Impacts of Tropical Cyclones

Tropical cyclones (TCs) are one of the most expensive and expansive natural disasters that emerge from the atmosphere. Between 1900 and 2017, approximately $2 trillion (corrected after inflation) in damages were incurred from TCs within the United States (Weinkle et al. 2018), averaging $17 billion per year. Four common dangers of TCs are damaging winds, sea level rise due to the storm surge, flooding, and tornadoes. High winds are the primary metric used to classify TCs as tropical depressions, tropical storms and hurricanes, per the Saffir-Simpson scale. The storm surge is often the most destructive aspect of TCs but is primarily confined to coastal and near coastal areas (Needham et al. 2015). Flooding from TCs is often widespread and may occur in areas not directly susceptible to TCs (Kidder et al. 2005).

Tropical cyclones pose a variety of multifaceted hazards. Tropical cyclones have a detrimental effect on global Gross Domestic Product (Chan and Kepert 2010). This does not include the indirect costs such as the opportunity cost of labor and business, the increased price of mitigation strategies, or the need for insurance (Gray et al. 1986). Other costs, such as the loss of cultural or sentimental objects and icons (McKernan and Mulcahy 2008) and the psychological health of residents (Fussell and Lowe 2014; Lowe et al. 2009), may not be quantifiable. Even the cost of the evacuation of residents is not negligible (Lowe 2012). TCs pose a hazard for industrial accidents (Misuri et al. 2019), soil contamination (Casteel et al. 2006), ecological damage (Erickson et al. 2019) and influence quality of life through power outages or degradation of air and water quality (Manuel 2013). This may result in the avoidance of areas perceived to be more vulnerable to TCs (Hunter 2005), particularly coastal areas. The perception of coastal regions as being more prone to TC threats than inland regions is slightly illusory as the only hazards posed uniquely to the littoral region are the storm surge (the most destructive aspect of TCs) and high wind.

Inland flooding accounts for 50% (Rappaport 2000) to 80% (Czajkowski et al. 2011) of United States deaths (statistics from before 2011 and may not account for later storms such as Hurricane Sandy of 2012). Much of the property damage from flooding within the United States, as recorded by insurance claims, occurs inland (Czajkowski et al. 2017). Though as discussed above, insurance claims only consider the property damage of the insured and not of uninsured/excluded damages. Other sectors that are impacted by inland flooding include energy (Han et al. 2009), agriculture (Stewart and Berg 2019; Wood et al. 2001; Hiesl and Rodriguez 2019), transportation , infrastructure (Chisolm and Matthews 2012; Lin and Cha 2021), and medicine (Ryan et al. 2015).

B. Fate of Tropical Cyclones and Extratropical Transition

Tropical cyclone intensity, although unpredictable after 4-5 days (Kieu and Moon 2016), has a semi-predictable behavior in given situations. Often, TCs strengthen over warm waters with weak vertical wind shear. Conversely, strong wind shear (Frank and Ritchie 2001) and a dearth of surface moisture undermine the intensity (Kimball 2006). The premise is that wind shear disrupts the vertical structure of TCs, while the land is presumed to be dry. This process reduces the transport of moisture from the surface to the TC. If the TC does not dissipate, it eventually may undergo extratropical transition (ET), which is when the TC takes on characteristics of an extratropical cyclone.

Evans et al. (2017) and Keller et al. (2018) provide recent literature reviews regarding ET. ET occurs when a preexisting tropical cyclone interacts with a baroclinic environment or a preexisting midlatitude synoptic system. A TC undergoing ET may cause continuity problems for operational forecasting centers (Blake et al. 2013) as the hazards posed are similar to those of a TC, even if the structure does not reflect those hazards. Those hazards may be amplified by ET, and hazards may be generated downstream from ET (Grams and Blumer 2015). Characteristics of ET may be identified on satellite by the dissolution of symmetry and the characteristics of an extratropical system (such as the manifestation of fronts) (Jones et al. 2003). Another graphical though quantifiable way of identifying ET is through the use of Cyclone Phase Space (CPS) diagrams (Hart 2003), which applies the thermal wind of 900-600 hPa, the thermal wind of 600-300 hPa, and the cross-track thermal symmetry between 900-600 hPa for categorization. Evans et al. (2017) and Klein et al. (2000) describe ET as a three-step process: 1) initial contact with the baroclinic zone degrades the TC structure, expands the wind field and introduces asymmetry to the precipitation, 2) the TC becomes superimposed with the baroclinic zone, gaining vertical tilt and creating fronts and losing its warm core in the upper levels, and 3) the TC becomes a component of the extratropical cyclone as it loses its tropical structure, remaining as a low-level warm anomaly.

C. Background on the Brown Ocean Effect

Provided that a TC that is over land does not interact with a baroclinic zone to begin ET, it is presumed to decay over land. Generically, if ET does not occur and the TC, even temporarily, does not decay, it is considered to undergo Tropical Cyclone Maintenance or Intensification (TCMI, see Figure 1). While there may be various reasons why a TC may undergo TCMI, the topic of this dissertation is on what has become known as the “Brown Ocean Effect” (Andersen and Shepherd 2014; Andersen et al. 2013).

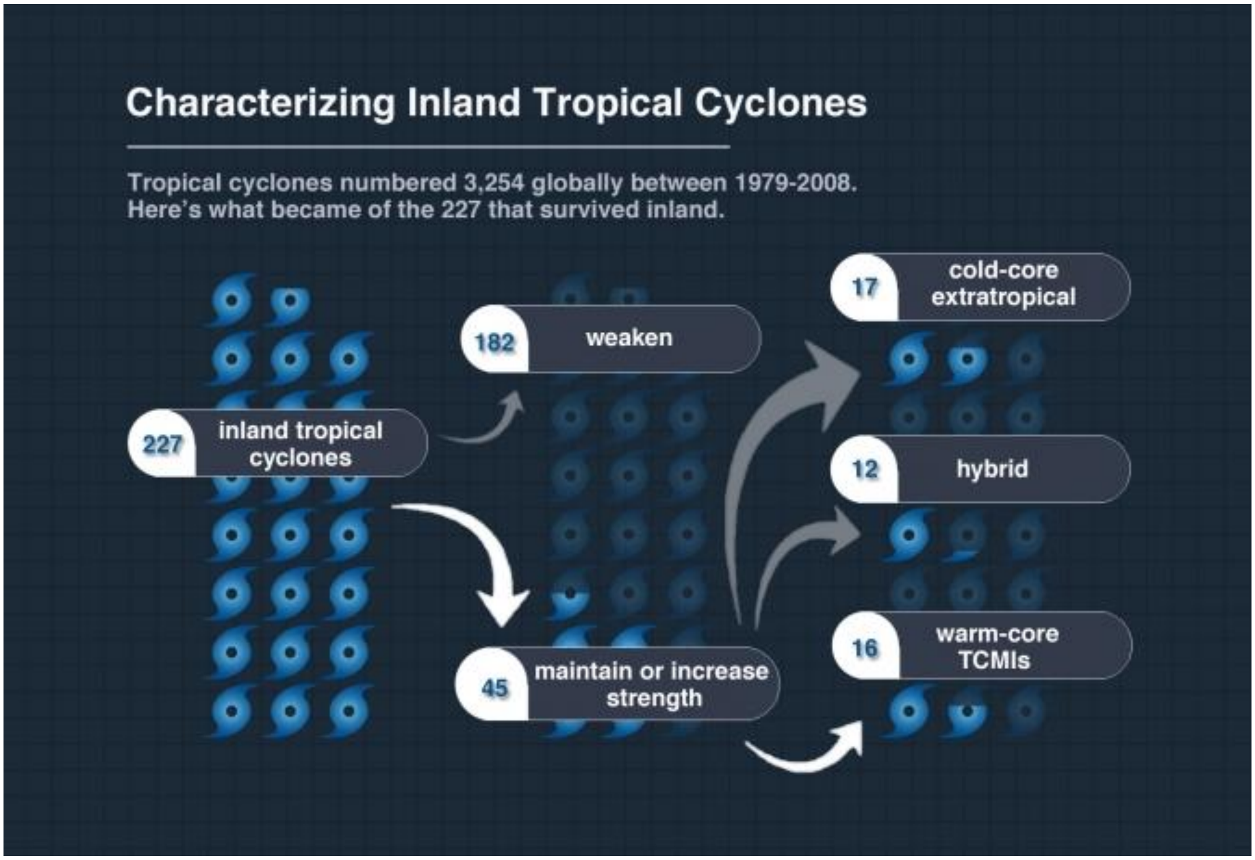

Figure 1: Schematic categorizing inland tropical cyclone fate. Image credit: NASA/Kathryn Hansen. Source: https://www.nasa.gov/content/goddard/brown-ocean-can-fuel-inland-tropical-cyclones/

The assumption that land weakens TCs hinges on the moisture available for evapotranspiration. Tuleya and Kurihara (1978) show that the soil moisture is the most important aspect in determining post-landfall decay. If the surface is sufficiently moist, the TC may still intensify or maintain intensity despite its geographic location (Shen et al. 2002; Andersen et al. 2013). Moreover, the change in the roughness of the surface may also strengthen the TC after landfall provided that the evaporation from the surface was not impacted (Tuleya and Kurihara 1978).

The “Brown Ocean Effect” may be summarized that in the proper environment, moist enthalpy fluxes may strengthen the TC beyond simply providing a source of moisture. The process of evaporating surface moisture to the TC, in turn, provides the enthalpy flux that enhances the storm strength. This is evident in the case of the agukabam, coined by Emanuel et al. (2008). Agukabams are TCs that are not intensified through a supply of moisture while over land but are instead invigorated by the sensible heat flux from the surface. This idea is supported by Mrowiec et al. (2011) which showed that a hurricane may be sustained without the presence of water vapor. The intensification due to the sensible heat flux complements the “Brown Ocean Effect.” Because the concept of the Agukabam relies on surface heat fluxes, it will be considered as part of the Brown Ocean Effect. In this way, the Brown Ocean Effect may be defined as the reintensification or maintenance of overland TCs due to surface enthalpy fluxes.

D. “Proof-of-Concept” Simulations

Since this concept is relatively new and many scholars are unaware of this phenomenon, a small, preliminary series of idealized simulations of TCs was conducted using the Weather Research and Forecasting (WRF) model. First, a control simulation was run for 6 days with the settings described by Table 1. Next, a “Dry Land” simulation was conducted by restarting the control simulation after three days of simulation time and replacing the ocean with land covered by deciduous trees and no available surface moisture. Finally, a “Brown Ocean Effect” simulation was conducted by replicating the “Dry Land” simulation but using a fully moistened surface. For these simulations, the land-surface model was turned off in order to allow the simulation a constantly moistened or dried surface at a constant temperature. The time period that was chosen was prior to the period of rapid intensification (RI) of the control simulation. RI is defined as the event or period where the maximum wind speed of the TC intensifies by 35 knots within one day.

Table 1: Model settings for "Proof-of-Concept" simulations.

Setting	Choice	Reference (if applicable)
Horizontal resolution	15 km	N/A
Microphysics	Kessler	Kessler 1969
Radiation	Capped Newtonian relaxation scheme	Rotunno and Emanuel 1987
Convection	None	N/A
Input profile	Default	Jordan 1958
Boundary Layer	YSU	Hong et al. 2006
Vertical layers	21	N/A
Land-Surface Model	None	N/A
Surface layer	MM5 Similarity scheme with alternate C_k/C_d over the ocean	Jiménez et al. 2012; Donelan et al. 2004

As expected, the aptly named "Brown Ocean Effect" simulation intensified, even in a pattern that is not so different from the control simulation, whilst the "Dry Land" simulation weakened accordingly. Figure 2 shows the maximum wind speed for each simulation. This "Proof-of-Concept" experiment indicates that the Brown Ocean Effect is certainly plausible, if not likely. These simulations were conducted with physics options that were not necessarily the most accurate but were optimized for speed and lower computational costs. Yet, they were still able to produce a TC. One of the major influences on the strength of the TC was likely the horizontal resolution (Gentry and Lackmann 2010), which in future simulations will be corrected.

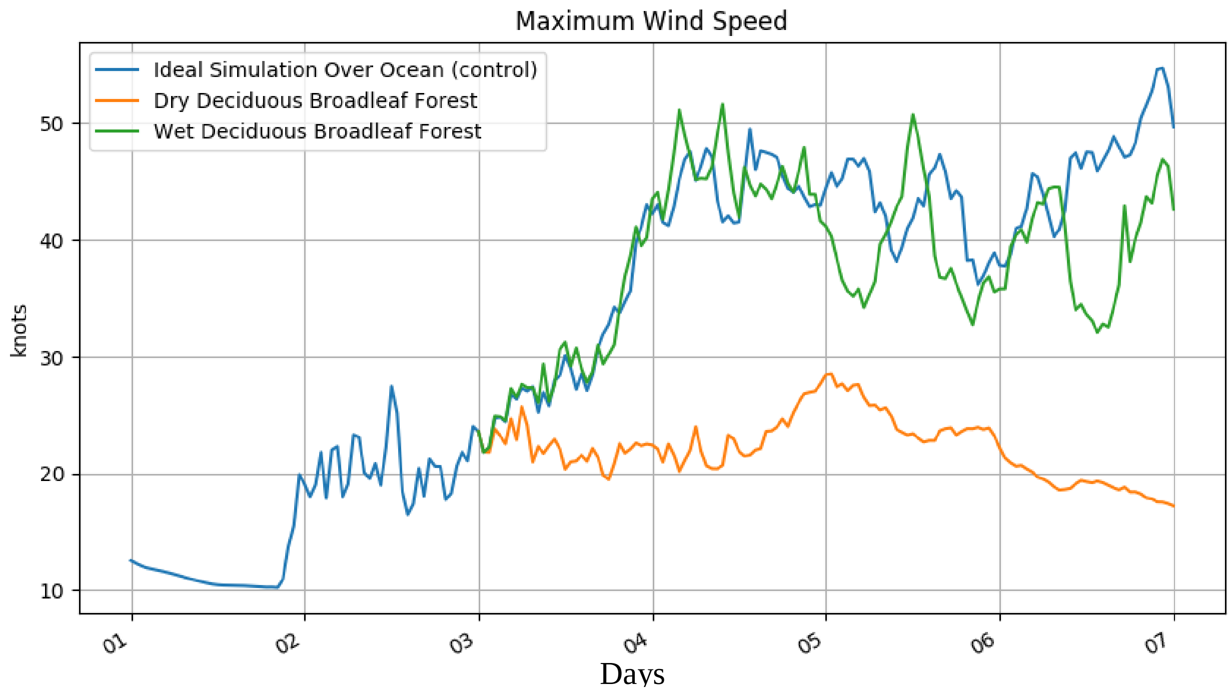

Figure 2: Maximum wind speed for the “Proof-of-Concept” simulations.

This “Proof-of-Concept” experiment, while just a preliminary exercise, was a testbed for further tests. For Chapters 2 and 3, simulations using Bare Ground and Mixed Cropland were used along with various configurations of soil moisture availability. Chapter 2 focuses primarily on the surface impacts on the improved simulations. Chapter 3 applies theories of TC intensification to the idealized simulations to produce insight into the mechanism as well as to garner information on TC intensification. Chapter 4 details a climatology of TCMI events, and produces a prototypical tool to diagnose the potential for a given TC to undergo TCMI rather than decay.

CHAPTER 2

THE INFLUENCE OF SOIL MOISTURE AND SURFACE ROUGHNESS ON AN IDEALIZED TROPICAL CYCLONE[1]

[1]Thomas A.M., J.M. Shepherd, and J.A. Santanello 2021. Submitted to *Journal of Geophysical Research: Atmospheres*

A. Introduction

It is commonly accepted that a tropical cyclone (TC) dissipates after landfall (Kaplan and DeMaria 1995; Zhu 2008) unless it undergoes extratropical transition (Evans et al. 2017; Keller et al. 2018). The reasons for the dissipation include the absence of moisture source (Shen et al. 2002; Tuleya and Kurihara 1978) and the existence of shear (Kaplan and Demaria 2001). The influence of soil moisture may slow the dissipation to a negligible rate and even reverse the dissipation rate while maintaining characteristics of a TC (Andersen et al. 2013; Andersen and Shepherd 2014; Arndt et al. 2009; Nair et al. 2019). This is termed the Brown Ocean Effect (BOE) as the ground surface is presumed to be so moist and warm that the moisture flux is comparable to that from over an ocean (Andersen et al. 2013). The impact of the BOE is not a binary categorization but rather a signal with a spectrum of influence (Yoo et al. 2020). The BOE differs from other studies that hypothesize the existence of cyclogenesis over land (Cronin and Chavas 2019; Mrowiec et al. 2011) in that the TC has been formed a priori and is influenced by surface fluxes post-landfall.

The BOE hypotheses have primarily assumed a constant soil moisture distribution. However, the assumption of uniform soil moisture is not appropriate for a realistic environment but is still consistent within the literature that supports the BOE (Andersen and Shepherd 2014). Previous studies that examined the influence of soil moisture gradients on TCs include Tropical Storm Erin (2007; Arndt et al. 2009; Kellner et al. 2012; Monteverdi and Edwards 2010) and Hurricane Danny (1997) and Hurricane Fran (1996) (Kehoe et al. 2010). Kellner et al. (2012) hypothesized that the soil moisture gradient helped produce a gradient in vorticity, which helped to reintensify Tropical Storm Erin (Arndt et al. 2009; Monteverdi and Edwards 2010). This finding is consistent with Evans et al. (2011). Kehoe et al. (2010) proposed that the enhancement of Hurricane Fran was due to soil moisture gradients. They drew from an analogy of other mesoscale circulations induced by differences in land use (Hong et al. 1995; Ookouchi et al. 1984). Kehoe et al. (2010) also indicated that Hurricane Danny had local maxima in precipitation in areas where the soil moisture gradient was prominent.

Previous studies also suggest that the intensity of TCs is dependent on the surface drag coefficient (Bryan 2013; Emanuel 1995; Malkus and Riehl 1960). The surface drag coefficient is dependent on surface roughness length and the Monin-Obukhov length (Powell et al. 2003; Stull 2009). The surface roughness is a fundamental difference between the land surface and oceanic surface which is another aspect in which the BOE is different from the typical intensification of TCs. Changes in the roughness length may reduce TC intensity overall but may also induce convergence and enhanced local winds (Zhu 2008). Increases in surface drag have also been proposed as a mechanism for the enhancement of precipitation in TCs (Zhang et al. 2018).

The goal of this research is to demonstrate the validity of the BOE from a theoretical perspective as well as test the aforementioned deviations from a typical water surface. A simulation of an idealized TC was used to conduct a series of experiments replacing the water surface with surface roughness and patterns of soil moisture availability (SMA; Lee and Pielke 1992) beneath a developed cyclone.

B. Data and Methods

The Weather Research and Forecasting Model (WRF) was used to simulate an idealized TC. Specific changes to the default configuration of the idealized TC simulation within WRF include the deactivation of radiation, convective, and land-surface parameterization, as well as a domain of 984 km x 984 km with 4 km resolution. Other settings within the idealized TC simulation include Purdue microphysics (Chen and Sun 2002), the YSU boundary layer scheme

(Hong et al. 2006) and revised MM5 surface layer scheme (Jiménez et al. 2012) with altered drag coefficient (Donelan et al. 2004). A control simulation (CTRL) with a water surface was run for a 10-day period. After a two-day period, the restart file of CTRL was altered by replacing the water surface with different land-use types and SMA profiles. Two different land-use categories were used, namely “Bare Ground” (BG; z_0=0.01 m) and “Mixed Cropland” (MC; z_0=0.1 m). Since the land-surface parameterization was deactivated, the SMA profile and the surface temperature of 301.15 K was non-variant with unintended feedback mechanisms suppressed. One limitation with this approach is that while the TC may move, the soil moisture profile does not change.

Eleven of the fourteen SMA profiles consisted of uniform SMA, ranging from 0 to 1. Three non-uniform SMA profiles were also used: a parabolically weighted Gaussian distribution (wG), inverse of the weighted Gaussian distribution (iwG), and piecewise (Pw). The wG profiles describe the effect of a TC moving over a previously moistened track as if the TC followed the tracks of a previous TC. The iwG profile shows the influence of a TC moving over a dry area but with a moist inflow. The Pw profile follows the same reasoning as the wG profile but with the SMA gradient emphasized. Those three non-uniform SMA profiles are described by Table 1, where x' and y' are normalized coordinates relative to the minimum central pressure, and R is the radius from the minimum central pressure. Particular simulations will be referred to as land use type followed by the SMA profile. For example, BG-wG will refer to the bare ground simulation with the weighted Gaussian distribution, and MC-U0.3 will refer to the mixed cropland simulation with a uniform SMA of 0.3.

Table 1: Details and equations describing the non-uniform soil moisture availability profiles.

Long Name	Abbreviated Name	Expression	Reason
Parabolically weighted Gaussian	wG	$\left(1-\frac{[x']^2}{2}-\frac{[y']^2}{2}\right)\exp[-\frac{[x']^2}{2}-\frac{[y']^2}{2})]$	Moist near center, dry at edge of domain
Inverse weighted Gaussian	iwG	$1-\left(1-\frac{[x']^2}{2}-\frac{[y']^2}{2}\right)\exp[-\frac{[x']^2}{2}-\frac{[y']^2}{2})]$	Dry near center, moist at edge of domain
Piecewise	Pw	$\begin{cases}0 \text{ if } R > 250 \text{ km}\\ 1 \text{ if } R < 250 \text{ km}\end{cases}$	Moist near center. Strongest SMA gradient.

Some caveats should be mentioned. This was a modeling study in an idealized environment so the conditions may not perfectly align in observational studies. This includes the expanse of one singular land use type, the validity of parameterizations used by the simulation, and the presence of environmental shear. Some of the assumptions may also reduce feedback mechanisms that could be an artifact of a stagnant TC rather than a TC moving over an infinite expanse. While deactivating these settings also eliminates potentially relevant feedback mechanisms and signals (Subramanian 2016; Tang et al. 2019; Tang and Zhang 2016), the reduction to the bare soil processes and roughness length effect eliminates complicating impacts.

Such complicating factors that arise from a fully coupled land surface model (LSM) include the transpiration rate, infiltration, and surface runoff, which can modulate the soil moisture. As a theoretical approach, these factors are suppressed in favor of controlling the amount of moisture that can enter the TC. Appendix A provides a justification for deactivating the LSM by simulating BG-U0.2 conditions using the NOAH LSM but with surface radiational cooling deactivated by setting the emissivity to 0. This experiment also does not test changes to surface temperature or gradients in surface temperature. Also, the method of replacing the land surface does not induce asymmetries typical of a landfalling TC. Despite these shortcomings, these simulations demonstrate the importance of having accurate representation of soil moisture profile and surface features.

C. Results

Figure 3 shows the maximum instantaneous wind speed for the BG and MC land use types for all 14 SMA profiles. CTRL achieves an asymptotically stable (Kieu 2015) quasi-steady state (QSS) shortly after rapid intensification. Although CTRL achieves a QSS, the BOE experiments decay at varying rates consistent with Kaplan and DeMaria (1995). As expected, the maximum wind speed for all of the BG simulations were generally greater than the MC simulations. One important difference between the CTRL simulation and the BG/MC simulations is the onset of rapid intensification (RI), which is defined as the increase of the maximum wind speed by 30 knots in 24 hours or less. RI onset occurs earlier in the BG/MC simulations, with the exception of the iwG and drier uniform SMA distributions of the BG simulations. The onset of RI happens earlier in the MC simulations than the CTRL. Moreover, the BG-wG and BG-Pw have a more pronounced period of RI. The maximum wind speed of the uniform BG simulations during the QSS are more incremental than the MC simulations, which shows a less distinguishable pattern. To this extent, the maximum wind speed in the QSS for the MC-Pw and MC-iwG simulations are almost indistinguishable. The maximum wind speed in the BG simulations during the QSS are more sensitive to changes in the SMA, especially near the center of the TC, than the MC simulations.

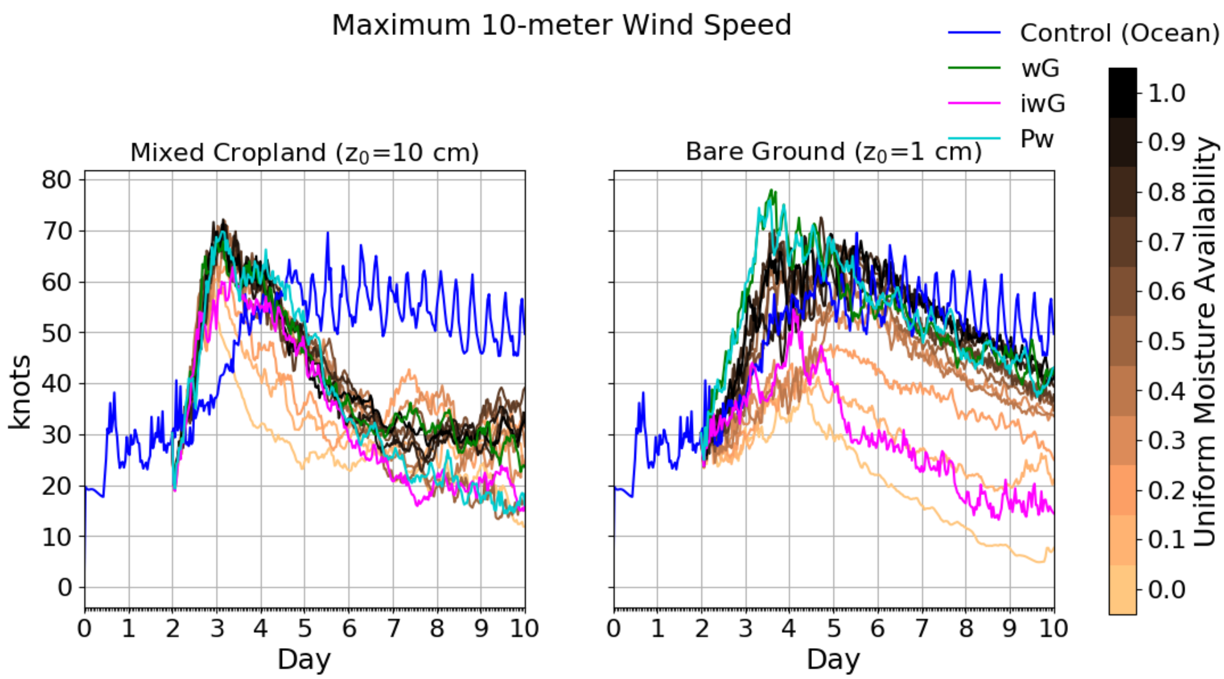

Figure 3: Maximum instantaneous wind speed (knots) for idealized tropical cyclones over a water surface (CTRL), over Mixed Cropland (left) and Bare Ground (right). The uniform SMA profiles are labeled according to the colorbar, while the CTRL and non-uniform SMA profiles are labeled in the legend.

Figure 4 shows the domain-summed total accumulated precipitation over MC (left) and BG (right). All of the MC simulations produced more precipitation than the CTRL simulation. The CTRL simulation, however, produced more precipitation simulations with a lower SMA than the BG-U0.3. The presence of a gradient in SMA had a large impact in the total accumulated precipitation. The influence of the land use type was stronger on the uniform SMA profiles than the SMA profiles that had a SMA gradient. That is, the BG-iwG produced more precipitation than the BG-U1.0, while the MC-U1.0 produced more precipitation than the MC-wG. Land use has a small impact on the total accumulated precipitation generated by SMA gradients. BG-wG and MC-wG, as well as MC-Pw and BG-Pw, have comparable total accumulated rainfall amounts, however MC-iwG produced more precipitation than BG-iwG, indicating that there may be a radial dependence to this relationship. The cause of this is likely due to the differences in sensitivity of the surface latent heat flux.

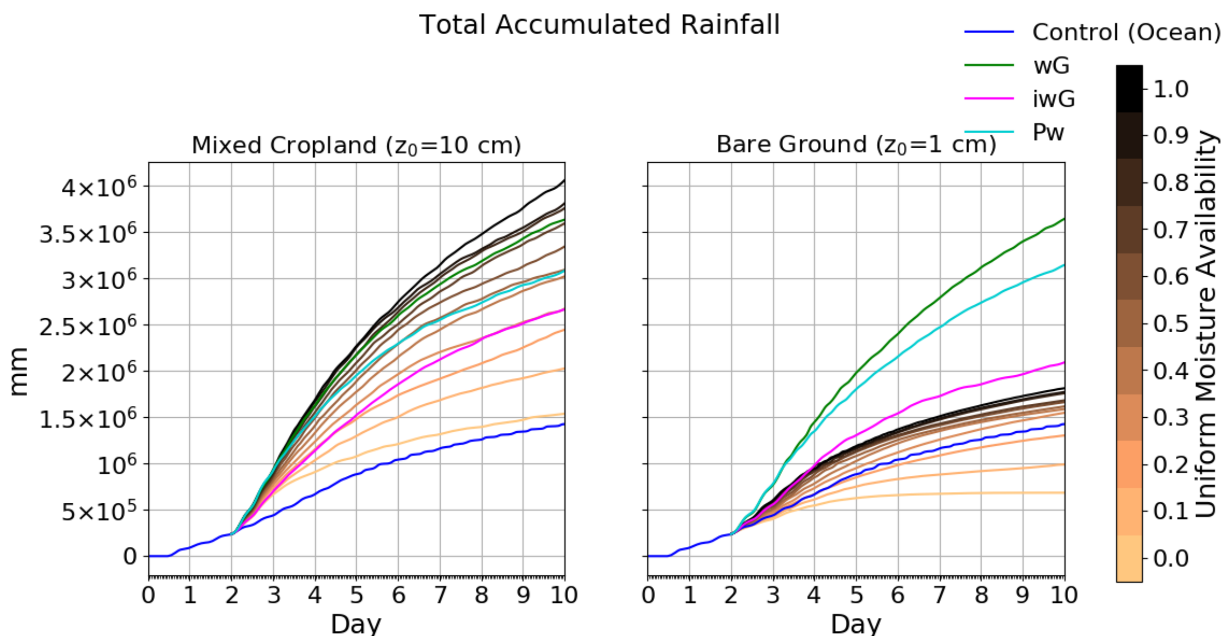

Figure 4: Domain-summed accumulated precipitation (mm) for idealized tropical cyclones over a water surface (CTRL), over Mixed Cropland (left) and Bare Ground (right). The uniform SMA profiles are labeled according to the colorbar, while the CTRL and non-uniform SMA profiles are labeled in the legend.

Figure 5 shows the surface latent heat flux, which is computed by the surface layer parameterization after 180 hours of the CTRL simulation. This demonstrates that the latent heat flux of the MC-U0.2 and BG-U0.5 most resemble the latent heat flux of the CTRL simulation. Latent heat flux increase is larger in the MC simulations than the BG simulations, even though the wind speed is lower. The cause of the difference in latent heat flux between land-use categories is due to enhancements in the bulk enthalpy transfer coefficient depicted by Figure 6. The greatest amount of latent heat flux is found in the simulations with the Pw profile. The Pw SMA profiles also have the largest gradient in latent heat flux, as expected with the gradient in the SMA profile. The enhanced soil moisture gradient allows dry air from outside the radius to be advected within the storm, enhancing the moisture gradient between the surface and lower atmosphere. This likely further increases the latent heat flux.

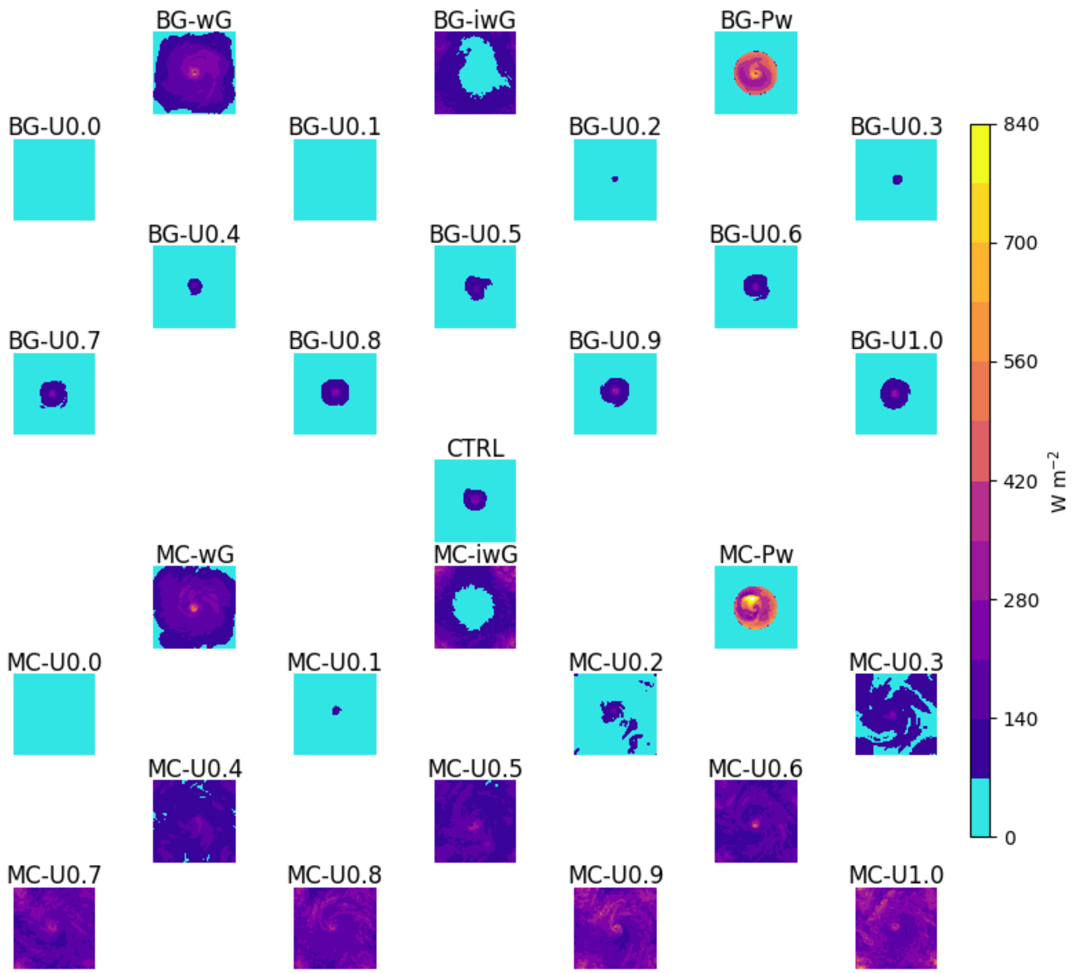

Figure 5: Surface latent heat flux (W m^{-2}) for each simulation at hour 180.

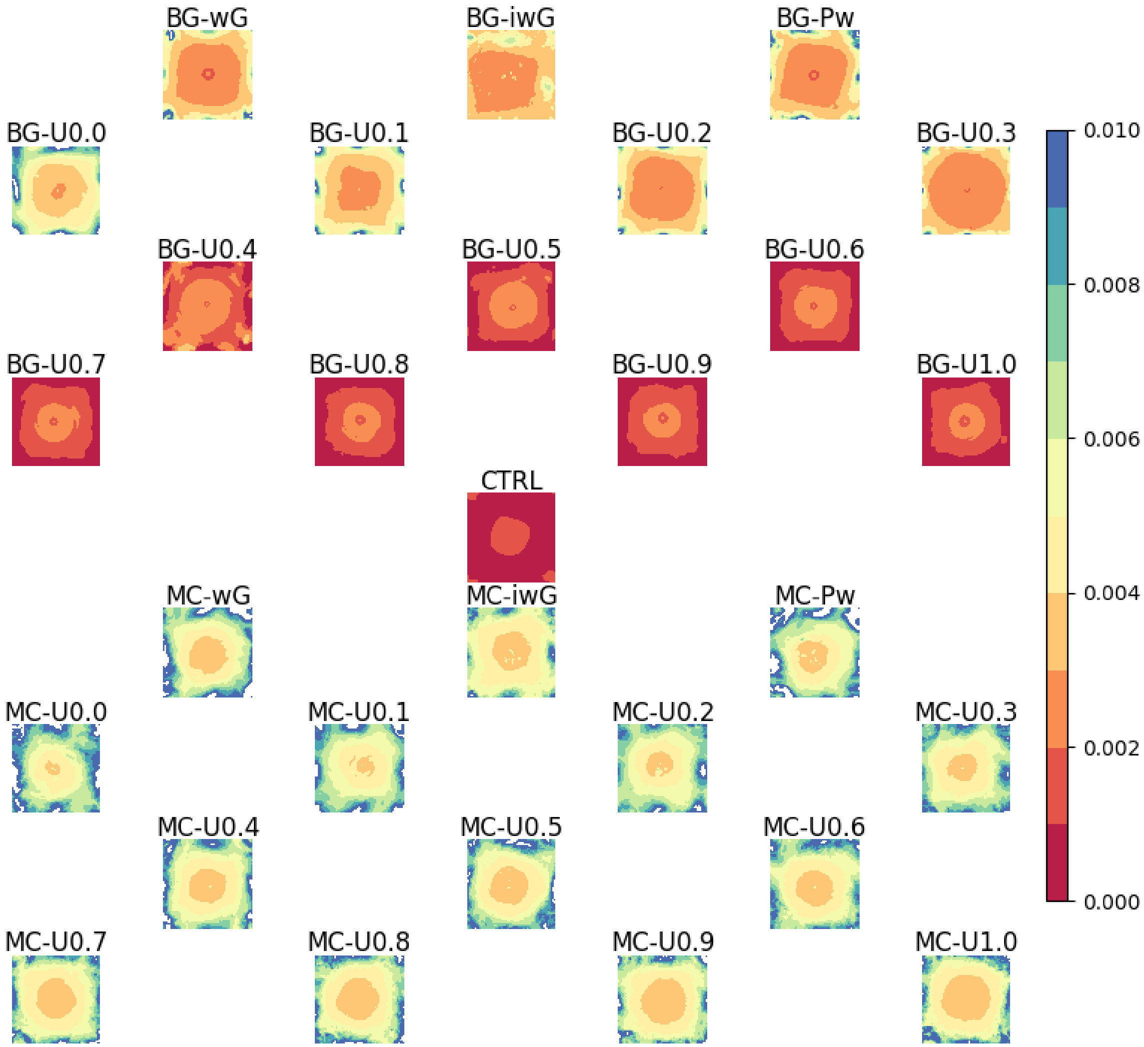

Figure 6: Enthalpy exchange coefficient after 180 hours of the CTRL simulation.

D. Discussion and Conclusions

Through the use of idealized simulations of TCs, the BOE has been demonstrated to be a mechanism of overland reintensification. Previous descriptions of the BOE ignore the existence of soil moisture gradients, which can produce more precipitation than just a uniform SMA distribution in areas with a lower roughness length. Moreover, increases in friction enhance the precipitation produced, at the cost of hurricane intensity. Thus, it is proposed that the BOE should be evaluated among two different modes, precipitation enhancement and intensification/maintenance. The pattern of sudden enhancement of convection is likely caused by the gradient imbalance associated with the imposition of the land surface (Bryan 2013). Enhancements in precipitation are more likely in areas that have more friction and weaker wind speeds. The effect of friction on precipitation suggests that hurricane-related flooding is enhanced in urbanized areas, which is consistent with the study by Zhang et al. (2018) on Hurricane Harvey.

Moreover, the influence of soil moisture gradients was investigated. It is found that the maximum wind speed is most influenced by the soil moisture closest to the center. However, when precipitation is considered, soil moisture gradients were more influential than soil moisture alone over areas with less surface roughness. This indicates that the TCs that generate the most hazardous rain-related conditions and wind damage move over a moist area with soil moisture gradients. While the radial orientation of the soil moisture gradient does have a large impact on the wind speed, it has a smaller impact on the precipitation relative to the existence of a soil moisture gradient. It is difficult to distinguish the role of the magnitude of the soil moisture due to constraints related to soil moisture and the location of the TC. The role of azimuthal differences in soil moisture may also be impactful, but was not explored.

CHAPTER 3

APPLICATION OF CURRENT HURRICANE INTENSITY THEORIES TO THE BROWN OCEAN EFFECT[1]

[1]Thomas A.M., J.M. Shepherd, and J.A. Santanello 2021. To be submitted to *Journal of the Atmospheric Sciences*

A. Introduction

The economic impact of landfalling tropical cyclones (TCs) is approximately $17 billion per year, adjusted for inflation (Weinkle et al. 2018). While it is common for TCs to dissipate after landfall (Kaplan and DeMaria 1995), it has also been accepted that the dissipation rate can be slowed by large quantities of soil moisture (Tuleya and Kurihara 1978; Shen et al. 2002). In a recent generation of studies, the post-landfalling TC dissipation rate has been showed to maintained or reversed by soil moisture and soil moisture gradients. This phenomenon has been named the "Brown Ocean Effect" (BOE; Andersen et al. 2013; Collins and Walsh 2017), in that moist soil provides enthalpy fluxes similar to those over an ocean. One characteristic of these TCs is enhanced latent heat flux (Andersen et al. 2013) in an environment favorable for TCs. Examples of the BOE post-landfall hurricane strengthening include TS Erin (2007; Evans et al. 2011; Kellner et al. 2012; Monteverdi and Edwards 2010; Arndt et al. 2009), an unnamed tropical system (Nair et al. 2019), TS Bill (Collins and Walsh 2017), and various TCs in the Bay of Bengal (Rao et al. 2019). The BOE is different from the unobserved (Emanuel 1994; Montgomery and Smith 2014) but theoretically possible (Mrowiec et al. 2011; Cronin and Chavas 2019; Tang et al. 2016) overland cyclogenesis since the BOE requires an a priori TC.

The abnormal environment for TCs provides a unique opportunity to examine the intensification mechanisms. The mainstream TC intensification theories (Montgomery and Smith 2014) assume an oceanic surface, which is disrupted by the observation of overland intensification. The first intensification theory is the wind-induced surface heat exchange (WISHE) (Emanuel 1986; Rotunno and Emanuel 1987; Emanuel 2012; Montgomery and Smith 2020), which supposes that the TC intensification is a function of the temperature, enthalpy/entropy, and momentum fluxes between the surface and outflow. These fluxes are calculated differently over land rather than over water (Stull 2009). WISHE and the corollary of the maximum potential intensity (MPI; Holland 1997; Emanuel 2012) are useful for statistical forecasts of hurricane intensity (Shimada et al. 2018) as well as estimating trends in intensity due to climate change (Henderson-Sellers et al. 1998; Elsner et al. 2008; Emanuel 1987). MPI is a moderately reliable metric for prognosticating the upper bound for intensity in different basins (Tonkin et al. 2000) with 20% of hurricanes reaching 80% or more of their MPI (Demaria and Kaplan 1994), though a few storms may become “superintense” and exceed the MPI (Persing and Montgomery 2003; Rousseau-Rizzi and Emanuel 2019). WISHE has also been utilized to study features of TCs, such as the formation of secondary eyewalls (Cheng and Wu 2018). Despite criticism of axisymmetric and gradient wind assumptions (Montgomery et al. 2009; Smith and Montgomery 2015; Smith et al. 2008; Montgomery and Smith 2020), WISHE has proven to be a reasonable conceptual model for describing the intensification mechanism (Tao et al. 2019; Zhang and Emanuel 2016; Rousseau-Rizzi and Emanuel 2020). It is hypothesized that the BOE will favor the WISHE mechanism due to the shared emphasis on surface entropy fluxes.

The challenging theory to WISHE emphasizes inner-core convective bursts that are called “vortical hot towers” (VHTs). VHT’s are hypothesized to be formed by deep convective updrafts within the eyewall, forming cyclonic vorticity anomalies (Hendricks et al. 2004). VHTs promote convective activity and act as a heating source (Montgomery et al. 2006). As a functional heating source, VHTs generate potential vorticity (PV) anomalies. These VHTs merge with the cyclone at large, creating a PV gradient. The consequent PV gradient produces vortex Rossby waves (VRWs; Moller and Montgomery 2000). The VRWs, which take on the appearance of spiral bands (Montgomery and Kallenbach 1997), make the vortex axisymmetric (Moller and Montgomery 2000; McWilliams et al. 2003). This wave-mean flow interaction acts to intensify the TC azimuthal velocity (Montgomery and Kallenbach 1997). The VHT theory has been useful in studying tropical cyclogenesis (Montgomery et al. 2006; Hendricks et al. 2004) and identifying the onset of rapid intensification (Zhuge et al. 2015). VHTs have been implicated in the overland reintensification of Typhoon Fanapi (2010) although the reintensification is not attributed to the same processes as those that are behind the BOE (Liou et al. 2016).

One additional aspect investigated herein is the amount of precipitation produced by the idealized simulations. Neither WISHE nor VHTs provide a mechanism regarding TC precipitation. Many studies have been done on precipitation but focus on the morphology of the fields (Wingo and Cecil 2010; Rogers et al. 2020; Li et al. 2015; Wen et al. 2019; Ankur et al. 2020) or the climatological frequency of TCs (Touma et al. 2019; Ren et al. 2006; Feldmann et al. 2019; Larson et al. 2005; Li and Zhou 2015; Zhu and Quiring 2013; Tu et al. 2020). However, the impact of TCs like Hurricane Harvey (2017) highlight the need for a mechanism explaining the precipitation over land (Zhang et al. 2018; Li et al. 2020). Therefore, an equation will be derived to quantify the sensitivity of rainfall to the surface roughness. It should be noted that this principle is not limited to TCs but can be found within rainfall in urban regions (Zhang et al. 2014).

The goal of this research is to apply the intensification theories to the BOE to yield insight into the mechanism governing overland intensification. Section 2 documents the use of idealized simulations of TCs where the ocean surface was replaced with different land surfaces. Section 3 describes the structure of the resulting cyclones with an emphasis on the particularly relevant variables in each intensification mechanism. Section 4 discusses the structural changes to the idealized TC and interprets the resultant variables in the light of both intensification theories. Section 5 elucidates the relationship between the BOE and TC intensification, and provides insight into the TC intensification.

B. Data and Methods

a. Idealized Simulations

A simulation of an idealized TC on an f-plane over water (CTRL) within the WRF model was conducted with an elapsed time of 10 days. The settings for all simulations are described by Table 2. These settings are similar to those used in Tao et al. (2019) and Hill and Lackmann (2008). One potentially significant modification is the deactivation of the land-surface model, which effectively holds the surface properties as fixed. This prevents unintended feedback mechanisms such as evaporative cooling altering the surface temperature or precipitation altering the soil moisture availability (SMA; Lee and Pielke 1992) but also eliminates the cooling of the surface by the downdraft as well as recycling of TC precipitation (Liu et al. 2019). Disabling the land-surface model also does not consider the effect of evapotranspiration, which implies that the latent heat flux may be underestimated over vegetation.

Table 2: WRF model settings for all experiments.

Setting	Choice	Reference
Horizontal resolution	4 km	N/A
Radiation	None	N/A
Cumulus physics	None	N/A
PBL	YSU	Hong et al. (2006)
Microphysics	Purdue-Lin	Chen and Sun (2002)
Initial profile	None	Jordan (1958)
Boundary conditions	Cyclic	N/A

After two days of elapsed time, the simulation was restarted with a land surface replacing the water surface. The land use types include a bare ground (BG) and mixed cropland (MC). The bare ground land use type has a roughness length of 1 cm, and the mixed cropland has a roughness length of 10 cm. By contrast, the roughness length formulation over water, which is in the CTRL simulation, is dependent on wind speed (Donelan et al. 2004). In addition to the alteration to the roughness length, the SMA was modified. Eleven horizontally uniform SMA profiles incrementally increasing from 0 to 1 were conducted for each of the land use types. Additionally, three spatially non-uniform SMA profiles described by Table 3, were applied to each of the land use types. The wG and Pw simulations emphasize the SMA closest to the center of the storm with the latter having the strongest SMA gradient. The third non-uniform SMA profile, the iwG, has the driest soil closest to the center of the storm.

Table 3: Non-uniform soil moisture availability profiles.

Long Name	**Abbreviated Name**	**Expression**	**Reason**
Parabolically weighted Gaussian	wG	$\left(1-\frac{[x']^2}{2}-\frac{[y']^2}{2}\right)\exp[-\frac{[x']^2}{2}-\frac{[y']^2}{2})]$	Moist near center, dry at edge of domain
Inverse weighted Gaussian	iwG	$1-\left(1-\frac{[x']^2}{2}-\frac{[y']^2}{2}\right)\exp[-\frac{[x']^2}{2}-\frac{[y']^2}{2})]$	Dry near center, moist at edge of domain
Piecewise	Pw	$\begin{cases}0 \text{ if } R > 250 \text{ km} \\ 1 \text{ if } R < 250 \text{ km}\end{cases}$	Moist near center. Strongest SMA gradient.

The simulations will be referred to by the land use type followed by the abbreviated name of the SMA profile found in Table 3. Uniform SMA profiles will be referred to as U followed by the value of the SMA. For example, the bare ground simulation with a piecewise SMA profile will be referred to as BG-Pw, and the simulation using a mixed cropland with a uniform SMA profile of 0.8 will be referred to as MC-U0.8. Computations of height, potential vorticity, updraft helicity, and equivalent potential temperature were done using WRF-Python (Ladwig 2019).

b. Methodology of Evaluation

1) WISHE

Tao et al. (2019) examined the validity of several assumptions within WISHE. These include the validity of the gradient wind assumption above the PBL, and the functional relationship of the angular momentum and saturation entropy signifying moist slantwise neutrality. We will examine the slantwise convection assumption as well as modify the saturated surface assumption within the MPI equation.

One of the assumptions of WISHE is the existence of a steady-state cyclone under idealized conditions. In order to calculate the MPI, some of the underlying assumptions include a constant ratio of the enthalpy exchange coefficient to drag coefficient, a constant PBL temperature, and constant radius of maximum wind at the PBL. This will be evaluated at the radius of azimuthally-averaged tangential winds. Additionally, the formulation of the potential intensity equation described by Bister and Emanuel (1998) will be modified to account for surface moisture. The modification to the original equation, which is

$$V_{MPI} = \sqrt{\frac{C_k}{C_D}(s_* - s)(T_s - T_0)} \qquad \text{Equation 1}$$

where C_k is the surface enthalpy coefficient, C_D is the surface drag coefficient, T_s is the surface temperature, and T_0 is the ouflow temperature, will primarily affect the difference between the saturation entropy, s_*, and the surface entropy, s. The ansatz equation is

$$V_{ansatz-MPI} = \sqrt{\frac{C_k}{C_D}(s_{*a} - s_a)(T_s - T_0)} \qquad \text{Equation 2}$$

where s_{*a} and s_a are the modified saturated and unsaturated surface entropy. Entropy was computed using

$$s(T_s, q) = c_p(q)\ln[\theta_e(T_s, q)] \quad \text{Equation 3}$$

where c_p is the moist specific heat capacity, q is the water vapor mixing ratio at 2 meters, and θ_e is the equivalent potential temperature computed by WRF-Python (Ladwig 2019). The modified saturated and unsaturated surface entropy are computed as

$$s_{*a} = s(T_s, Mq_s[T_s]) \quad \text{Equation 4}$$

$$s_a = s(T_s, Mq) \quad \text{Equation 5}$$

where M is SMA, and q_s is the saturated water vapor mixing ratio at the surface. The basis of the ansatz is that a relaxation of the saturation assumption for surface entropy is more appropriate for land than over the ocean. Variables are used at 2 meters only when the variable at the surface was unavailable. Since SMA is the surface soil specific humidity, the amount of moisture is the product of SMA and saturated mixing ratio. The purpose of altering the saturation entropy in addition to the surface entropy is to prevent an inflation of the maximum velocity due to an inflated entropy difference.

2) VHT Theory

VHTs are definitive convective perturbations that contribute to diabatic heating within the eyewall. The variables of interest for the identification of VHTs are microphysical diabatic heating, potential vorticity, and vertical velocity. Therefore, VHTs may be identified through an azimuthal variance of those variables. The presence of VRWs will also be identified. The identification of VHTs is insufficient to the attribution of intensification so the mean PV response and tangential velocity will also be examined.

C. Results

a. WISHE Analysis

Since WISHE is based on the idea of slantwise-neutral moist convection, angular momentum is presumed to be a function of entropy. Figure 7 displays the angular momentum and the saturated entropy averaged between 72 and 132 hours of CTRL simulation. This period is presumed to be shortly after landfall. In both the MC and BG experiments, the warm core becomes more prominent with increasing SMA. Corresponding to the stronger warm core, the tendency towards slantwise-neutral convection increases with SMA.

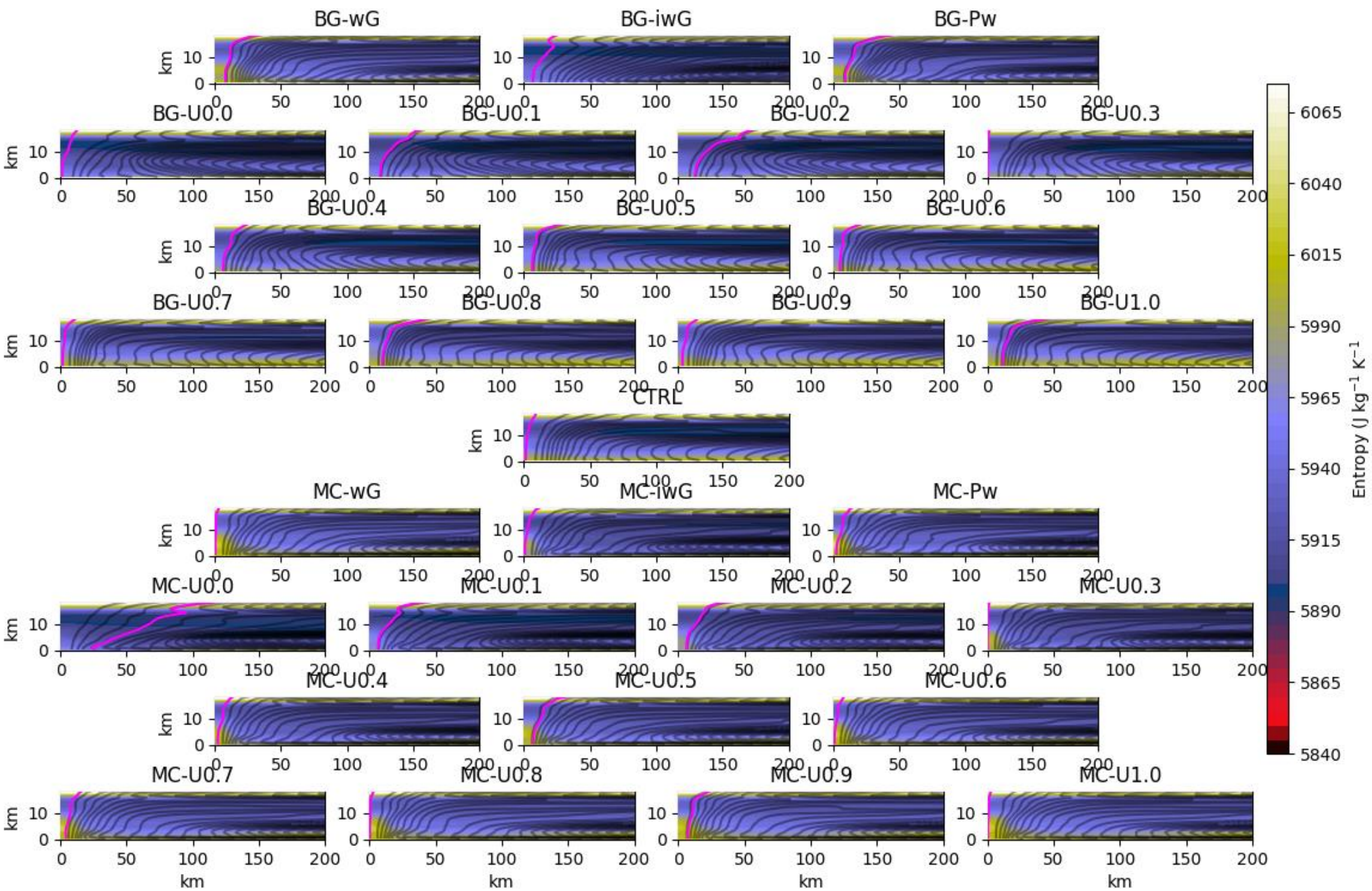

Figure 7: Saturation entropy (filled contours) and angular momentum (black contours), averaged between 72 and 132 hours of CTRL simulation. The magenta contour represents the angular momentum of the maximum azimuthally-averaged tangential wind at 10 m.

Figure 8 and Figure 9 show the maximum radial velocity in each column and that of the surrounding 4 levels, averaged between 72 and 132 hours and 144 hours to the end, respectively. The first period is semi-stable since the MC and non-uniform SMA distribution eventually have an outflow at a lower height. While this difference in height between the two periods may be a result of the TC-influenced environment affecting the TC, this new height may also be interpreted as a new steady state given that the uniform SMA in the BG simulations resemble the CTRL simulation. This lower height may be due to the enhanced latent heat fluxes increasing condensational warming aloft and reducing the height of the updraft, Evidence of this is provided in Figure 11, which is the azimuthally-averaged change in the potential temperature with height.

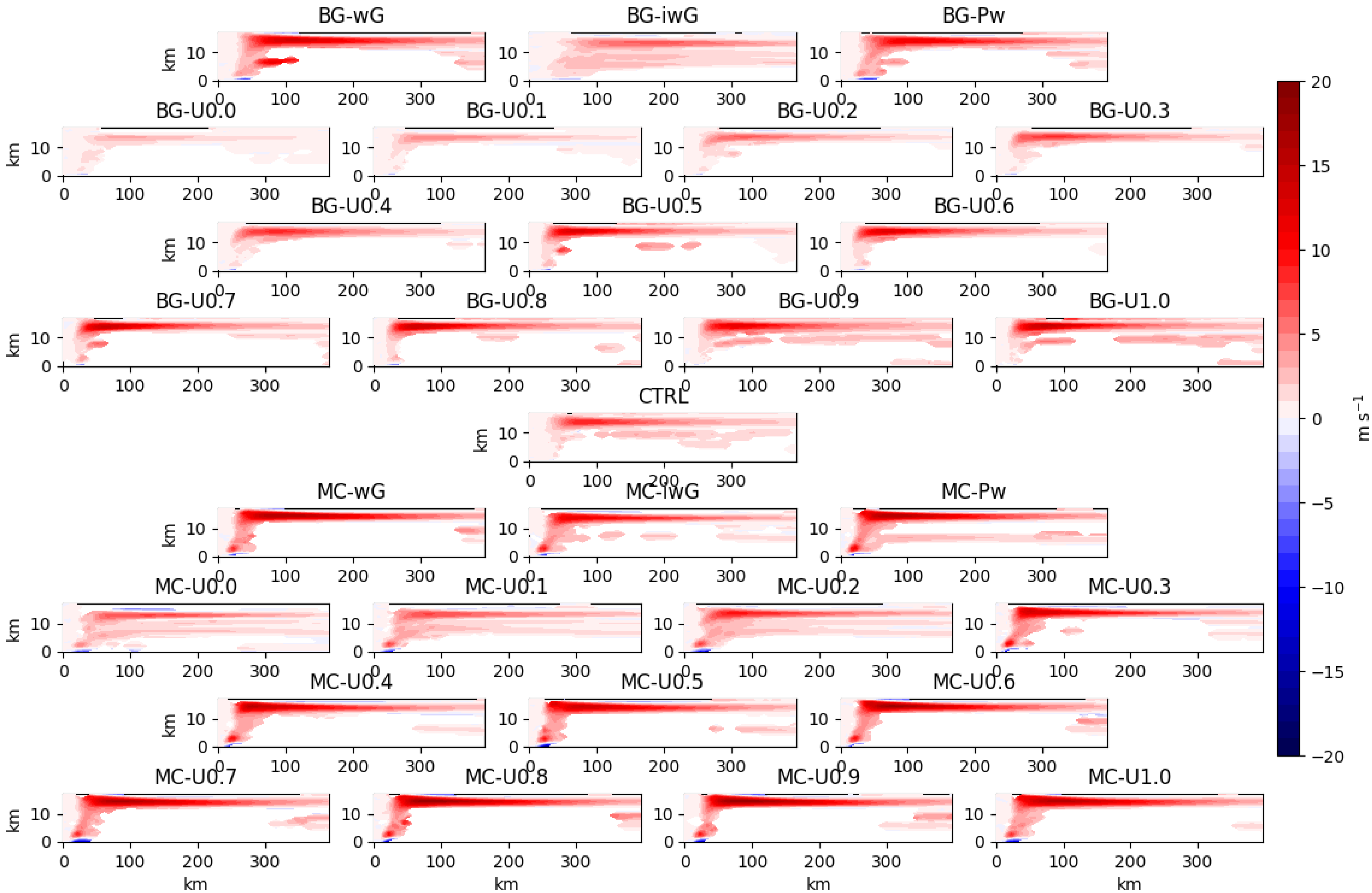

Figure 8: Radial velocity of the outflow and surrounding levels, averaged between 72 and 132 hours.

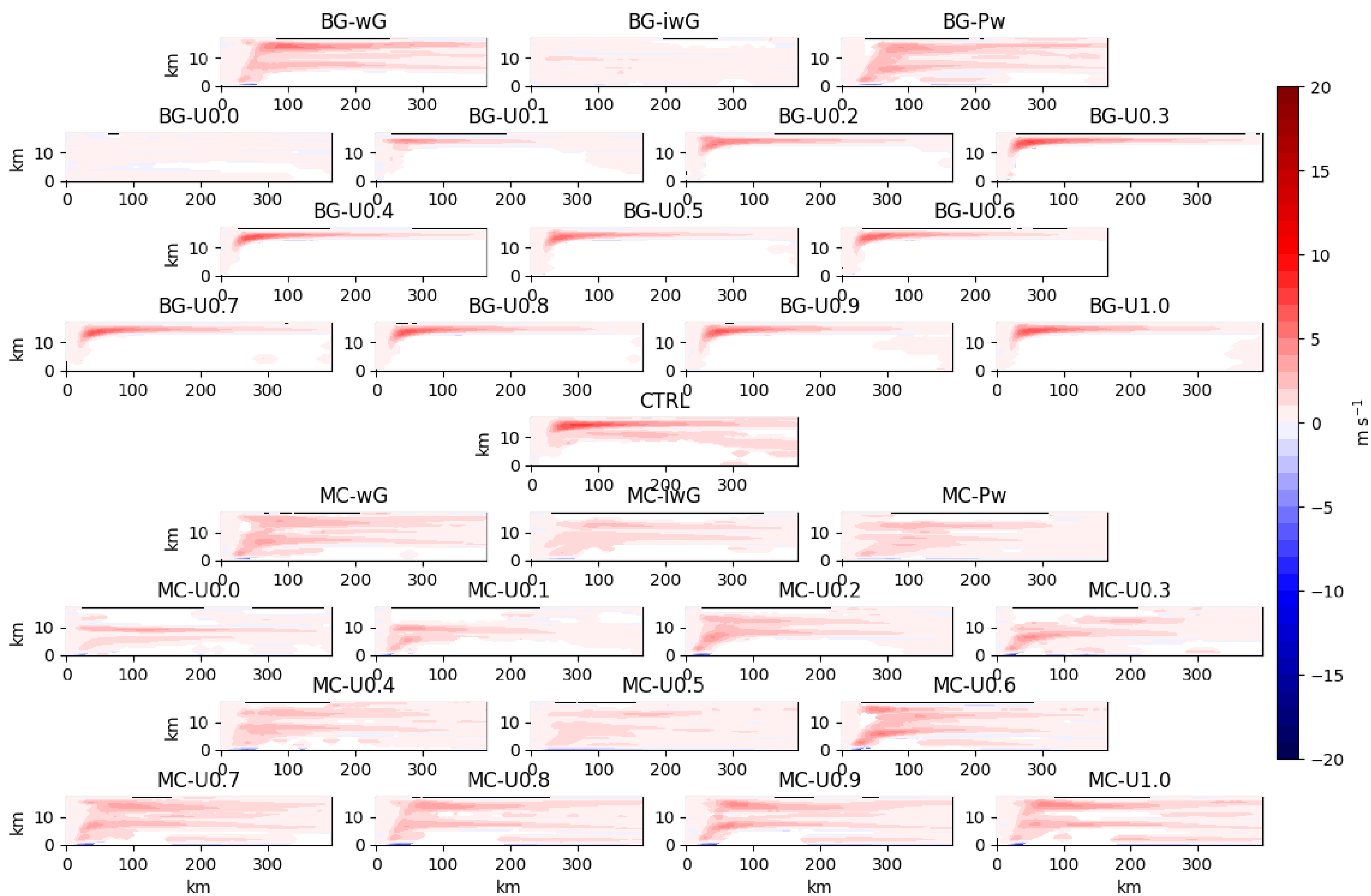

Figure 9: Same as Figure 8, but averaged between 144 hours and the end of the experiment.

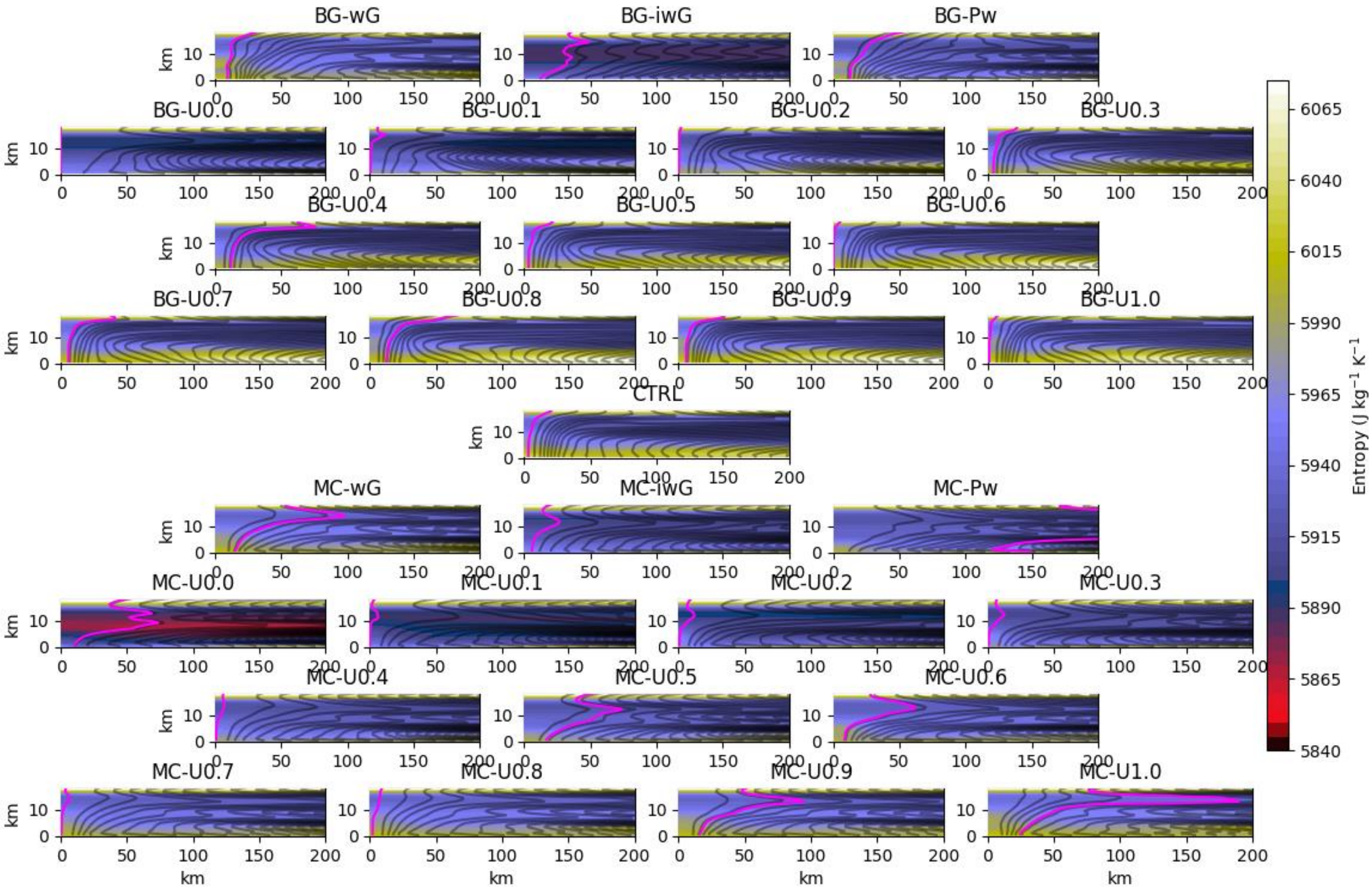

Figure 10: Same as Figure 7, but averaged between 144 hours and the end.

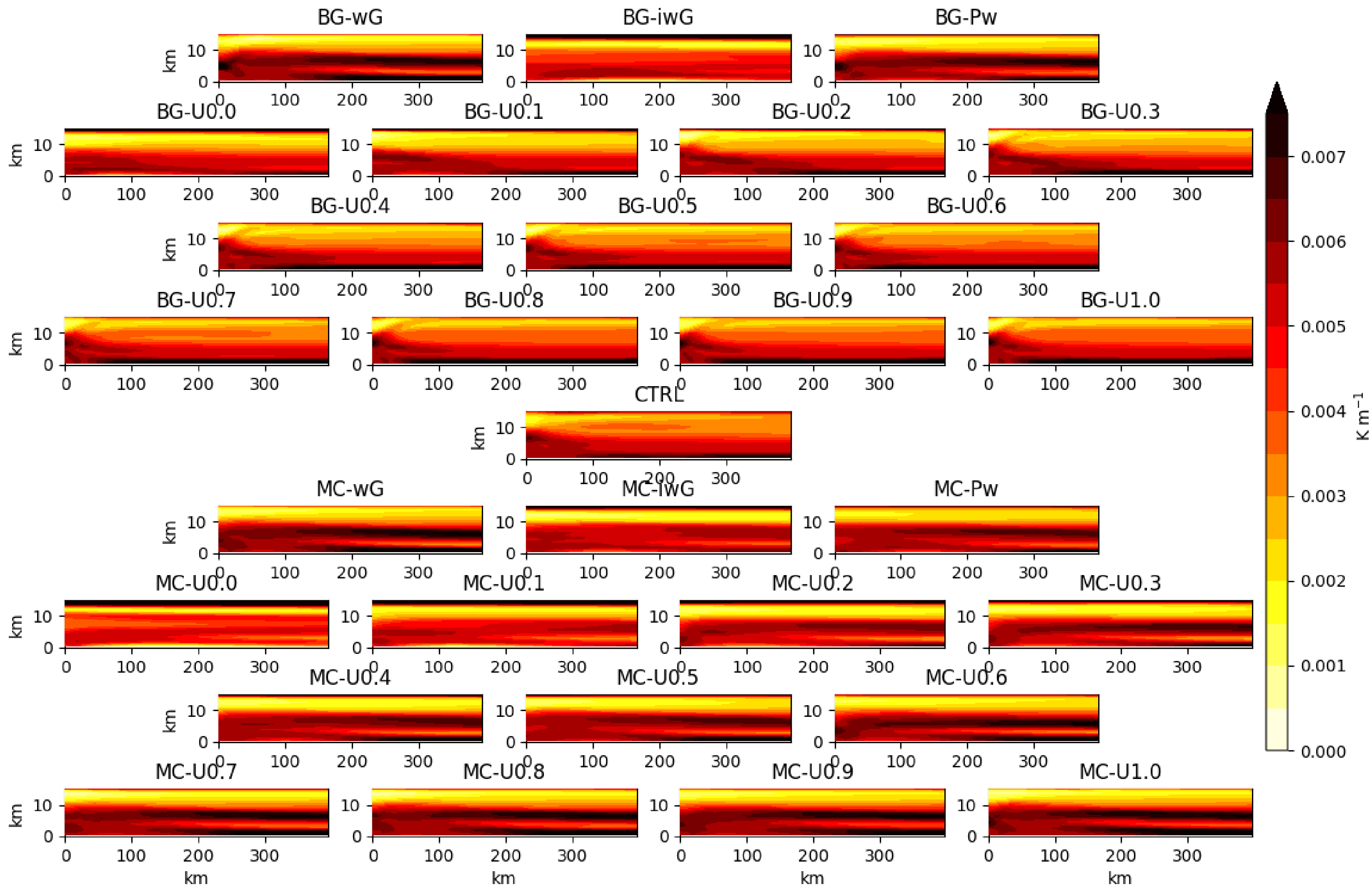

Figure 11: The change in the potential temperature with height during the late period

The change in the convection and thermal wind is reflected in Figure 12, which is part of the cyclone phase space (CPS; Hart 2003) diagram. Large circles depict the period between 72 and 132 hours and "x" depicting the period between 144 hours and the end. CPS diagrams describe the thermal structure of cyclones. Warm-core cyclones are typically TCs, and cold-core cyclones are typically extratropical cyclones. Usually within CPS diagrams, baroclinicity is examined, but that requires TC movement, which is not applicable in this study. The comparison involving baroclinicity was not done since the translation speed for the TCs was either nonexistent or negligible. Thus, the component of the CPS diagram that was examined was the thermal wind comparison between the lower levels (900-600 hPa) and the upper levels (600-300 hPa). The simulated TCs have deep warm cores during the early period with few exceptions. During this period, the MC simulations tend to be deeper than the BG simulations. While all simulations have a weaker lower level thermal wind than for the upper level, this is far more prominent in the later period when the low-level thermal wind changes sign. This suggests that the BG simulations with uniform SMA distributions have a low-level cold core similar to a post-tropical cyclone like Hurricane Sandy (2012). Figure 12 also indicates that the warm core structure is maintained in the MC simulations. Neither is supported by Figure 10, which may indicate that the CPS diagram can be misinterpreted absent thermal asymmetry information. It may also be due to the stratification from the prolonged presence of the updraft. The late structure of the MC-Pw indicates that extratropical transition (ET) has started, which is in contrast to the early MC-Pw. Contrasting this difference to the difference between the early and late periods of the BG-Pw experiment indicates that roughness length has an influence on ET. Moreover, the similarity between the late structure of MC-iwG and BG-iwG indicates that when the SMA is lower near the center, the impact of the land surface is negligible in the final state. In comparison, when the SMA is greater near the center than in the environment, a deep warm core is favored. It should be noted that ET inferred by the CPS diagram does not mean that actual ET, which involves entanglement with a baroclinic zone, fully occurred.

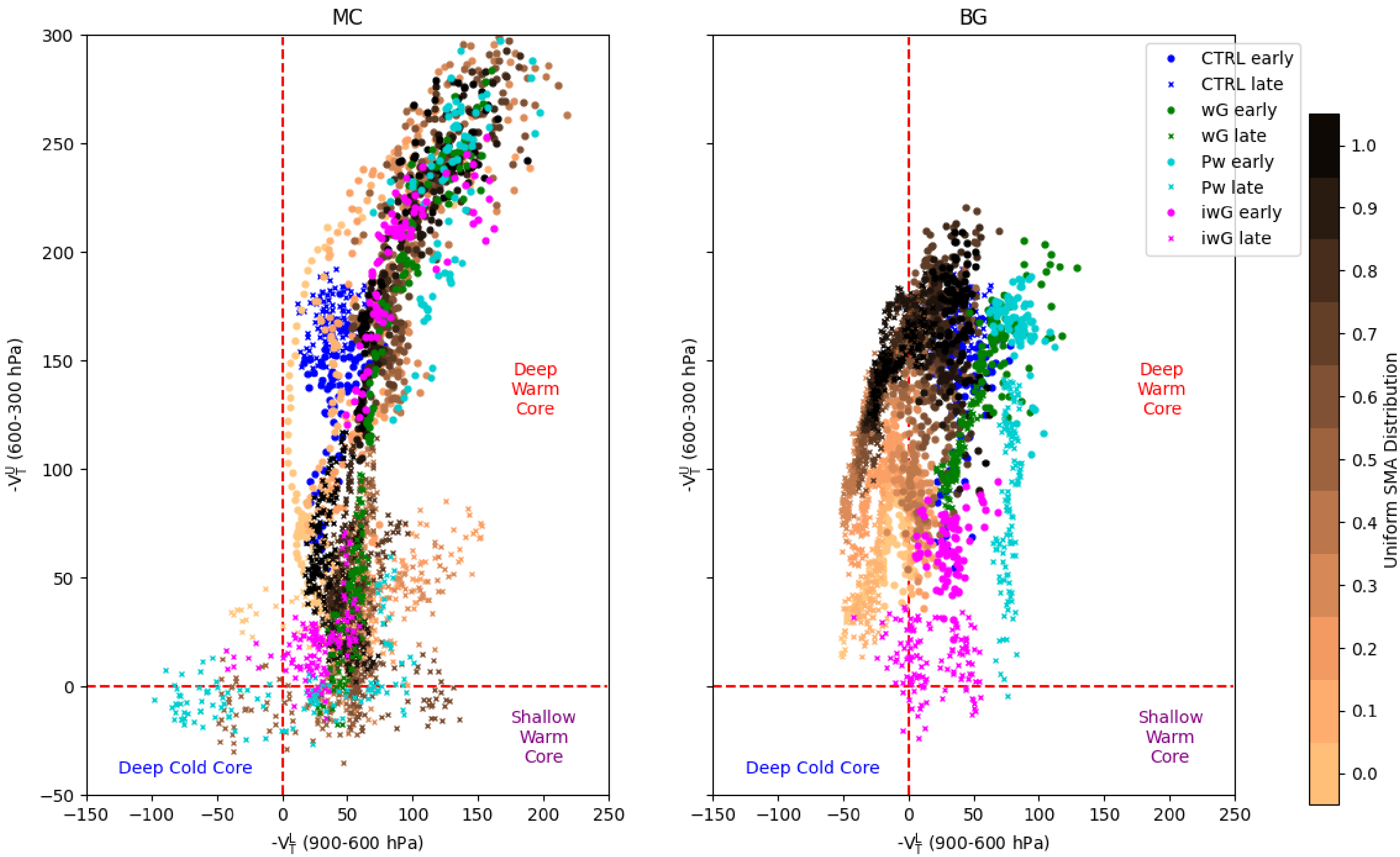

Figure 12: The thermal wind comparison plot of the Cyclone Phase Space diagram. Large circles represent the time period between 72 hours and 132 hours of CTRL simulation and "x" represents an instance between 144 hours and the end.

Figure 13 shows the maximum azimuthally averaged tangential wind speed, the MPI, and the ansatz for the BG and MC experiments. The temporal average for each of the aforementioned variables changes due to uniform SMA is quantified in Table 4. Since the SMA for the ocean is 1, the MPI and the ansatz are the same for the CTRL simulation. The change from the oceanic surface to the land surface does have an impact on the MPI, but the influence that SMA distributions have are minor with lower SMA distributions having a larger temporal variance though the MPI of the BG-Pw and BG-wG simulations are less than the other simulations. Unlike the MPI, the ansatz shows a progression that approximates the modeled wind speed. This implies that the ansatz is a better indicator of the BOE than the ordinary MPI. However, as predicted, the ansatz underestimates the wind speed for the driest soils, namely the U0.0 simulations. The ansatz also underestimates the wind speed for the iwG simulations, possibly since the evaluation of the ansatz is closer to the drier part of the domain.

		Slope (m s^{-1} per 0.1 SMA)	**p-value**
BG	MPI	-1.24	6.02e-05
	Ansatz	3.24	8.03e-05
	Maximum Azimuthally-Averaged 10-m tangential wind speed.	1.35	1.07e-04
MC	MPI	-0.93	1.03e-04
	Ansatz	1.81	1.6e-04
	Maximum Azimuthally-Averaged 10-m tangential wind speed.	0.47	4.99e-03

Table 4: Linear regression statistics for the azimuthally and temporally averaged intensity parameters

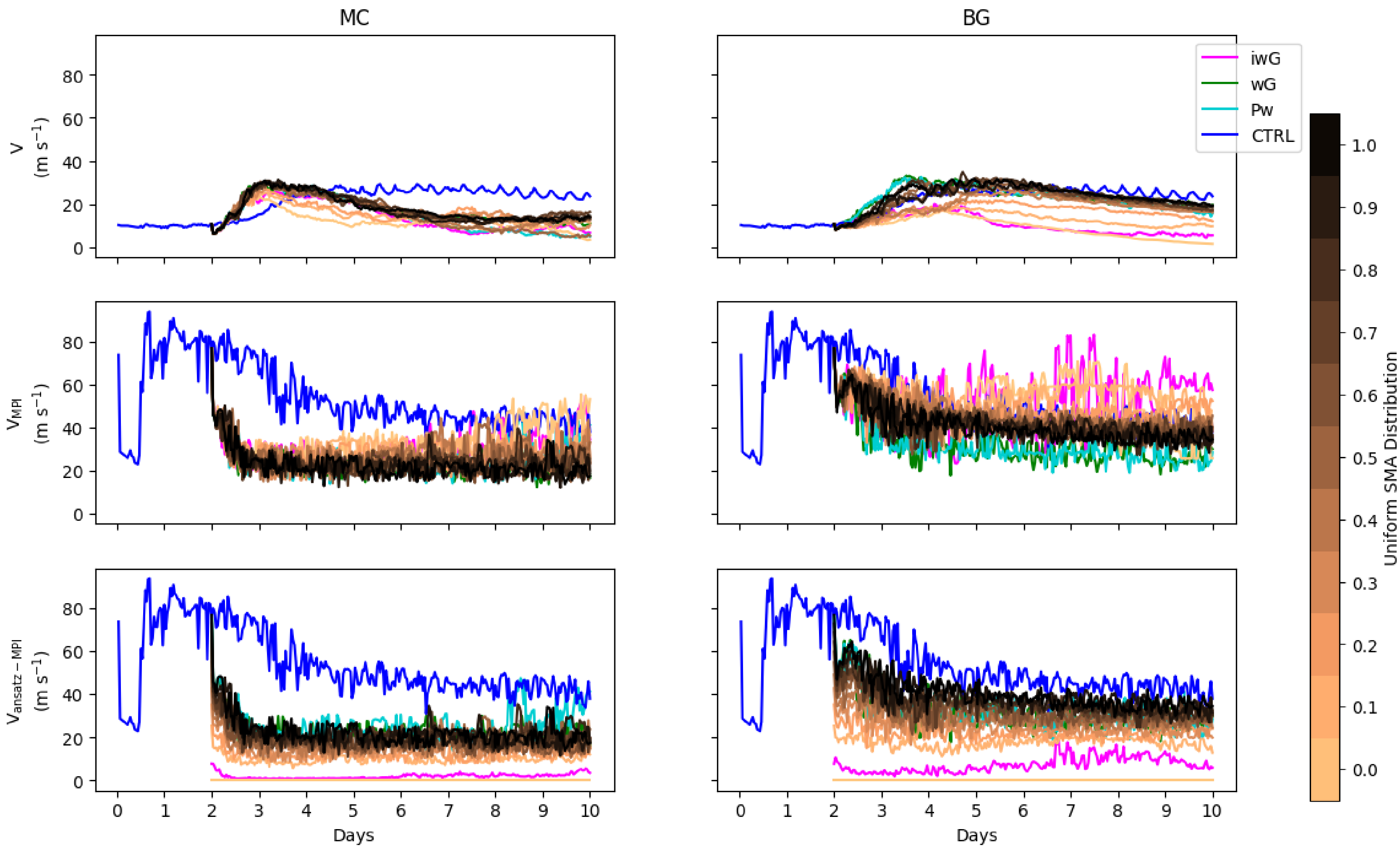

Figure 13: Timeseries for the azimuthally-average tangential 10 m wind speed (top row), MPI (middle row), and ansatz-MPI (bottom row).

The iwG and U0.0 cases are not the only instances of superintensity in the suite of experiments. Figure 14 shows the difference between the MPI and the modeled wind speed as well as the ansatz and the modeled wind speed. The impact of switching to a new land surface is most apparent in the MC simulations. All can be regarded as superintense at some point in which modeled intensity exceeds the MPI before the transition to the quasi-stable steady state. This is analogous to a TC moving over an area of cooler water that cannot support the current intensity. Superintensity is more prevalent in the MC simulations than the BG simulations. The BG-wG and BG-iwG simulations are superintense more often than the other BG experiments possibly because the entropy difference is larger. This is not the case with the ansatz where the modeled wind speed of the iwG simulations exceed the ansatz. This condition will be called ansatz-superintensity. The degree of ansatz-superintensity decreases with increasing SMA indicating that this metric is more appropriate for instances where BOE mechanisms are possible. This applies more to the BG simulations; however, the MC simulations also show that the ansatz is a more reasonable estimation of modeled wind speed than MPI. It should be noted that this does not defeat the purpose of MPI, which was to be a maximum theoretical wind speed. The ansatz is a useful metric for quantifying the BOE.

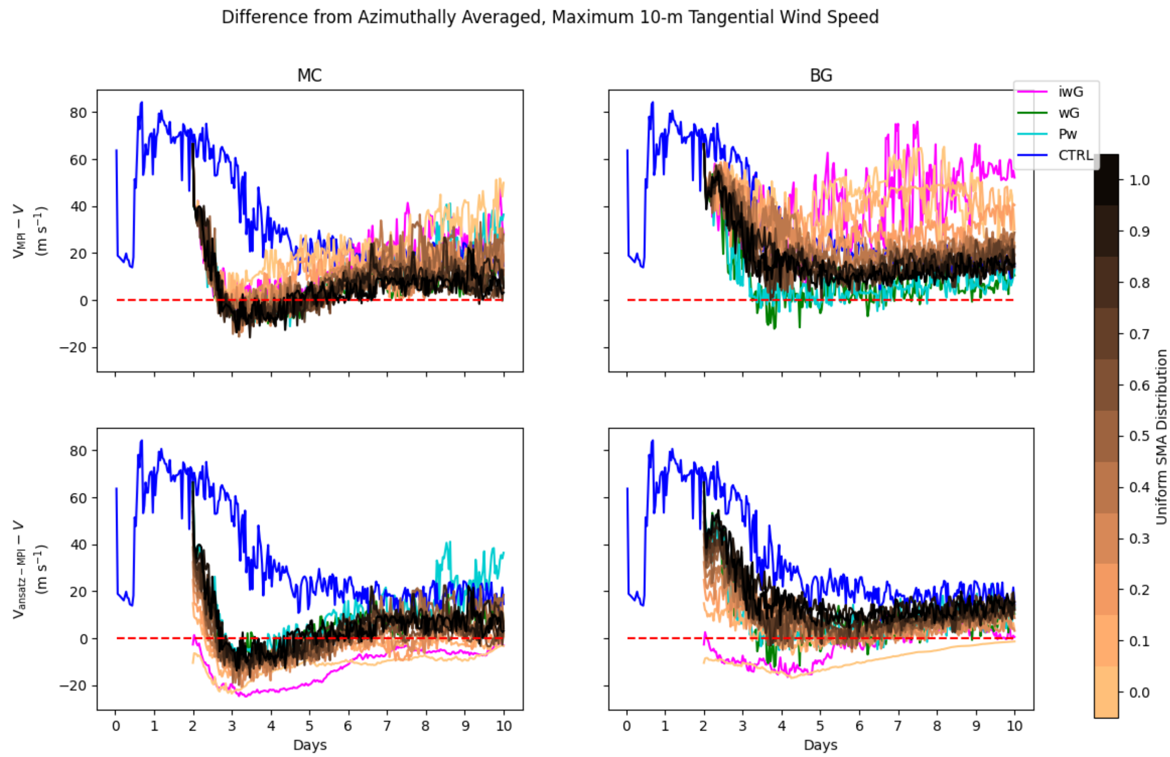

Figure 14: Difference from the azimuthally-averaged, maximum 10 m tangential wind speed for the MPI (top row) and ansatz-MPI (bottom row).

Figure 15 shows the various components of the MPI and ansatz-MPI. While the ratio of surface transfer coefficients has a sudden expected decrease, the other variables have noticeable differences. The unmodified entropy difference decreases with SMA, whereas the modified entropy difference increases with SMA. While the temperature difference between the outflow and the surface shows a small sensitivity to SMA, the land use has a larger impact. While this may be attributable to the lower outflow, a more likely reason is that the updraft was more tilted, leading to a maximum radial velocity that is at a lower height. This is evidenced by the warmer outflow occurring prior to the early period.

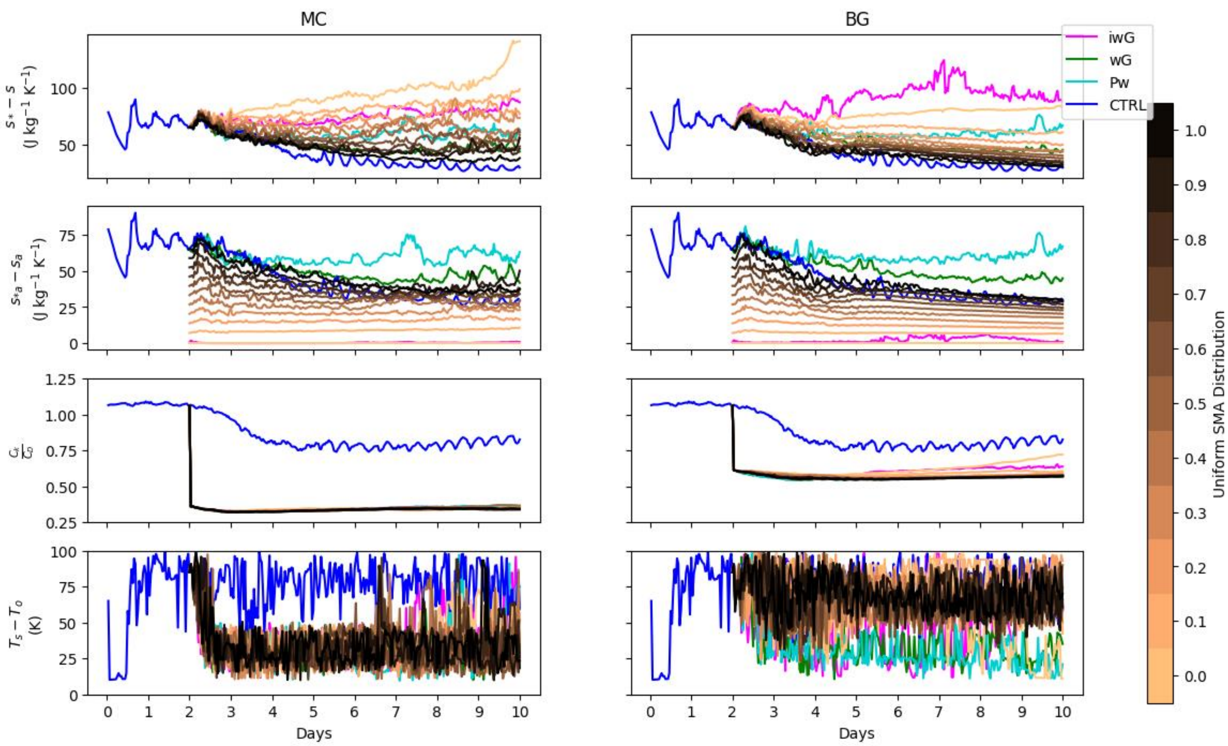

Figure 15: The surface entropy difference (top row), the modified entropy difference (second row), the ratio of surface exchange coefficients (third row) and surface-outflow temperature difference (bottom row), which are components of the MPI and ansatz-MPI.

b. VHT Analysis

Figure 16 displays a time-radius plot of azimuthally averaged simulated radar reflectivity. The presence of VRWs are more prominent in the CTRL simulation than the other simulations. The serialized maxima of reflectivity are indicative of VHTs with the rainband/VRW emanating radially from it. The pattern of VRWs is longer-lived in the CTRL simulation than the uniform BG simulations where the size of the rain shield narrows. This is not the case in the MC simulations or non-uniform SMA distributions where the rain shield does not decrease in size. Although there may not be reflectivity maxima, this is not indicative of the absence of VHTs.

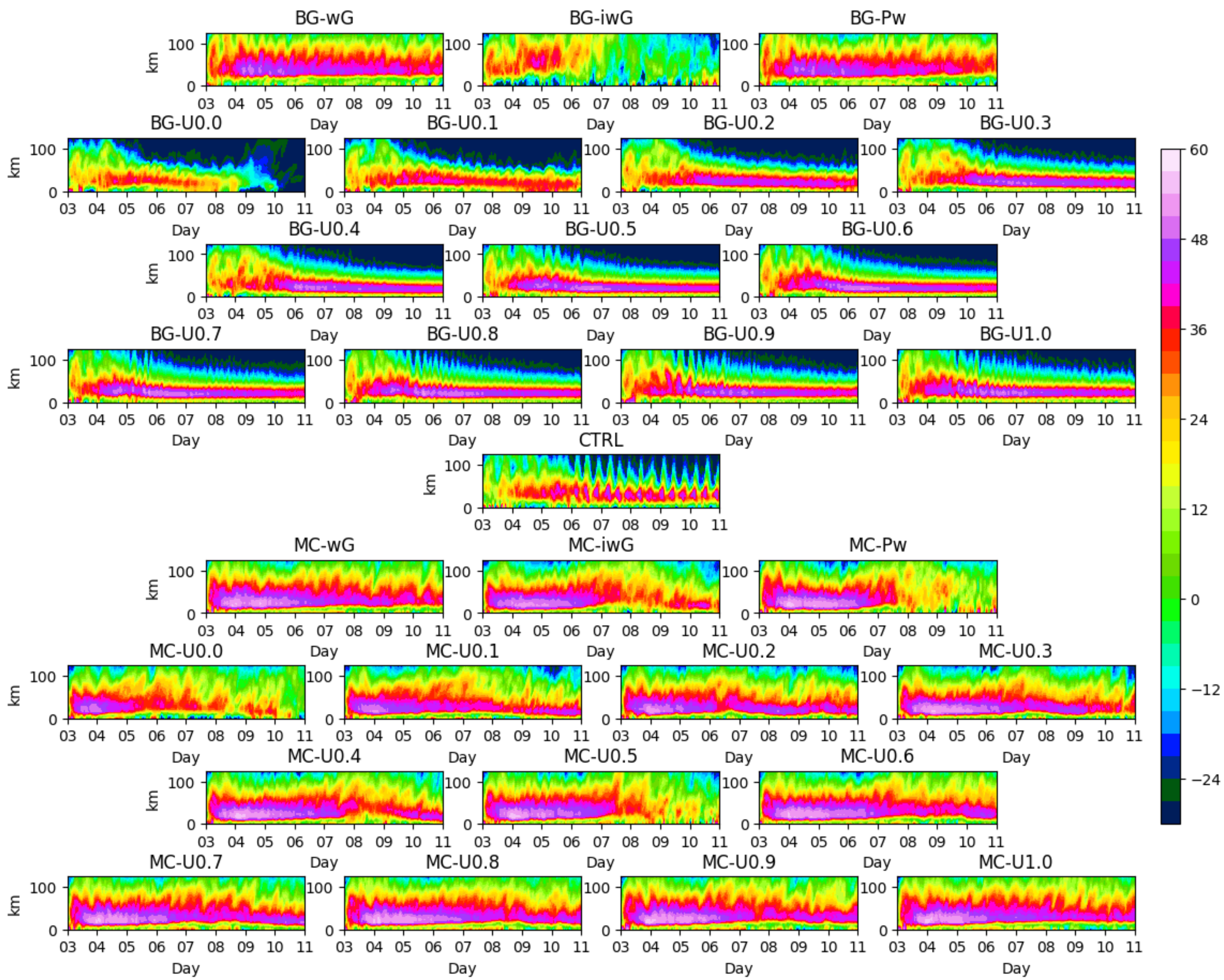

Figure 16: Time-radius plot of azimuthally averaged simulated radar reflectivity.

Figure 17 shows a time-radius plot of azimuthal variance of the updraft helicity (filled contours) and azimuthally averaged 10-m wind speed (white contours). The MC simulations have the most prominent VHTs early, but they dissipate at later times. This is consistent with the role that VHTs have in rapid intensification. The BG simulations with uniform SMA distributions as well as the CTRL simulation have VHTs that are more periodic and resilient during the later times though the VHTs quickly decay in the BG simulation. The absence of VHTs from the BG simulations with non-uniform SMA distributions as well as the MC simulations provides evidence that convection was suppressed in those simulations. The appearance of wind speed and VHTs shows that the relationship is consistent in the BG simulations but delayed in the MC simulations.

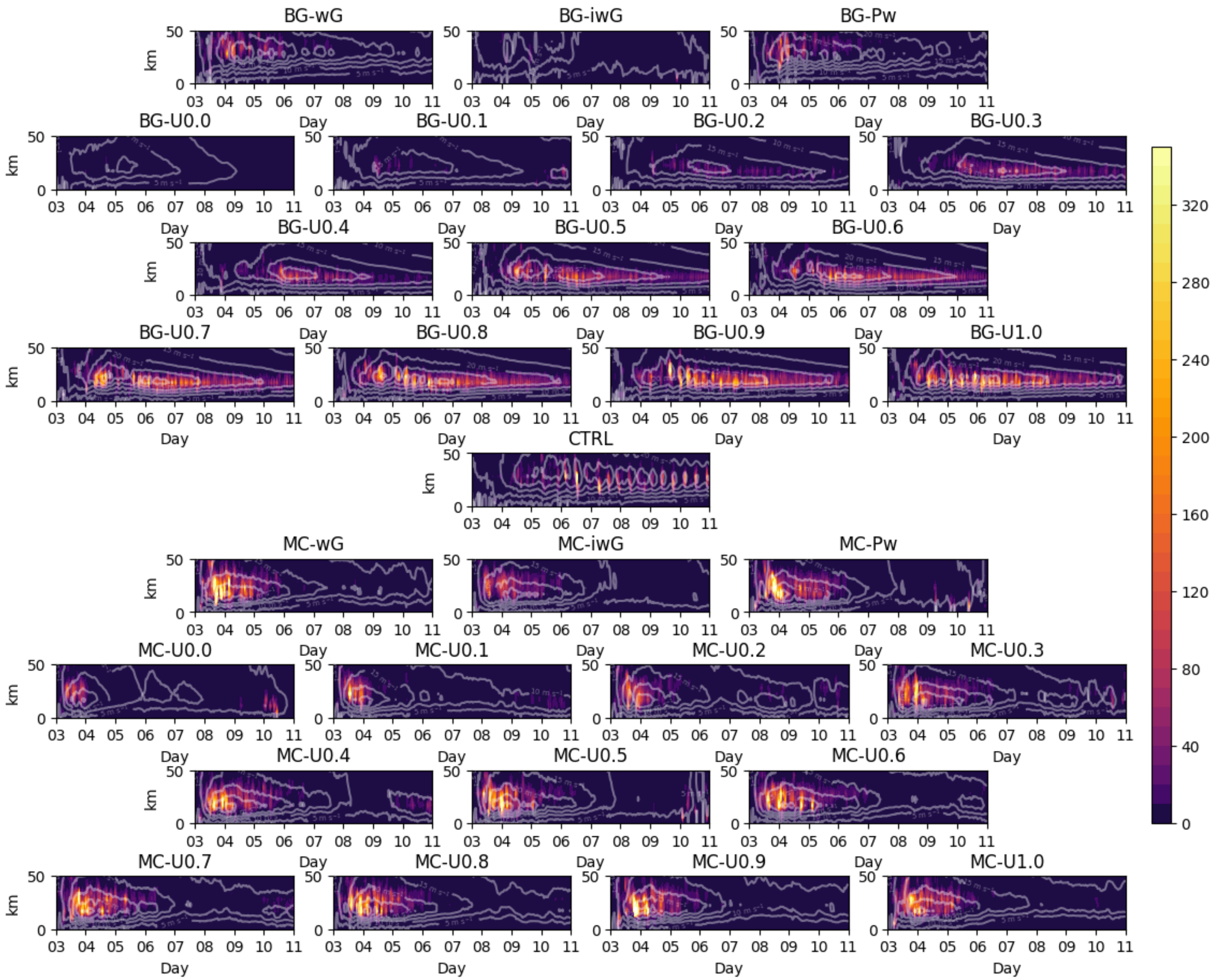

Figure 17: Azimuthal variance of the updraft helicity (shaded) and maximum azimuthally-averaged tangential wind speed (white contours).

Figure 18 shows the FFT magnitude of potential vorticity at the radius of maximum potential vorticity at 850 hPa, temporally averaged over the late period similar to Gentry and Lackmann (2010). The influence of shear from the imposed land surface, which is often attributed to wavenumber 1, increases with SMA in the BG. Notably, the wavenumber 1 maxima between the MC and BG simulations are of a similar magnitude for the higher SMA. The wavenumber 8 asymmetry maxima is larger in the BG simulations than the MC simulations, indicating that the wavenumber 8 VRWs produced are preferentially generated in the BG simulations with the most SMA. The absence of such a local maxima in the CTRL simulation suggests that this feature is unique to the BOE and is suppressed in areas with a greater roughness length. While the cause of this spectral maxima is unknown, it does show a sign of a polygonal eyewall, though overshadowed by the shear and symmetric modes.

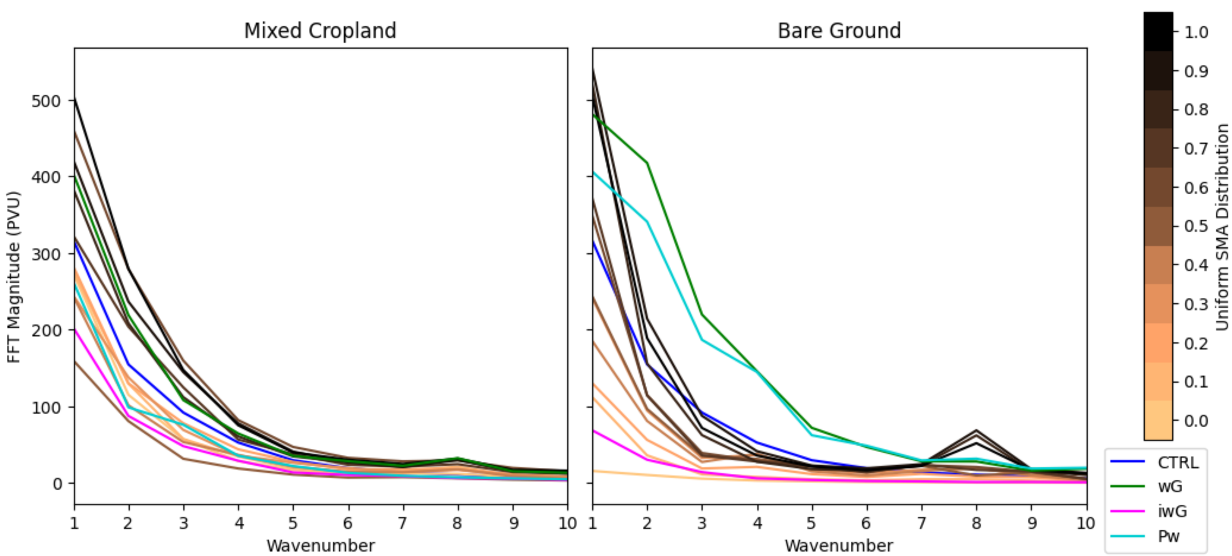

Figure 18: Spectra of the potential vorticity at the 850 hPa radius of maximum potential vorticity.

c. Precipitation mechanism analysis

While the WISHE and VHT analysis focus on the intensity, which is strictly defined as the maximum tangential wind speed, little has been said about the mechanism of describing the precipitation. Although the dynamical features provide the essential characteristics of a TC, the above theories do not apply to precipitation. The VHTs do not persist in the MC simulations, though the total accumulated precipitation accrues. Yet, WISHE requires that the atmosphere is unsaturated even to the extent that the atmosphere may be dry (Cronin and Chavas 2019; Wang and Lin 2020; Mrowiec et al. 2011). A moist-WISHE-like mechanism was proposed for the Madden-Julian Oscillation (Fuchs and Raymond 2017). Instead of either intensity theory, an examination of the neutrally stable similarity theory equations will show that the moisture flux increase in response to the roughness increase is mathematically predicted. The formula for such sensitivity is

$$\frac{\partial \overline{w'q'}}{\partial z_0} = \frac{\overline{w'q'}}{z_0 \left[\log \frac{z_{ref}}{z_0}\right]}$$

where $\overline{w'q'}$ is the kinematic moisture flux, z_0 is the roughness length, and z_{ref} is a reference height. The value of this sensitivity at a reference height of 2 m is shown in Figure 19. The full derivation can be found in Appendix B. A similar derivation can be found in Quintanar et al. (2016), which examined the impact of roughness length on surface heat fluxes in convective environments, which implicitly ignores the neutrality assumption. Similar arguments have been made concerning the precipitation decrease in deforested areas (da Rocha et al. 1996; Hasler et al. 2009; Sud et al. 1996; Sen et al. 2004). The assumption of neutral stability is not valid near the core and over the driest simulations but is otherwise acceptable as shown in Figure 20. This justifies the higher quantity of moisture flux in the MC simulations than the BG simulations. Moreover, this also indicates that the sensitivity of the moisture flux to roughness length decreases with increasing roughness length, which explains the large jump between the CTRL and other simulations. Furthermore, the sensitivity increases with increases in SMA. Therefore, the latent heat flux will be more sensitive to changes in surface roughness where SMA is larger. This is not a unique idea as indicated in Chen and Zhang (2009) among the other references in this section.

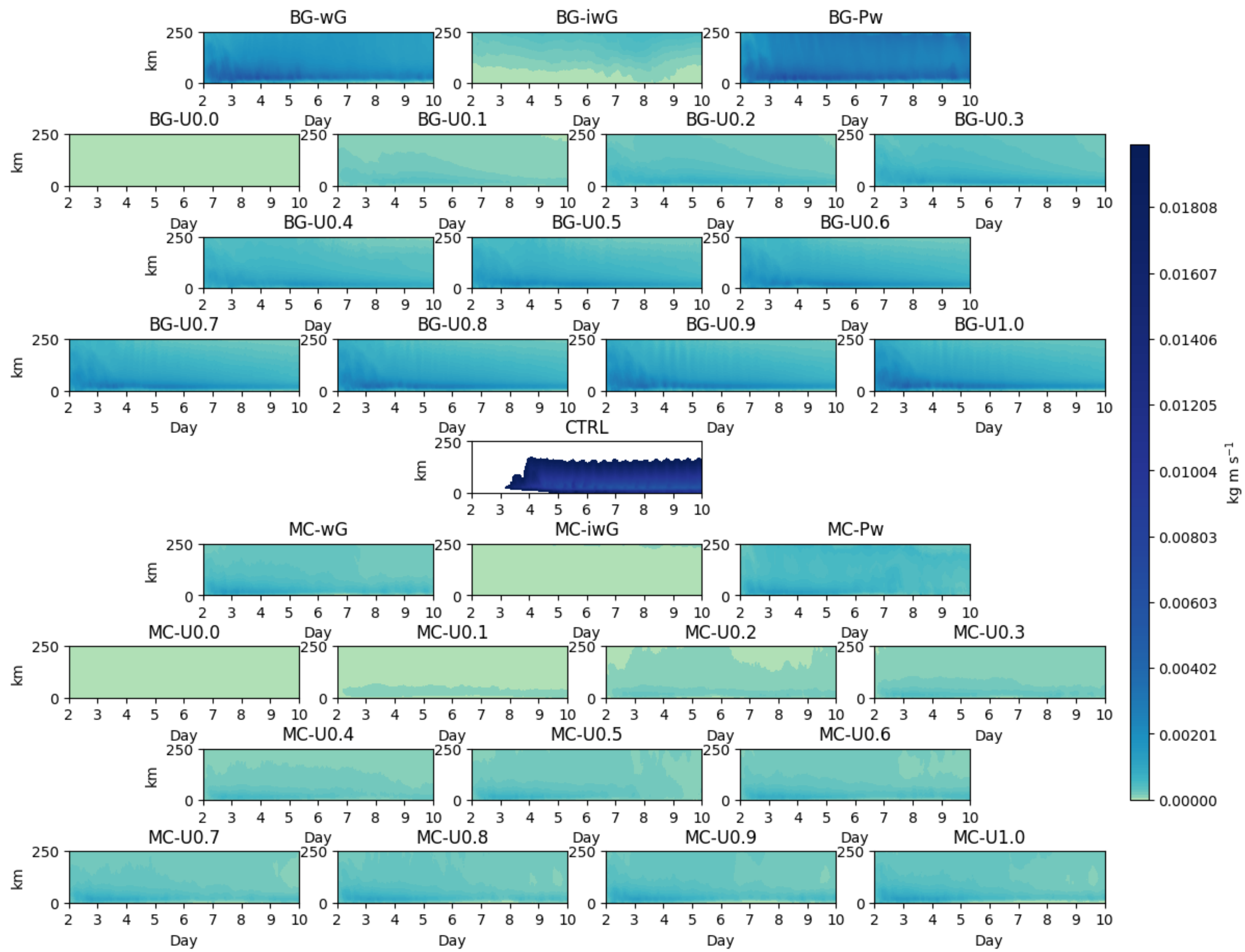

Figure 19: Sensitivity of the latent heat flux to surface roughness length at a reference height of 2 meters.

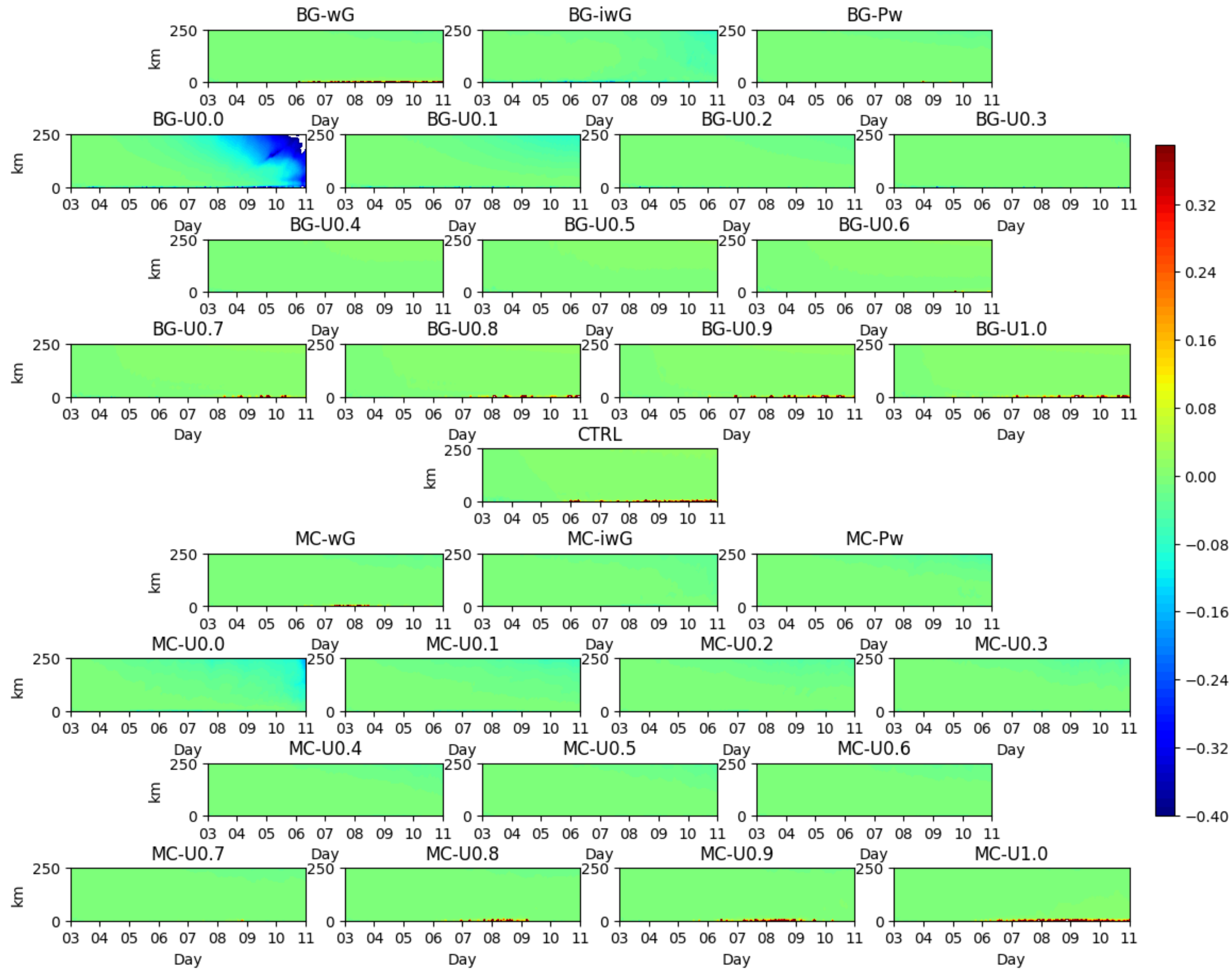

Figure 20: Azimuthally-averaged inverse Monin-Obukhov length.

Since it has been established that surface moisture flux increases with roughness length, then the water vapor mixing ratio increases. With the increase of water vapor mixing ratio comes the increase of hydrometeors and precipitation. Therefore, the sensitivities to SMA and surface roughness are applicable to precipitation by the influence of surface moisture flux. However, the advection of microphysically relevant variables or parameterizations may lead to a relationship that may not be spatially matching. Departing from the assumptions in this study, application of the sensitivity equation does neglect evapotranspiration; therefore it should be applied only in regard to evaporation by turbulence.

D. Conclusions

A series of simulations of TCs that developed over water were imposed over land surfaces with varying surface characteristics, namely roughness and moisture availability. The simulations were examined in the context of the WISHE and VHT intensity hypotheses of TC intensification. As part of the WISHE analysis, an ansatz maximum potential intensity equation was developed. In addition to the intensification analysis, an evaluation of the total precipitation differences was conducted to describe the role that friction has on precipitation.

a. Intensity analysis

Both the WISHE and VHT analysis adequately evaluate the intensity of the idealized TCs. The VHTs and VRWs explain the patterns in the radial-temporal deviations of tangential wind and corresponding composite reflectivity patterns within each simulation. Unlike the VHT analysis, WISHE provided an explanation for an intercomparison of simulations. WISHE also did have some deficiencies such as the reliance on slantwise-neutral convection, which the simulations approached but never reached. Not achieving slantwise-neutral convection may not be an obstacle however, as it is acknowledged that WISHE is supposed to represent a TC that achieved maximum intensity. Other papers have shown such a criteria is achievable (Tao et al. 2019; Wang and Lin 2020). This is not the only problem that may arise. TCs that undergo the BOE require latent heat fluxes to maintain a deep warm core structure, which the BG simulations lack. The warm-core structure, which is generated by diabatic heating of the microphysics, is maintained by the enhancement of the latent heat flux by the roughness length increase. Yet, the increase in latent heat fluxes also implies an increase in condensational warming, which impedes convection. This transition suggests that there is an intrinsic condition within the BOE, which may require rough surfaces to maintain a warm core to be classified as a TC, but at the expense of actual intensification. This is an important augmentation of the original BOE concept put forth by Andersen et al. (2013) and others. However, a rough surface presents another problem in that the diabatic heating from the enhanced latent heat flux can suppress the convection and intensity. Further research will be required to understand the competing aspects of these two factors.

While WISHE may have appeared to be the best candidate for explaining the BOE, significant modifications are needed for MPI to function. Otherwise, the surface saturated entropy difference decreases with increasing SMA, which is contrary to the very basis of the BOE. The modification used here considers not just the difference between the saturated and unsaturated entropy but a modified version considering SMA. The resulting equation is a version of MPI that reflects the premise of the BOE— a version of MPI where the intensity increases with SMA as opposed to decreases with SMA. The ansatz MPI is not without flaws, however, as it does tend to promote superintensity in the early period. This is analogous to a TC that is stronger than the MPI of the surface is able to support. Additionally, due to the lower outflow in the MC simulations, a different way of evaluating the outflow temperature had to be established.

b. Precipitation Analysis

While not required to describe the precipitation variation to achieve the intended result, we decided to include a small description of some of the precipitation metrics. While the assumption of neutrality may be dubious, we have shown that it is largely satisfied in this particular study. In other studies that rely on convective instability (Quintanar et al. 2016), such an equation may be inappropriate. From the derived equation, this suggests that while increasing the roughness length may increase the latent heat flux, the amount that it increases diminishes with increasing roughness. As a practical application, this means that building larger buildings in urban areas will increase precipitation less than planting crops on a flat terrain. But this also means that cities, which are already prone to increased rainfall (Shepherd 2005) and SMA, may see increased sensitivity to roughness length, promoting increases in evaporation and precipitation.

The dependence on the surface moisture flux for inland TC precipitation also implies necessary modifications to existing rainfall mechanisms. The Tropical Cyclone Rainfall (TCR; Lu et al. 2018; Zhu et al. 2013) mechanism focuses on the moisture flux but at a reference height. Our result suggests that the focus of the TCR model should instead be on the surface moisture flux to capture the maximum amount of precipitation. While doing so may underestimate any advected environmental moisture (e.g. Yoo et al. 2020) and have the spatial structure warped by advective processes, a precipitation rate analog to the MPI is possible. There is one additional deviation to the TCR model that was found in our study. The convergence (not shown) generated by the land surface was not markedly different between the CTRL simulation and the other simulations. This excludes convergence as a possible mechanism for achieving an intense steady state, as proposed by older hypothesis, the conditional instability of the second kind (CISK; Charney and Eliassen 1964), which was already demonstrated to not be dependent on surface enthalpy flux coefficients (Craig and Gray 1996).

c. Implications for forecasts

While BOE TCs are uncommon, understanding the land surface and the subsequent atmospheric interactions are critical for gauging the inland impact of any TC. For forecasters, especially long-range forecasters, the ansatz-MPI may adequately describe the intensity the TC may sustain due to the BOE. That is, if the ansatz-MPI is large, then the SMA and enthalpy flux may provide an estimate for the TC. Testing on known BOE storms as well as transitioning or dissipating TCs will be required before implementation. This ansatz-MPI is inadequate in describing the BOE in its entirety. Inland developed areas, including agricultural and forested areas, are more prone to flooding than wind damage. Thus, a wind-based metric for quantifying the precipitation potential is insufficient by itself. Alternatively, more precipitation-based metrics are appropriate.

While precipitation-based metrics do exist, they often have some challenges which makes them not as easy to quantify for this research. Recently, the Extreme Rain Multiplier (Bosma et al. 2020) as well as the Wet-Millimeter Day (Shepherd et al. 2007) were developed, but such metrics are region/climatologically-dependent and therefore cannot be applied to the idealized simulations. Another index, the Hurricane Hazard Index (Jordan and Clayson 2008) is as useful as the Saffir-Simpson scale in that the only addition is the storm surge, and not freshwater flooding. A precipitation scale that is sufficient to describe the BOE will need to be non-regionalized and ideally understandable to the public. But the development of such a criterion is crucial for developing a BOE index for precipitation.

CHAPTER 4

A CLIMATOLOGICAL DIAGNOSTIC TOOL FOR INLAND TROPICAL CYCLONE AND MAINTENANCE EVENTS[1]

[1]Thomas A.M., and J.M. Shepherd 2021. To be submitted to *Frontiers in Earth Science*

A. Introduction

After tropical cyclones (TCs) make landfall, it is often assumed that the wind speeds decay, and damage is reduced. There are two types of progression that an inland tropical cyclone may take: extratropical transition (ET; Keller et al. 2018; Jones et al. 2003; Evans et al. 2017) or dissipation (Kaplan and Demaria 2001; Shen et al. 2002). One exception to this categorization is the observation that some TCs intensify or maintain intensity while inland, albeit not indefinitely (Brauer et al. 2021; Andersen and Shepherd 2014). These events are called TC Maintenance or Intensification (TCMI) events by Andersen and Shepherd (2014; hereafter referred to as AS14). Unlike AS14, the central pressure criteria was not considered. Decreases in pressure could be without meaning if the environmental pressure, which IBTrACS does not record, decreases proportionally thereby sustaining the pressure gradient. Often, the “Brown Ocean” effect (BOE), which hypothesizes that enhancements in surface enthalpy fluxes induced by antecedent soil moisture support the TC, is attributed or associated. Examples of these events include, but are not limited to, Tropical Storm Erin (2007; Evans et al. 2011; Kellner et al. 2012; Monteverdi and Edwards 2010), Tropical Storm Bill (2015), and an unnamed Tropical Depression in 2010 (Nair et al. 2019). The BOE may be a factor in non-TCMI events, as the surface roughness may reduce the intensity but increase the precipitation (see Chapter 2). That is, despite the presence of soil moisture and enhanced latent heat fluxes, the surface wind is still constrained by the properties of the surface.

The number of TCMI events is not limited to these studies. Rather, those studies are only instances of the BOE. A similar study, Andersen and Shepherd (2014; hereafter AS14), examined previous TCs to identify characteristics of TCMI events not found in ET events. AS14 considered the 1-month antecedent values of latent heat flux and supporting components.

However, as Chapters 2 and 3 suggests, the immediate surface conditions have a large impact on the resulting structure of the TCs not just the environment of the previous month. In this study, the analysis will focus on the immediate environment of each location that TCMI events occurred and did not occur.

Section 2 describes the methodology used to identify TCMI events and describe a prototypical machine-learning model. Section 3 investigates the cross-validation of similar machine-learning models, as well as instances where the prediction and dataset do not match. Section 3 will also examine previously unexamined TCs. Section 4 explores potential uses of the machine-learning model, as well as potential pitfalls of the model.

B. Data and Methods

TC location and intensity data were obtained from the International Best Track Archive for Climate Stewardship dataset (IBTrACS; Knapp et al. 2010, 2018). Of those TCs, only those that occurred since 1980 were considered as that is the limit of the Modern-Era Retrospective analysis for Research and Applications, Version 2 (MERRA-2; Gelaro et al. 2017), which was used for the environmental conditions. Of the variables in MERRA-2, only the Single level variables (SLV), flux variables (FLX), and land variables (LND) were considered. Not only were the variables at the time of the strike considered, but the variables 24 hours prior were used.

Each datum that occurred 350 km away from the coast was considered, similar to AS14. Unlike AS14, however, this study does not compare ET events with TCMI events but rather TCMI events and TCs that decay. As long as the datum and the following datum's 'nature' were classified as a Tropical Storm or Disturbance, the datum was still categorized. The classification of the following datum is important as neglecting such a criterion may mean a mis-categorization of a TCMI storm as a TC undergoing ET. The change in the maximum wind speed (MWSPD, or 'usa_wind' in IBTrACS) between the previous time and next time, a time span typically of 6 hours, were calculated using centered differencing. If the MWSPD difference was greater than or equal to 0, the datum was classified as a TCMI event. If the MWSPD-change criteria were not met, the datum was classified as a non-TCMI event. If the datum occurred in the North Atlantic basin, it was used to test the developed machine-learning model. Otherwise, the datum was used to train the model coefficients. The data for TCMI and non-TCMI storms were consolidated by averaging the environmental variables of TCMI and non-TCMI events. This consolidation prevents the observational independence assumption of logistic regression models from being violated.

The function used to create the machine learning model was the "Logit" function in statsmodels (Seabold and Perktold 2010). Candidate machine-learning models were developed iteratively going through pairs of unmatched, potentially relevant variables to identify candidate variables for a final prototype machine-learning model, which was initialized as an empty set. Then the accuracy of each variable pair for both the test and training dataset was evaluated and stored under the condition that the variance inflation factor (VIF) was less than or equal to 10 (O'Brien 2007). If a variable in the variable pair is included in the candidate variables, it is excluded for the test.

Afterwards, the most accurate candidate machine-learning models were selected. The accuracy metric utilized is the average of the Peirce Skill Score (Manzato 2007; Peirce 1884) between the test and training dataset subtracted by the absolute difference, with the same process applied to the Clayton Skill Score. Optimizing just the Peirce Skill Score with a difference penalty produced reasonable values of other skill scores with minimal difference between the testing and training datasets. The subtraction of the absolute difference is to penalize overfitting of the training dataset. The most frequent variable that was shown in the most accurate candidate machine-learning models was used to train the next iteration of candidate machine-learning models, though the variable was excluded if the most frequent variable appeared previously in the set of candidate variables. The exclusion of a candidate variable may not always indicate that the machine-learning model is necessarily less accurate but may be a result of a reduction in the VIF. After the Peirce Skill Score was optimized, variables with a p-value greater than 0.6 were removed.

While the prototypical machine-learning model may be useful for identifying TCMI events, it is not without flaw. On a dynamic note, the machine-learning model does not account for external influences, including localized intensification due to surface features, or horizontal influences. For example, Cyclone Kelvin (2018) has been shown to have maintained a warm core (Shepherd et al. 2021) over land but was more influenced by the horizontal advection of moisture rather than the BOE (Yoo et al. 2020). This may be the reason that the prototypical machine-learning model missed the TCMI of Kelvin. Along a similar line, this prototypical machine-learning model does not include extratropical cyclones, which derive energy from baroclinicity (Evans et al. 2017; Keller et al. 2018). Intensification due to the influence of surface features and topography (Coch 2020; Miller et al. 2013) are also not considered.

The criteria allowed for a small number of non-North Atlantic storms (93) and an even smaller number of North Atlantic TCs (65) so the amount of data used to train and test the machine-learning model is very limited. Of those limited number of TCs, there were 40 TCs in the North Atlantic basin and a total of 20 TCs in other basins that were counted as both non-TCMI and TCMI cyclones. This may mean that more stringent criteria for discriminating between TCMI and non-TCMI events, beyond wind speed, may be necessary. Other choices, such as excluding subtropical cyclones, is open for critique. One criteria for TCs to be consideration that may be relaxed is the 350 km buffer from the coast, suggested by Andersen and Shepherd (2014), which excluded TCs such as Hurricane Gaston (2004; Franklin et al. 2006) and Tropical Storm Helene (2000; Franklin et al. 2001) from being considered. The spatial criteria also does not prevent the TC under consideration from being influenced by the oceanic environment (Yoo et al. 2020).

C. Results

a. Statistical Model

Table 5 provides a summary of the final prototypical machine-learning model. Variables ending with the suffix ‘Prev’ refer to variables from 24 hours prior. For reference, the equation for a logistic regression model is

$$P = \left(1 + \exp\left[-\beta_0 - \sum_{i=1}^{N} \beta_i x_i\right]\right)^{-1}$$

where P is the probability of an event occurring, β_0 is the constant, β_i is the i^{th} coefficient corresponding to the i^{th} variable. While the pseudo-R squared of 0.1727 may be underwhelming, the other statistical measures of accuracy, described in Table 6 are more optimistic. The relatively small Brier Skill Score indicates the need to assign a reference probability to discriminate between TCMI and non-TCMI events. The probability that was used to discriminate between TCMI and non-TCMI events was a naïve probability of 50%. There is a bias towards overpredicting TCMI events as indicated by the False Alarm Rate for both datasets being over 50%. Adjustment of the naïve reference probability of 50% may change the Probability of Detection but also may increase the False Alarm Rate.

A positive coefficient indicates that the variable has a tendency towards promoting a TCMI event, while a negative coefficient is indicative of a reduction in the likelihood to a TCMI event. The magnitude of the coefficients is less relevant than the sign as the data was not normalized, so the coefficients have units. The positive coefficient with buoyancy scale (BSTAR) is indicative of the influence of the WISHE mechanism on the occurrence of TCMI events. The coefficient associated with the previous day accumulated precipitation (PRECTOTPrev) indicates recently wetted soil, which may be promoting the BOE. Comparing PRECTOTPrev to the 3-hour accumulated precipitation at the analysis time (PRECTOT), which have the same units, suggests that previously day precipitation is more indicative of a TCMI event than the precipitation of the TC. The coefficient associated with the planetary boundary layer height, both from the previous day (PBLHPrev) and at analysis (PBLH), implies that less turbulent mixing increases the probability of a TCMI event. While this may not directly be associated with the BOE, the influence of buoyancy is indicative of enhanced soil moisture. The meaning of the opposite sign between the coefficients associated with the previous day meridional wind (V250Prev) and the meridional wind at the analysis time (V250) is unknown, but there may be some level of bias within the wind variables based on the gradient wind balance and TCs in opposite hemispheres.

Table 5: Description of the machine-learning model and the constituent coefficients.

Variable Name	**Coefficient**	**Standard Error**	**p-value**	**Coefficient units**
const	0.5955	1.051	0.571	N/A
BSTAR	461.686	194.405	0.018	$s^2\ m^{-1}$
PBLH	-0.0012	0.001	0.199	m^{-1}
V250Prev	0.095	0.049	0.052	$s\ m^{-1}$
PBLHPrev	-0.0009	0.001	0.275	m^{-1}

H1000Prev	0.0076	0.008	0.323	m^{-1}
BSTARPrev	79.2888	119.757	0.508	$s^2\ m^{-1}$
V250	-0.0826	0.06	0.167	$s\ m^{-1}$
PRECTOTPrev	1597.887	911.807	0.08	$kg^{-1}\ m^2\ s$
U10M	0.1557	0.083	0.062	$s\ m^{-1}$
LWLAND	0.0507	0.038	0.18	$W^{-1}\ m^2$
PRECTOT	370.3106	267.323	0.166	$kg^{-1}\ m^2\ s$

Table 6: Contingency Analysis and Brier Score of the machine-learning model on the test dataset and training dataset.

Metric	Test	Train	Reference
Percentage of Hits (A)	25.24%	9.91%	N/A
Percentage of False Positives (B)	12.62%	1.8%	N/A
Percentage of Misses (C)	24.27%	17.12%	N/A
Percentage of Correct Negatives (D)	27.86%	71.17%	N/A
Climatological Probability of a Single TCMI event	49.51%	27.03%	N/A
Probability of Detection	51%	36.66%	Doswell et al. 1990; Wilks 2006
False Alarm Rate	25%	2.5%	Wilks 2006
Clayton Skill Score	0.276	0.6523	Clayton 1927, 1934; Wilks 2006
Brier Skill Score	0.2606	0.1566	Brier 1950; Wilks 2006
Odds Ratio	3.12	22.87	Stephenson 2000
Heidke Skill Score	0.1302	0.2081	Heidke 1926; Wilks 2006
Peirce Skill Score	0.2598	0.342	Peirce 1884; Wilks 2006
Equitable/Gilbert’s Skill Score	0.1497	0.3827	Gilbert 1884; Wilks 2006

b. *Verification Composite*

Figure 21 shows the sea level pressure (SLP) relative to the IBTrACS location averaged over the contingencies produced by the prototype machine-learning model. The centeredness is indicative that the TC position is represented well by MERRA-2. The central and environmental pressures are lower in the non-North Atlantic dataset than the testing dataset, indicating a systematic difference between the datasets. There are a couple of other systematic differences between the training and testing datasets. Another systematic difference is the roughness length (Figure 22), which is larger in the North Atlantic basin than in the other basins. It should be noted that in both datasets but particularly the training dataset, the number of constituent storms that had false positives is limited, which emphasizes individual storm characteristics. Cyclone Naomi (1993) and Cyclone Yasi (2011), which progressed over the sparsely vegetated Australian interior, were the only TCs that were false positives in the training dataset leading to a systematic difference in the roughness length. Both the systematic difference in SLP and Z0M lead to systematic differences in the maximum wind speed (SPEEDMAX; Figure 23). The average storm that underwent TCMI had a lower SPEEDMAX than the storms that did. The eastern maxima in SPEEDMAX is due to the compound effect of the translation velocity and gradient wind balance.

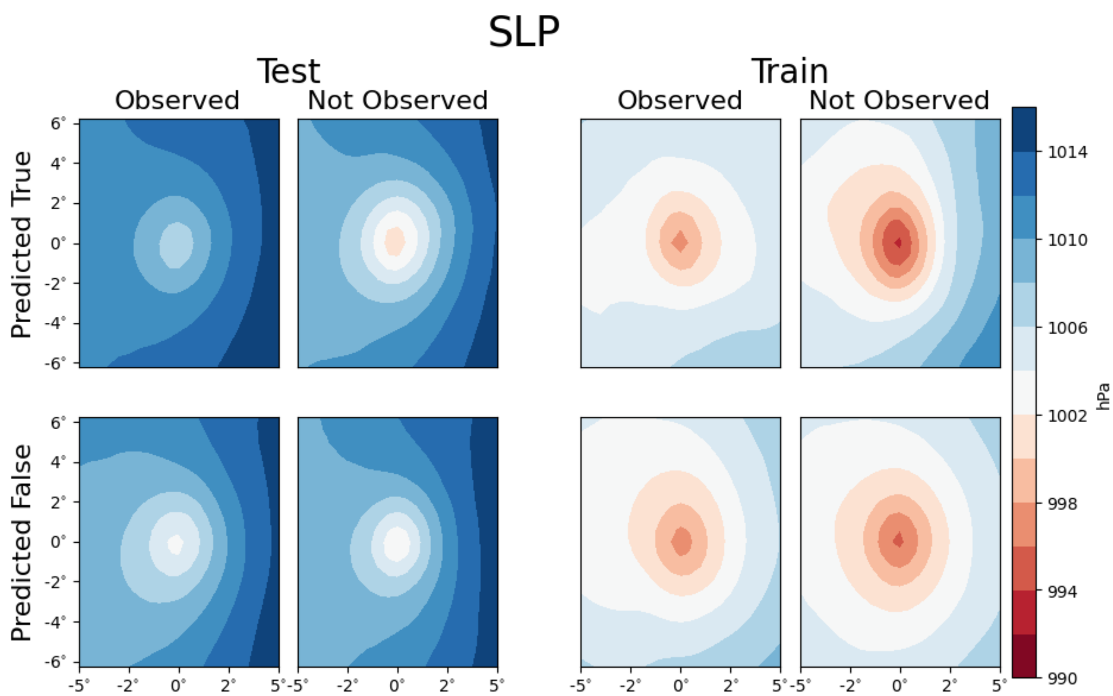

Figure 21: Composite mean sea level pressure (SLP) for all of the contingencies of the machine-learning model.

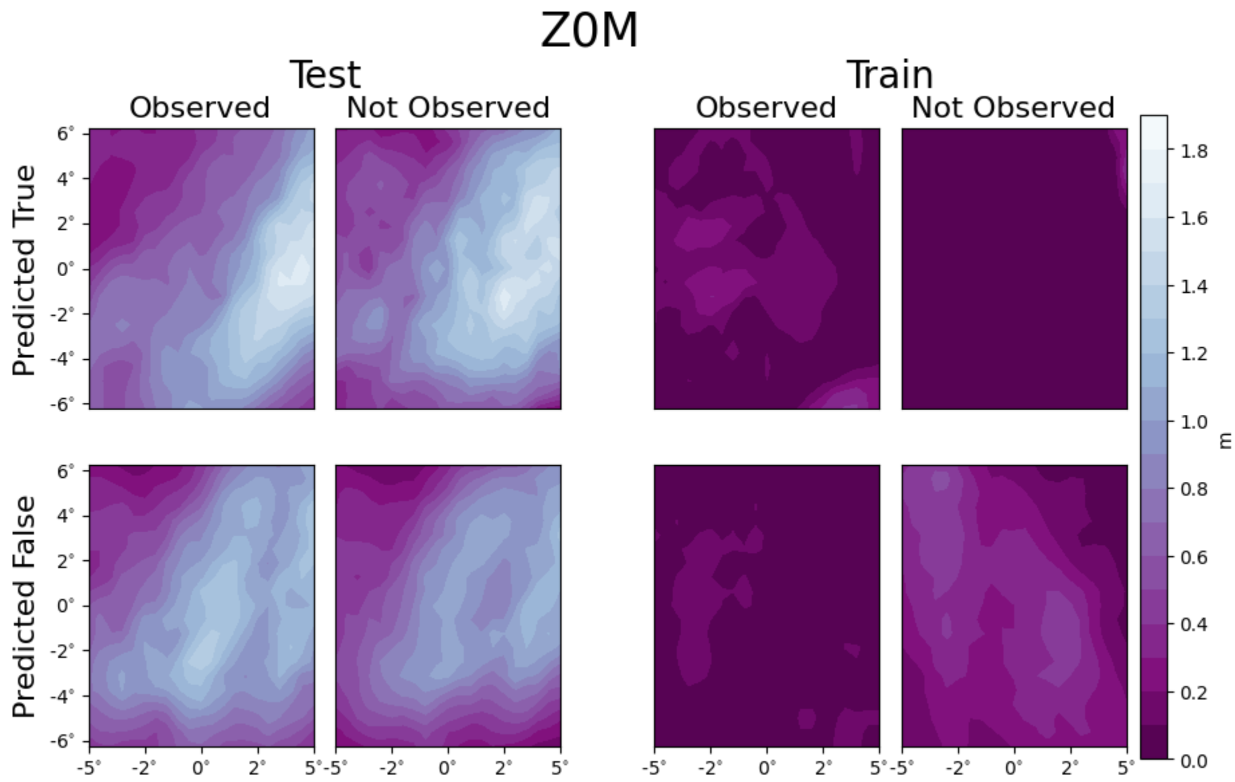

Figure 22: Composite mean of the aerodynamic roughness length (Z0M).

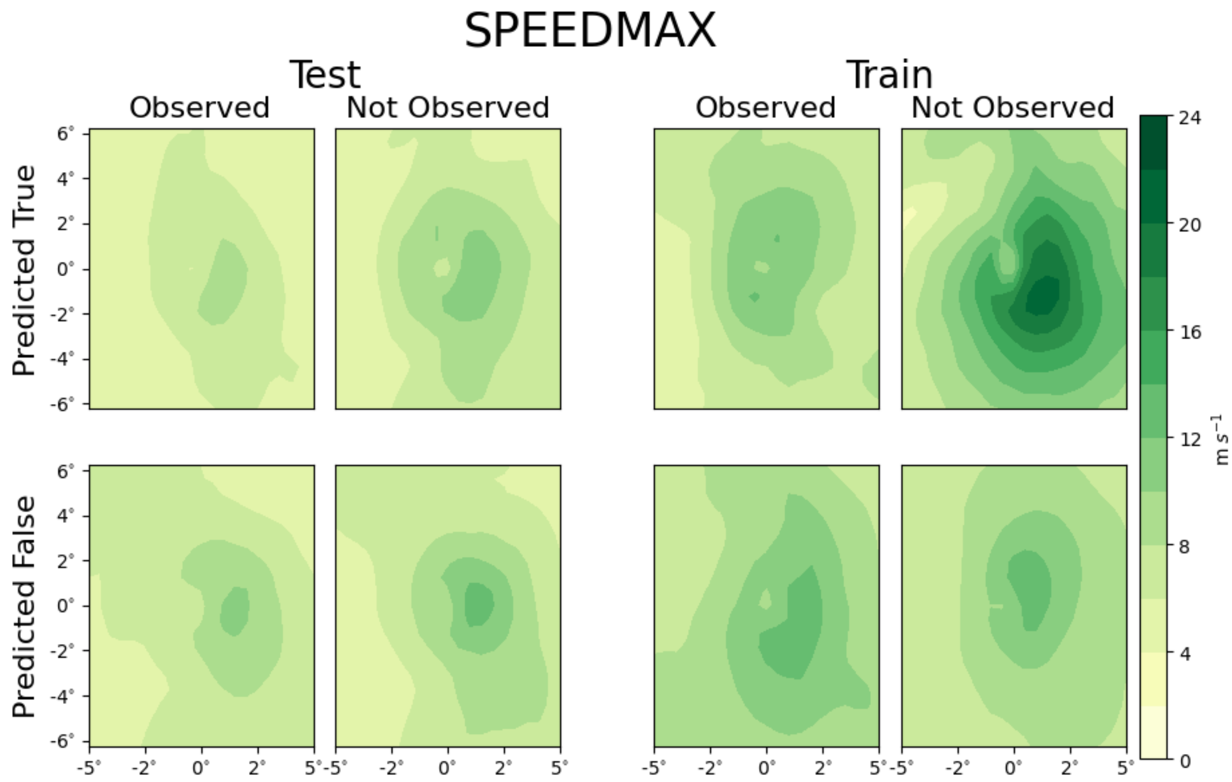

Figure 23: Composite mean of the maximum wind speed (SPEEDMAX).

Figure 24 shows the energy loss flux from interception (EVPINTR). For the testing dataset, the average EVPINTR is a good metric for determining inaccurate diagnoses, while it may improve the accuracy in the training dataset. However, including EVPINTR in the machine-learning model produced a larger p-value than the threshold. From a physical interpretation, EVPINTR is the amount of energy constrained to the surface by the presence of objects on the surface. EVPINTR disrupts the surface energy flux and reduces the buoyancy. This is seen in Figure 5, which shows BSTAR. BSTAR is one of the criteria variables within the machine-learning model that describes the role of the WISHE/BOE mechanism. In the testing dataset, the average BSTAR near the center of the TC is positive only in the hits. This is one way of discriminating between hits and false positives in the North Atlantic basin.

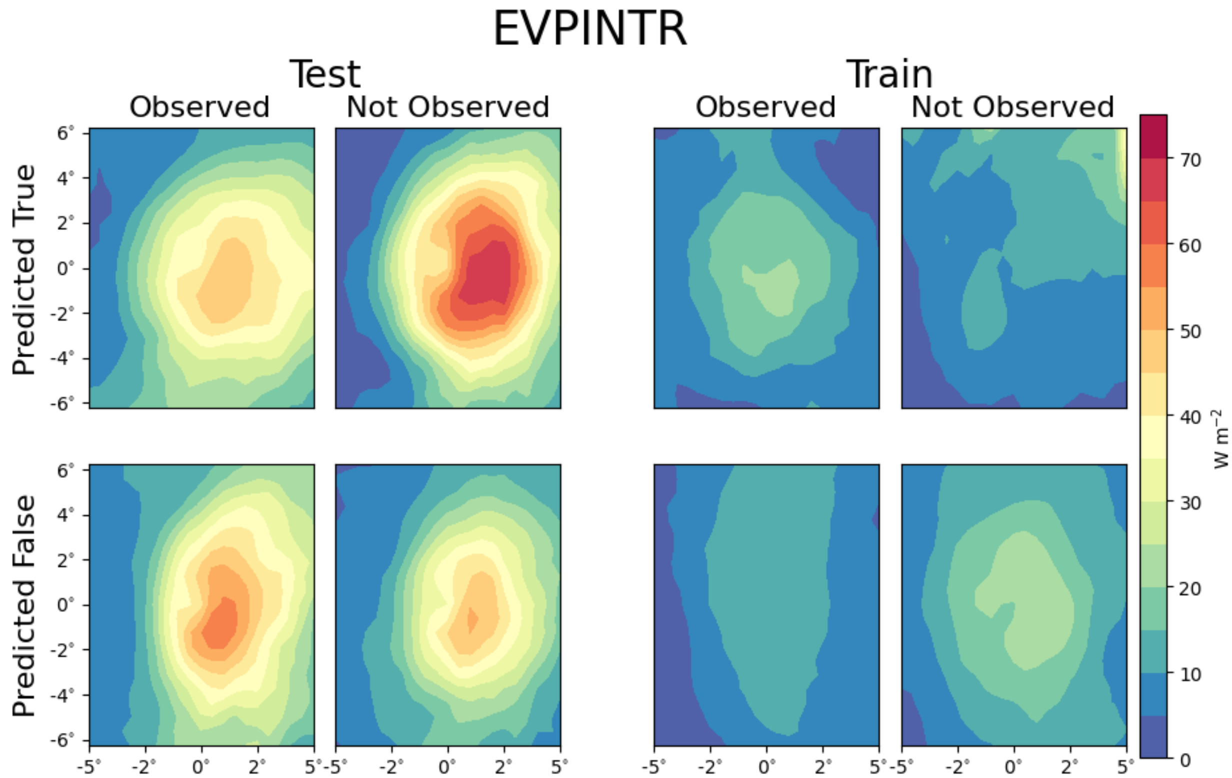

Figure 24: Composite mean of the energy loss flux by interception (EVPINTR).

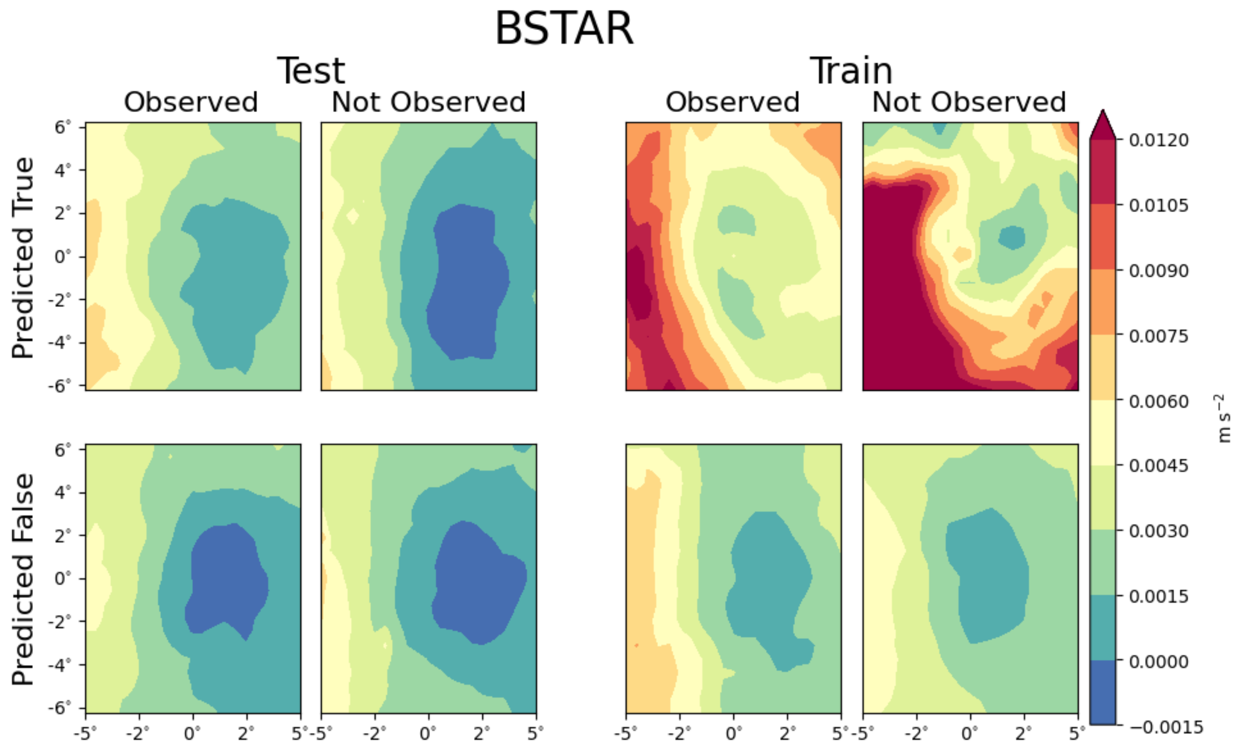

Figure 25: Composite mean of the surface buoyancy scale (BSTAR).

c. *Event Analysis*

1) Discussion

Figure 26 shows a geographical distribution of the machine-learning model performance on the testing dataset. The machine-learning model does not predict TCMI events in southern Mexico even though TCMI events do occur in that region. There are several identifiable storms that have and have not undergone TCMI. Specifically, Tropical Storms Erin (2007) and Bill (2015) are storms that were identified by the prototypical machine-learning model, which are published instances of the BOE (Evans et al. 2011; Kellner et al. 2012; Arndt et al. 2009; Brauer et al. 2021). Appendix C lists other storms that meet the TCMI classification. Below, we examine Tropical Storm Hermine (2010), which followed a similar path to Tropical Storms Erin and Bill, as well as Tropical Storm Dolly (2008), which eventually caused flooding in New Mexico.

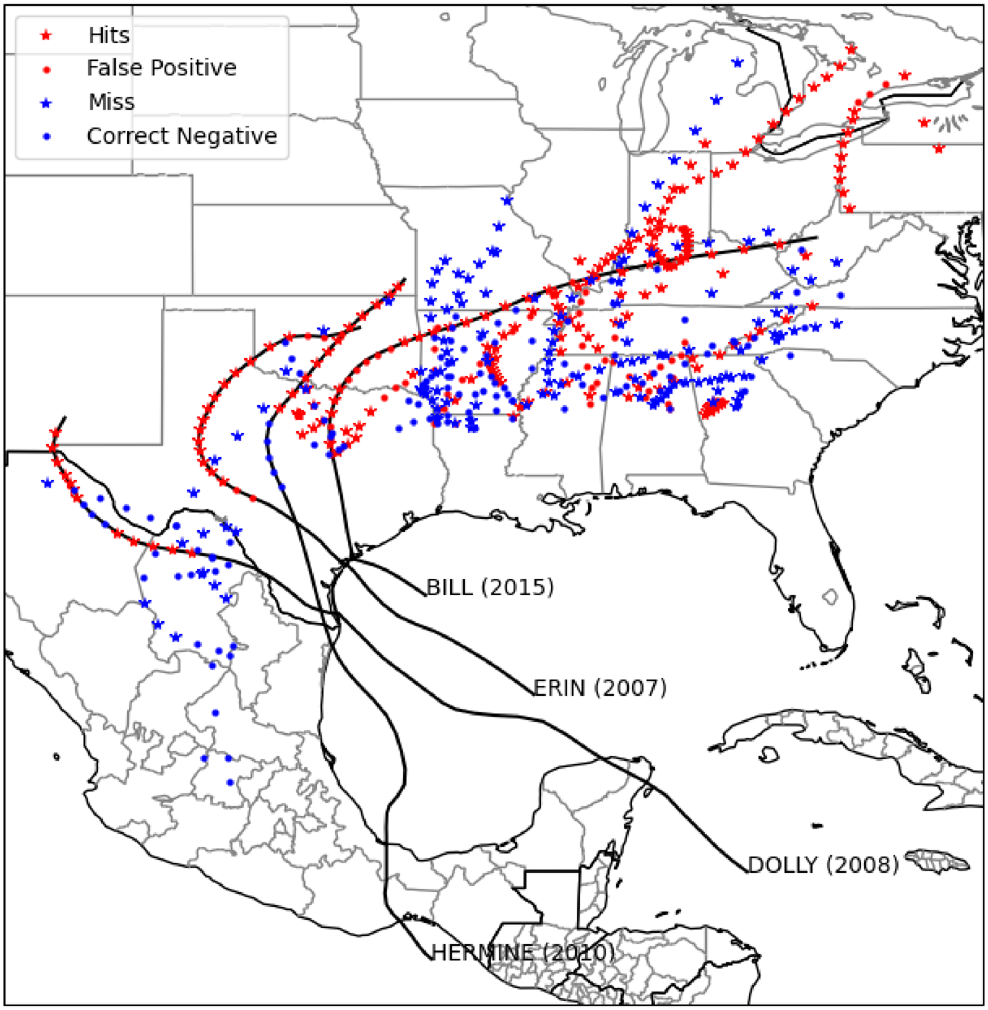

Figure 26: Map of the performance of the machine-learning model.

2) Hurricane Dolly (2008)

Hurricane Dolly (2008) was a hurricane that formed in the western Caribbean Sea on 20 July 2008. After experiencing two brief landfalls near Cancun, Mexico and South Padre Island, Dolly experienced a final landfall on Texas on 23 July 2008 at 2000 UTC. Figure 27 shows the trend in the intensity of Hurricane Dolly. After rapid weakening associated with landfall, Dolly experienced two periods of cyclone maintenance with the first period as a tropical depression and a constant wind speed of 25 kts for 20 hours, and the second period as a low pressure with a constant wind speed of 20 kts for 24 hours before dissipating. The first period had monotonically increasing pressure, while the pressure decreased 2 hPa over 12 hours, but increased by 6 hPa over the next 12 hours.

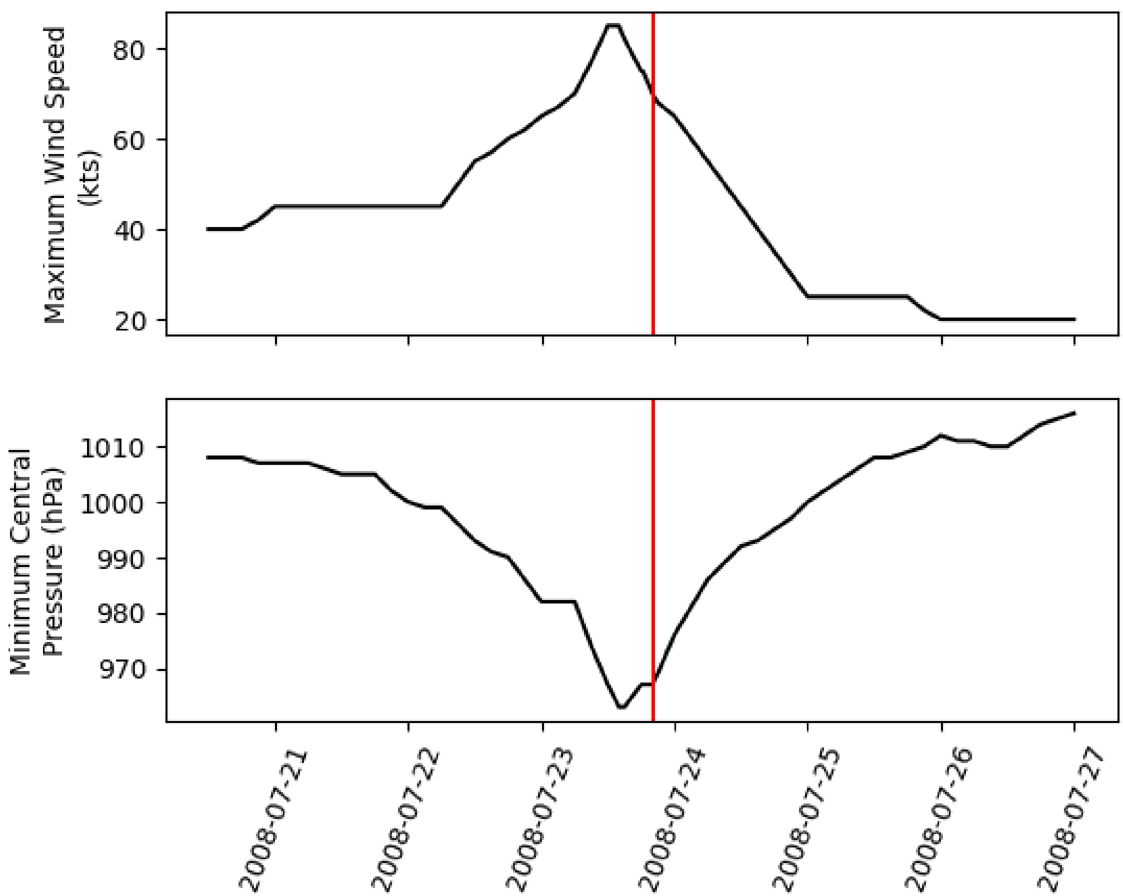

Figure 27: Maximum wind speed (top) and minimum central pressure (bottom) for Hurricane Dolly. The red line depicts the final landfall.

But more than just the characteristic wind speed change, Dolly produced a secondary precipitation maxima (Figure 28) in New Mexico, leading to flash flooding and the death of one person and (National Weather Service (NWS) 2018a). It should be noted that widespread floods impacted New Mexico earlier that month, before Hurricane Dolly, which may qualify as a series of predecessor rain events (PRE; Bosart et al. 2012; Galarneau 2015). This is supported by Figure 29, which shows the time averaged precipitation for the month, prior to final landfall. The machine-learning model did predict a TCMI event. The latent heat flux (shown in Figure 30) criteria of 70 W m^{-2} for the BOE, as suggested by AS14, was not sufficient evidence to predict the TCMI of Dolly, indicating that this tool is an improvement on previous criteria.

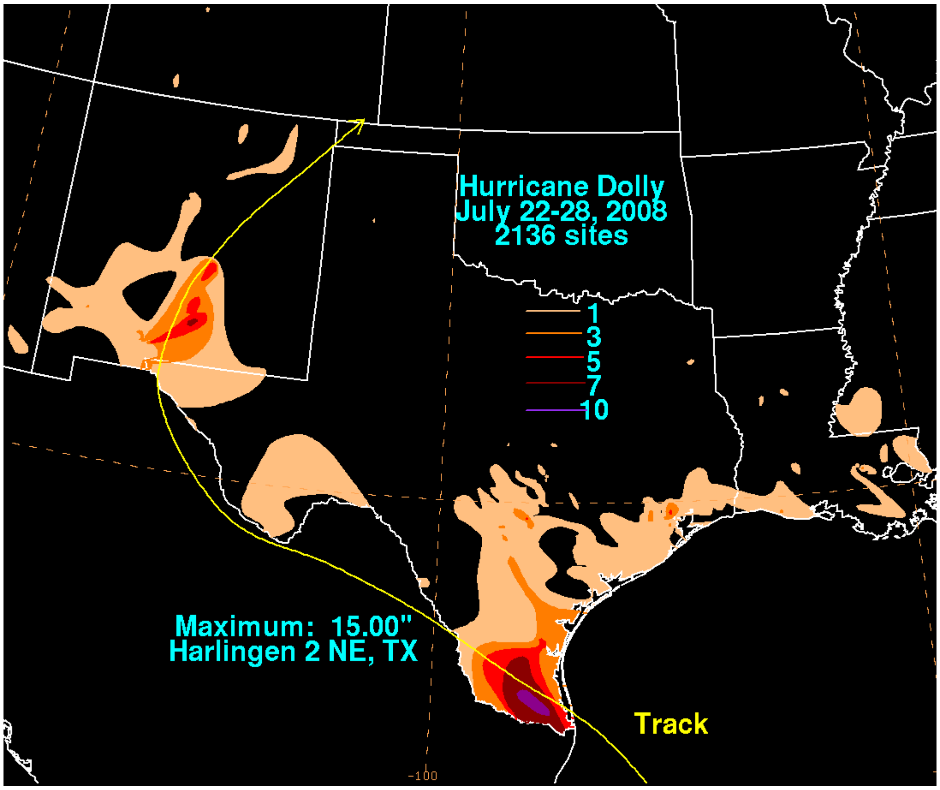

Figure 28: Rainfall associated with Hurricane Dolly in inches. Source: NOAA/NWS (https://www.wpc.ncep.noaa.gov/tropical/rain/dolly2008filledrainblk.gif)

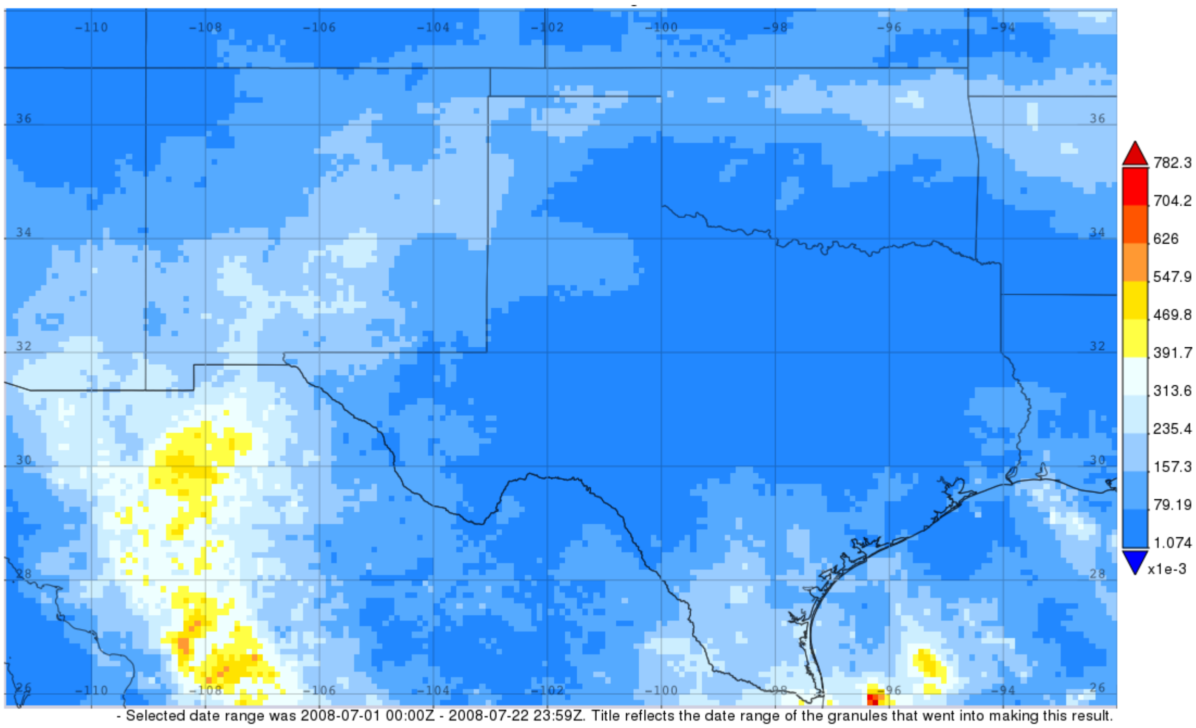

Figure 29: Time-averaged map of the final run of multi-satellite precipitation estimate with gauge calibration prior to the landfall of Hurricane Dolly (2008). Source: NASA Giovanni (Berrick et al. 2009; Acker and Leptoukh 2007).

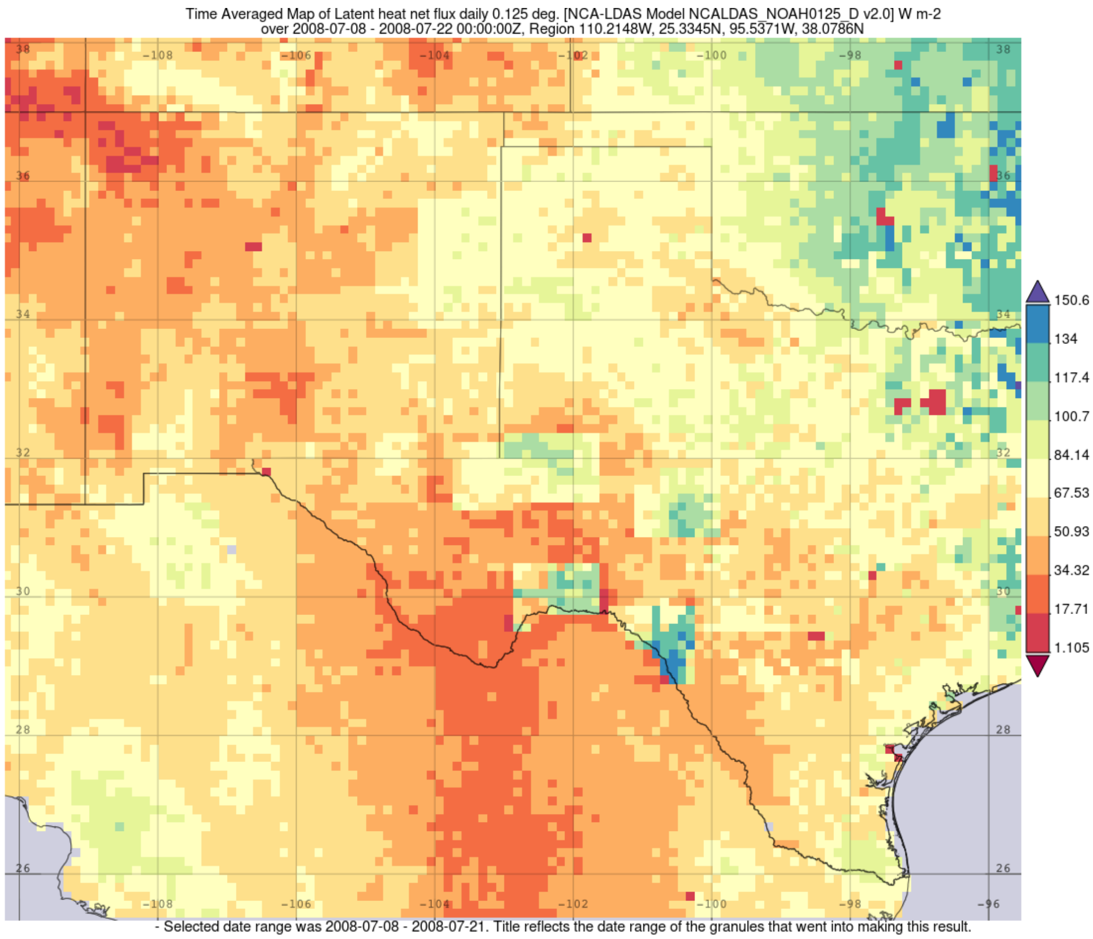

Figure 30: Two week averaged latent heat (W m^{-2}) from the NCA-LDAS model prior to Hurricane Dolly. Source: NASA GIOVANNI

3) Tropical Storm Hermine (2010)

Tropical Storm Hermine (2010) developed within the Bay of Campeche and traveled across to the Gulf of Mexico, making landfall in northeast Mexico at 0200 UTC on 7 September 2010 (Avila 2010). While Hermine lasted only 64 hours as a TC after landfall, 30 of those hours were as a tropical depression at a constant wind speed of 20 kts and a constant central pressure of 1005 hPa. The maximum wind speed and minimum central pressure is summarized in Figure 31.

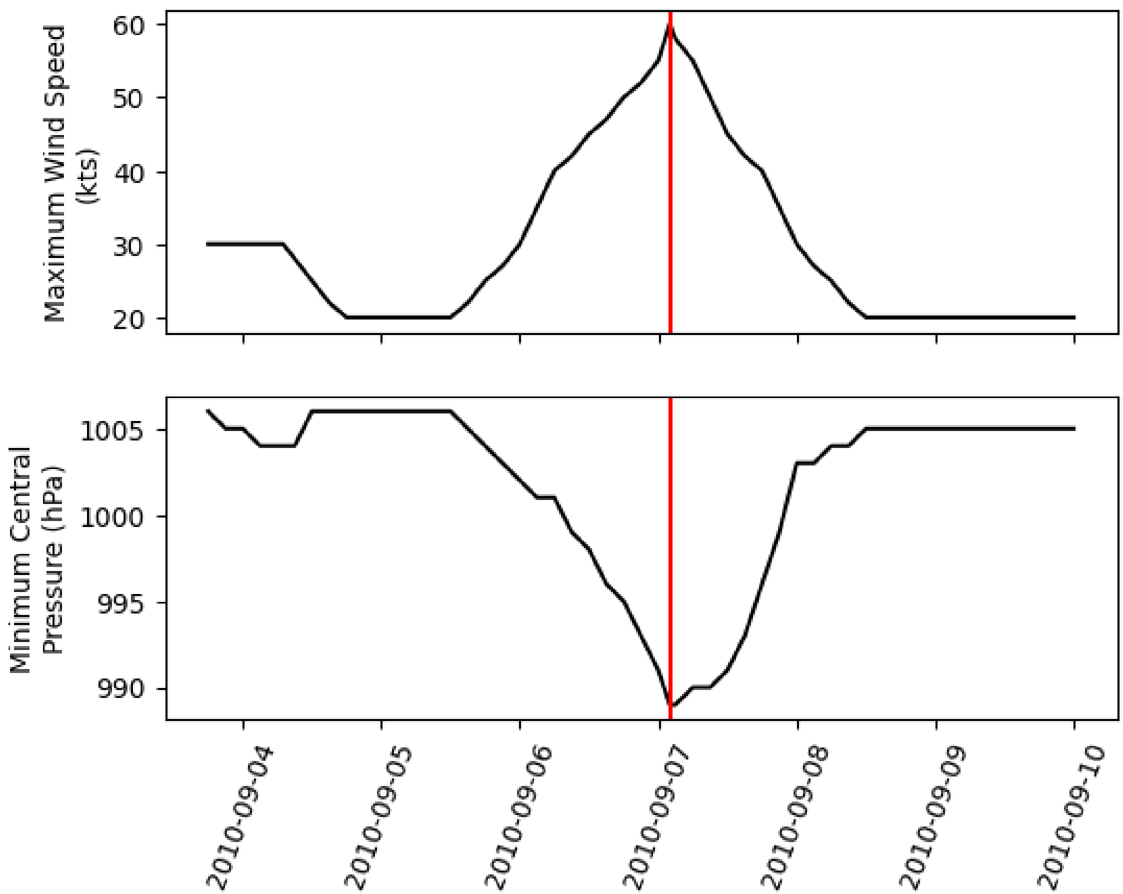

Figure 31: Maximum wind speed (top) and minimum central pressure (bottom) for Tropical Storm Hermine (2010). The red line depicts landfall.

Like Hurricane Dolly, Hermine produced an inland maxima in precipitation, as shown in Figure 32. Hermine was a significant precipitation event, despite it qualifying as a TCMI on the basis of the TC dynamics, as it was the only precipitation event for some areas in September 2010. A severe drought began afterwards (National Weather Service (NWS) 2018b). Despite the severe drought, the two-week averaged latent heat flux, shown in Figure 33, was sufficient to produce a BOE storm. For reference, a two week average 40 W m^{-2} is the criteria value of for the BOE identified by Andersen et al. (2013).

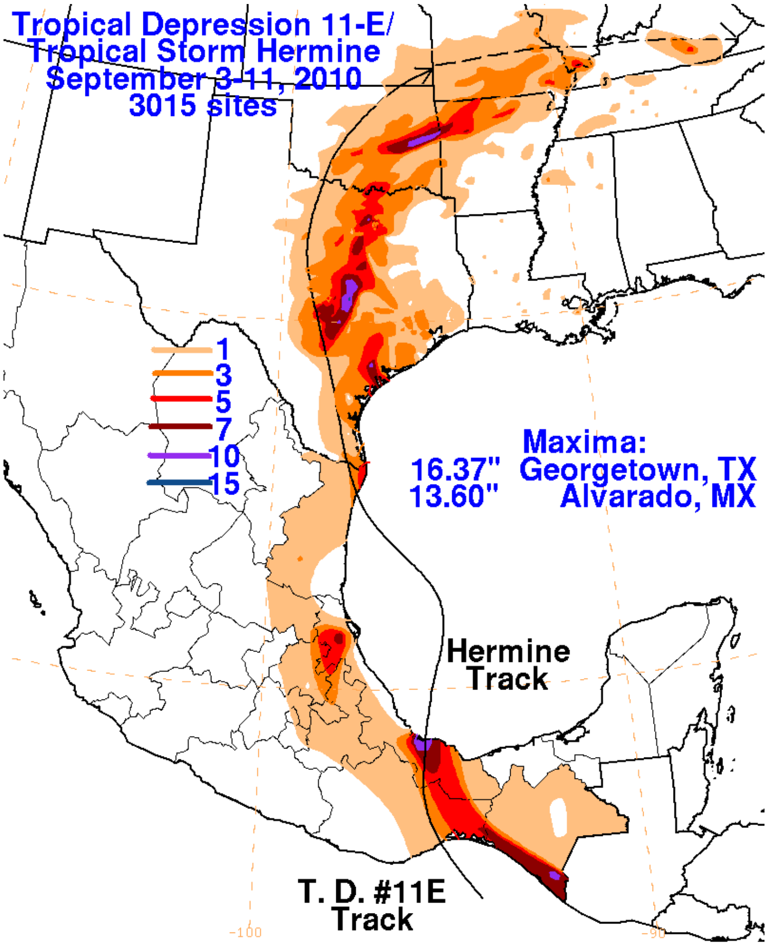

Figure 32: Rainfall associated with Tropical Storm Hermine (2010) in inches. Source: NOAA/NWS (https://www.wpc.ncep.noaa.gov/tropical/rain/hermine2010filledrainwhite.gif)

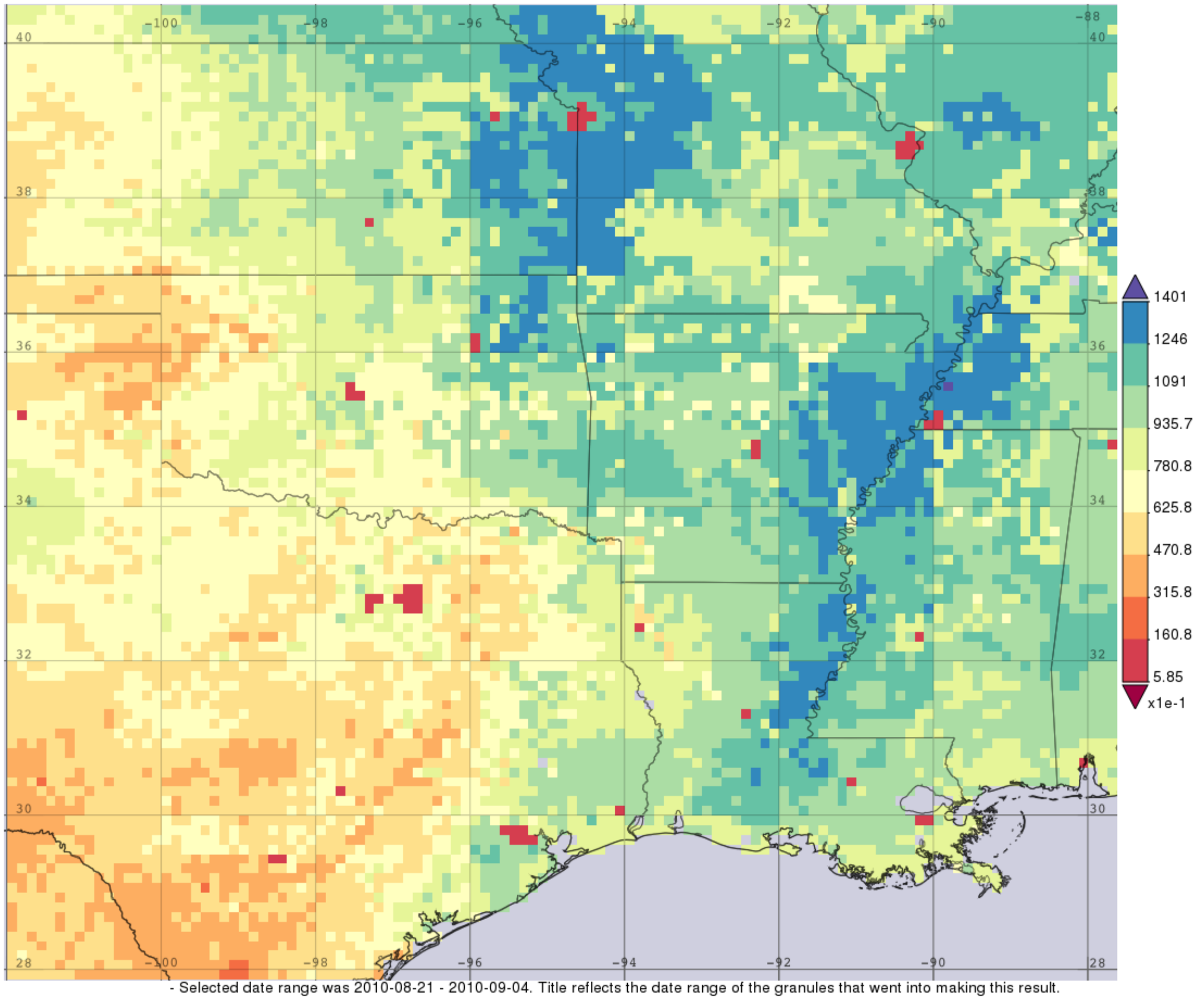

Figure 33: Time-averaged net latent heat flux from the NCA-LDAS model in W m^{-2}. Source: NASA GIOVANNI.

D. Conclusions

A prototypical machine learning model has been developed with variables that were chosen to optimize accuracy rather than any given cause of TCMI. Some variables that were important at the time of storm arrival were important the prior day, which indicates that a TCMI event is a reaction to the environment. Moreover, the variables that were finally selected show a heavy emphasis on land-surface processes, which also indicates that proper modeling of air-land interactions are critical for modeling TCMI events. This supports the idea that the accurate representation of the land surface state is critical to the accurate diagnosis of TCMI.

One aspect of the final machine-learning prototype model that can be criticized is the inclusion of the wind components (U10M, V250, V250Prev). The machine-learning model was trained on data in both the Northern and Southern Hemisphere, respectively, indicating an opposing bias in each due to the opposite signed Coriolis force and opposing rotation. Moreover, the 1000 hPa height from the previous day (H1000Prev) is included, even though it is often masked. However, developing the model without the masked variables still yields a similar subset of variables (including V250 and V250Prev) with similarly signed coefficients within the confidence interval of the original model, though with less accuracy. The role of the shifting meridional wind deserves more study. Moreover, the inclusion of meridional wind shift emphasizes the independence of variable selection without the perceived bias of the TCMI being caused exclusively by the BOE. To clarify, the variables in the final prototype model were chosen not out of preconceived notions of the causes of TCMI but as variables that improve the accuracy of the prototype machine-learning model. This means that variables that are instinctively examined for the BOE were not given priority (such as latent heat flux) but are heavily influenced by those variables.

a. Applicability and Future Use

What has been presented here is a usable prototypical machine-learning model that may diagnose the probability of a TCMI event based on reanalysis data. This probability forecast is effectively a conditional probability of a TCMI event given the inland onset of a TC. If given the probability that an area is to be struck by a hurricane at a given time, this diagnostic method can be applied to determine whether the TC decays or maintains strength/intensifies. This tool may be useful in diagnosing the occurrence of TCMI events in a future climate beyond the simple 70 W m^{-2} latent heat flux threshold suggested by AS14.

Possible future improvements to this statistical model include excluding weaker TCs as well as distinguishing between intensification and maintenance events. Identifying the BOE given a TCMI event through the use of Baye's Theorem is also a potential avenue of identifying specific TCs that underwent the BOE. Another potential improvement is the inclusion of surrounding grid cells or times but at the cost of additional computations and possibly decreasing the physical interpretability. While observations of rainfall are not included in the IBTrACS dataset, satellite observations of the precipitation rate in space may also be employed in to broaden the definition of TCMI beyond the dynamic criteria.

This study provides a list of candidate TCs to study for TCMI events (see Appendix C). More TCs can be considered if the range of dates is expanded to the full selection rather than what is limited by MERRA-2 or if the spatial constraints are reduced. This provides a new set of TCs to be considered as BOE storms for study, instead of morbidly awaiting new TCMI events or questioning any new TC for the potential for the BOE. This study also indicates that, while the BOE is one specific and major cause of TCMI, it is not the only cause.

CHAPTER 5

SUMMARY AND CONCLUSIONS

A. Overview

TCs have a strong impact on society, decimating coastal areas and causing inland flooding. While TCs are presumed to dissipate over land, diminishing the impact with distance from the coast, that presumption is not always true. Sometimes TCs are observed to maintain their strength or intensify, despite landfall. These TCs cause damage far inland, where mitigative measures for TCs may be absent. Previous research on TCs have shown that surface moisture fluxes are influential for these TCs. The research presented here attempts to do three things: 1) identify surface impacts and the impact of surface features, 2) investigate the role of intensification mechanisms in the BOE, and 3) identify previous TCMI cases for future research and the environmental variables.

The first manuscript (Chapter 2) introduces an idealized simulation of a TC over water. After 48 hours a series of simulations are derived from the simulation, each with a different combination of soil moisture profiles and surface roughness length. For the simulations with the smaller surface roughness length, the surface wind speed in the near steady-state is closest to the TC over water. Also, the relationship between surface wind speed and soil moisture is clearest for the smaller roughness length. For the larger surface roughness length, the near-steady state wind speed is weaker though the impact of soil moisture is far less clear. Concerning precipitation, the simulations with the larger roughness length produces more precipitation than the TC over water or the simulations with a smaller roughness length, except for the simulations with a soil moisture gradient. The enhanced precipitation was found to be caused by the enhanced latent heat flux. The soil moisture gradients increased the latent heat flux by promoting the surface-air moisture deficit through advection. The larger roughness length increased the latent heat flux by increasing the enthalpy exchange coefficient, which is an important component to the second manuscript.

The second manuscript revisits the idealized simulations and experiments with the focus more on the TC structure and the application of intensity theories. The main intensity hypothesis, the wind-induced surface heat exchange (WISHE), is examined in all of the experiments. Though slantwise-neutral convection is not attained, the reader is reminded that WISHE represents the strongest possible TC, which may not be the idealized environment. The vertical structure was found to be heavily influenced by the surface with the outflow at a lower height in the simulations with a larger surface roughness at a later time. Paradoxically, the simulations with a larger surface roughness (despite the weaker intensity) and the CTRL simulation can be categorized as a TC according to the cyclone phase space diagrams, while the simulations with less surface roughness *appear* to have started warm-core seclusion. This may be the result of condensational warming sustaining the lower warm core. The maximum potential intensity (MPI) was evaluated and found that a significant change – replacing the saturated entropy with the surface-modified saturated entropy – was required to imitate the BOE. Not including the surface modification yields a larger entropy difference and the implication that drier surfaces yield more intense TCs. The competing hypothesis, which focuses on convective asymmetries in the inner eyewall (Vortical Hot Towers or VHTs) and the associated wave response (Vortex Rossby Waves or VRWs), shows potential as it describes the spatiotemporal aspects of the maximum wind speed as well as the waveform rainband. Moreover, the spectra of the potential vorticity in the simulations with the lower roughness length and higher soil moisture show a unique feature for the BOE in higher soil moisture and lower surface roughness.

Manuscript three departs from the idealized simulations to investigate previous instances of Tropical Cyclone Maintenance and Intensification (TCMI) through the use of the International Best Track Archive for Climate Stewardship (IBTrACS) dataset. The data is categorized into TCMI and non-TCMI categories where both satisfy geographical requirements and are categorized as tropical storms or disturbances. TCMI events are events in which the wind speed increases or stays constant while non-TCMI events are TCs that weaken. The MERRA-2 reanalysis dataset is referenced to create a prototypical machine-learning model trained on the non-North Atlantic basin, while tested on the North Atlantic basin. Both the training and testing dataset were used to identify relevant variables for the development of the machine-learning model. A physical interpretation of the machine-learning model shows a large component from the BOE through the surface buoyancy scale. After the development of the machine-learning model, previously unstudied TCMI cyclones that are potential BOE case studies were identified and briefly studied.

In synthesis, it has been shown that modeling the BOE is possible but is highly dependent on the accuracy of the land-surface state as shown in Chapters 2 and 3. Not only is the accuracy of the land-surface state beneath a TC important, but the land-surface state outside of the track was shown to have just as significant of an impact. Improving the prediction of TCMI events require the accurate representation of the variables elucidated in the statistical model of Chapter 4. This includes not just the fluctuating variables that are of importance to land-atmosphere interactions but also the more static variables such as roughness length which has a non-negligible influence on TC evolution.

References

Acker, J. G., and G. Leptoukh, 2007: Online analysis enhances use of NASA Earth Science Data. *Eos (Washington. DC).*, **88**, doi:10.1029/2007EO020003.

Andersen, T. K., and J. M. Shepherd, 2014: A global spatiotemporal analysis of inland tropical cyclone maintenance or intensification. *Int. J. Climatol.*, doi:10.1002/joc.3693.

——, D. E. Radcliffe, and J. M. Shepherd, 2013: Quantifying surface energy fluxes in the vicinity of inland-tracking tropical cyclones. *J. Appl. Meteorol. Climatol.*, **52**, 2797–2808, doi:10.1175/JAMC-D-13-035.1.

Ankur, K., N. K. R. Busireddy, K. K. Osuri, and D. Niyogi, 2020: On the relationship between intensity changes and rainfall distribution in tropical cyclones over the North Indian Ocean. *Int. J. Climatol.*, **40**, 2015–2025, doi:10.1002/joc.6315.

Arndt, D. S., J. B. Basara, R. A. McPherson, B. G. Illston, G. D. McManus, and D. B. Demko, 2009: Observations of the Overland Reintensification of Tropical Storm Erin (2007). *Bull. Am. Meteorol. Soc.*, **90**, 1079–1094, doi:10.1175/2009BAMS2644.1. http://journals.ametsoc.org/doi/10.1175/2009BAMS2644.1.

Avila, L. A., 2010: *Tropical Cyclone Report Tropical Storm Hermine (AL102010)*. https://www.nhc.noaa.gov/data/tcr/AL102010_Hermine.pdf.

Berrick, S. W., G. Leptoukh, J. D. Farley, and H. Rui, 2009: Giovanni: A web service workflow-based data visualization and analysis System. *IEEE Trans. Geosci. Remote Sens.*, **47**, 106–113, doi:10.1109/TGRS.2008.2003183.

Bister, M., and K. A. Emanuel, 1998: Dissipative heating and hurricane intensity. *Meteorol. Atmos. Phys.*, **65**, 233–240, doi:10.1007/BF01030791.

Blake, E. S., T. B. Kimberlain, R. J. Berg, Cangia, J. P. Losi, and J. L. Beven II, 2013: Tropical cyclone report Hurricane Sandy (AL182012) 22 – 29 October 2012. *Natl. Weather Serv. Natl. Hurric. Cent.*, 1–157.

Bosart, L. F., J. M. Cordeira, T. J. Galarneau, B. J. Moore, and H. M. Archambault, 2012: An analysis of multiple predecessor rain events ahead of tropical cyclones Ike and Lowell: 10-15 September 2008. *Mon. Weather Rev.*, **140**, 1081–1107, doi:10.1175/MWR-D-11-00163.1.

Bosma, C. D., D. B. Wright, P. Nguyen, J. P. Kossin, D. C. Herndon, and J. M. Shepherd, 2020: An intuitive metric to quantify and communicate tropical cyclone rainfall hazard. *Bull. Am. Meteorol. Soc.*, **101**, E206–E220, doi:10.1175/BAMS-D-19-0075.1.

Brauer, N. S., J. B. Basara, P. E. Kirstetter, R. A. Wakefield, C. R. Homeyer, J. Yoo, M. Shepherd, and J. A. Santanello, 2021: The Inland Maintenance and Re-intensification of Tropical Storm Bill (2015) Part 2: Precipitation Microphysics. *J. Hydrometeorol.*, 1–52, doi:10.1175/jhm-d-20-0151.1.

Brier, G. W., 1950: VERIFICATION OF FORECASTS EXPRESSED IN TERMS OF PROBABILITY. *Mon. Weather Rev.*, **78**, 1–3, doi:10.1175/1520-0493(1950)078<0001:VOFEIT>2.0.CO;2. http://journals.ametsoc.org/doi/10.1175/1520-0493(1950)078%3C0001:VOFEIT%3E2.0.CO;2.

Bryan, G. H., 2013: Notes and correspondence comments on "sensitivity of tropical-cyclone models to the surface drag coefficient." *Q. J. R. Meteorol. Soc.*, **139**, 1957–1960, doi:10.1002/qj.2066.

Casteel, M. J., M. D. Sobsey, and J. P. Mueller, 2006: Fecal contamination of agrioultural soils before and after hurricane-associated flooding in North Carolina. *J. Environ. Sci. Heal. - Part A Toxic/Hazardous Subst. Environ. Eng.*, **41**, 173–184, doi:10.1080/10934520500351884.

Chan, J. C. L., and J. D. Kepert, 2010: Global perspectives on tropical cyclones: from science to mitigation.

Charney, J. G., and A. Eliassen, 1964: On the Growth of the Hurricane Depression. *J. Atmos. Sci.*, **21**, 68–75, doi:10.1175/1520-0469(1964)021<0068:OTGOTH>2.0.CO;2. http://journals.ametsoc.org/doi/abs/10.1175/1520-0469(1964)021%3C0068:OTGOTH%3E2.0.CO;2.

Chen, F., and Y. Zhang, 2009: On the coupling strength between the land surface and the atmosphere: From viewpoint of surface exchange coefficients. *Geophys. Res. Lett.*, **36**, 1–5, doi:10.1029/2009GL037980.

Chen, S.-H., and W.-Y. Sun, 2002: A One-dimensional Time Dependent Cloud Model. *J. Meteorol. Soc. Japan. Ser. II*, **80**, 99–118, doi:10.2151/jmsj.80.99. https://www.jstage.jst.go.jp/article/jmsj/80/1/80_1_99/_article.

Cheng, C. J., and C. C. Wu, 2018: The role of WISHE in secondary eyewall formation. *J. Atmos. Sci.*, **75**, 3823–3841, doi:10.1175/JAS-D-17-0236.1.

Chisolm, E. I., and J. C. Matthews, 2012: Impact of hurricanes and flooding on buried infrastructure. *Leadersh. Manag. Eng.*, **12**, 151–156, doi:10.1061/(ASCE)LM.1943-5630.0000182.

Clayton, H. H., 1927: A METHOD OF VERIFYING WEATHER FORECASTS. *Bull. Am. Meteorol. Soc.*, **8**, 144–146, doi:10.1175/1520-0477-8.10.144. https://journals.ametsoc.org/doi/10.1175/1520-0477-8.10.144.

——, 1934: RATING WEATHER FORECASTS. *Bull. Am. Meteorol. Soc.*, **15**, 279–283, doi:10.1175/1520-0477-15.12.279. https://journals.ametsoc.org/doi/10.1175/1520-0477-

15.12.279.

Coch, N. K., 2020: Inland Damage from Hurricanes. *J. Coast. Res.*, **36**, 1093–1105, doi:10.2112/JCOASTRES-D-20A-00002.1.

Collins, J. M., and K. Walsh, 2017: Hurricanes and Climate Change. *Hurricanes and Climate Change*, Vol. 3 of, 117–134.

Craig, G. C., and S. L. Gray, 1996: CISK or WISHE as the Mechanism for Tropical Cyclone Intensification. *J. Atmos. Sci.*, **53**, 3528–3540, doi:10.1175/1520-0469(1996)053<3528:COWATM>2.0.CO;2. http://journals.ametsoc.org/doi/abs/10.1175/1520-0469%281996%29053%3C3528%3ACOWATM%3E2.0.CO%3B2.

Cronin, T. W., and D. R. Chavas, 2019: Dry and Semidry Tropical Cyclones. *J. Atmos. Sci.*, **76**, 2193–2212, doi:10.1175/jas-d-18-0357.1.

Czajkowski, J., K. Simmons, and D. Sutter, 2011: An analysis of coastal and inland fatalities in landfalling US hurricanes. *Nat. Hazards*, **59**, 1513–1531, doi:10.1007/s11069-011-9849-x.

——, G. Villarini, M. Montgomery, E. Michel-Kerjan, and R. Goska, 2017: Assessing Current and Future Freshwater Flood Risk from North Atlantic Tropical Cyclones via Insurance Claims. *Sci. Rep.*, **7**, 1–10, doi:10.1038/srep41609. http://dx.doi.org/10.1038/srep41609.

Demaria, M., and J. Kaplan, 1994: Sea Surface Temperature and the Maximum Intensity of Atlantic Tropical Cyclones. *J. Clim.*, **7**, 1324–1334, doi:10.1175/1520-0442(1994)007<1324:SSTATM>2.0.CO;2. 10.1175/1520-0442(1994)007%3C1324:SSTATM%3E2.0.CO;2.

Donelan, M. A., B. K. Haus, N. Reul, W. J. Plant, M. Stiassnie, H. C. Graber, O. B. Brown, and E. S. Saltzman, 2004: On the limiting aerodynamic roughness of the ocean in very strong winds. *Geophys. Res. Lett.*, **31**, 1–5, doi:10.1029/2004GL019460.

Doswell, C. A., R. Davies-Jones, and D. L. Keller, 1990: On Summary Measures of Skill in Rare Event Forecasting Based on Contingency Tables. *Weather Forecast.*, **5**, 576–585, doi:10.1175/1520-0434(1990)005<0576:OSMOSI>2.0.CO;2. http://journals.ametsoc.org/doi/10.1175/1520-0434(1990)005%3C0576:OSMOSI%3E2.0.CO;2.

Elsner, J. B., J. P. Kossin, and T. H. Jagger, 2008: The increasing intensity of the strongest tropical cyclones. *Nature*, **455**, 92–95, doi:10.1038/nature07234.

Emanuel, K., 2012: Self-Stratification of Tropical Cyclone Outflow. Part II: Implications for Storm Intensification. *J. Atmos. Sci.*, **69**, 988–996, doi:10.1175/JAS-D-11-0177.1. http://journals.ametsoc.org/doi/abs/10.1175/JAS-D-11-0177.1.

——, J. Callaghan, and P. Otto, 2008: A Hypothesis for the Redevelopment of Warm-Core Cyclones over Northern Australia*. *Mon. Weather Rev.*, doi:10.1175/2008MWR2409.1.

Emanuel, K. A., 1986: An Air-Sea Interaction Theory for Tropical Cyclones. Part I: Steady-State Maintenance. *J. Atmos. Sci.*, doi:10.1175/1520-0469(1986)043<0585:AASITF>2.0.CO;2.

——, 1987: The dependence of hurricane intensity on climate. *Nature*, **326**, 483–485, doi:10.1038/326483a0.

Emanuel, K. A., 1994: *Atmospheric convection / Kerry A. Emanuel.* New York : Oxford University Press, New York,.

Emanuel, K. A., 1995: Sensitivity of Tropical Cyclones to Surface Exchange Coefficients and a Revised Steady-State Model incorporating Eye Dynamics. *J. Atmos. Sci.*, **52**, 3969–3976, doi:10.1175/1520-0469(1995)052<3969:SOTCTS>2.0.CO;2. http://journals.ametsoc.org/doi/abs/10.1175/1520-

0469%281995%29052%3C3969%3ASOTCTS%3E2.0.CO%3B2.

Erickson, T. B., J. Brooks, E. J. Nilles, P. N. Pham, and P. Vinck, 2019: Environmental health effects attributed to toxic and infectious agents following hurricanes, cyclones, flash floods and major hydrometeorological events. *J. Toxicol. Environ. Heal. - Part B Crit. Rev.*, **22**, 157–171, doi:10.1080/10937404.2019.1654422. https://doi.org/10.1080/10937404.2019.1654422.

Evans, C., R. S. Schumacher, and T. J. Galarneau, 2011: Sensitivity in the Overland Reintensification of Tropical Cyclone Erin (2007) to Near-Surface Soil Moisture Characteristics. *Mon. Weather Rev.*, doi:10.1175/2011MWR3593.1.

——, and Coauthors, 2017: The extratropical transition of tropical cyclones. Part I: Cyclone evolution and direct impacts. *Mon. Weather Rev.*, **145**, 4317–4344, doi:10.1175/MWR-D-17-0027.1.

Feldmann, M., K. Emanuel, L. Zhu, and U. Lohmann, 2019: Estimation of atlantic tropical cyclone rainfall frequency in the United States. *J. Appl. Meteorol. Climatol.*, **58**, 1853–1866, doi:10.1175/JAMC-D-19-0011.1.

Frank, W. M., and E. A. Ritchie, 2001: Effects of Vertical Wind Shear on the Intensity and Structure of Numerically Simulated Hurricanes. *Mon. Weather Rev.*, **129**, 2249–2269, doi:10.1175/1520-0493(2001)129<2249:EOVWSO>2.0.CO;2. http://journals.ametsoc.org/doi/abs/10.1175/1520-0493%282001%29129%3C2249%3AEOVWSO%3E2.0.CO%3B2.

Franklin, J. L., L. A. Avila, J. L. Beven, M. B. Lawrence, R. J. Pasch, and S. R. Stewart, 2001: Atlantic hurricane season of 2000. *Mon. Weather Rev.*, **129**, 3037–3056, doi:10.1175/1520-0493(2001)129<3037:AHSO>2.0.CO;2.

Franklin, J. L., R. J. Pasch, L. A. Avila, J. L. Beven, M. B. Lawrence, S. R. Stewart, and E. S. Blake, 2006: Atlantic hurricane season of 2004. *Mon. Weather Rev.*, **134**, 981–1025, doi:10.1175/MWR3096.1.

Fuchs, Ž., and D. J. Raymond, 2017: A simple model of intraseasonal oscillations. *J. Adv. Model. Earth Syst.*, **9**, 1195–1211, doi:10.1002/2017MS000963. https://onlinelibrary.wiley.com/doi/abs/10.1002/2017MS000963.

Fussell, E., and S. R. Lowe, 2014: The impact of housing displacement on the mental health of low-income parents after Hurricane Katrina. *Soc. Sci. Med.*, **113**, 137–144, doi:10.1016/j.socscimed.2014.05.025. http://dx.doi.org/10.1016/j.socscimed.2014.05.025.

Galarneau, T. J., 2015: Influence of a predecessor rain event on the track of tropical cyclone Isaac (2012). *Mon. Weather Rev.*, **143**, 3354–3376, doi:10.1175/MWR-D-15-0053.1.

Gelaro, R., and Coauthors, 2017: The modern-era retrospective analysis for research and applications, version 2 (MERRA-2). *J. Clim.*, **30**, 5419–5454, doi:10.1175/JCLI-D-16-0758.1.

Gentry, M. S., and G. M. Lackmann, 2010: Sensitivity of Simulated Tropical Cyclone Structure and Intensity to Horizontal Resolution. *Mon. Weather Rev.*, **138**, 688–704, doi:10.1175/2009MWR2976.1. http://journals.ametsoc.org/doi/abs/10.1175/2009MWR2976.1.

Gilbert, G. K., 1884: FINLEY’S TORNADO PREDICTIONS. *Am. Meteorol. Journal. A Mon. Rev. Meteorol. Allied Branches Study*, **1**, 166. https://search.proquest.com/scholarly-journals/finleys-tornado-predictions/docview/124374084/se-2?accountid=14537.

Grams, C. M., and S. R. Blumer, 2015: European high-impact weather caused by the downstream response to the extratropical transition of North Atlantic Hurricane Katia

(2011). *Geophys. Res. Lett.*, **42**, 8738–8748, doi:10.1002/2015GL066253.

Gray, W. M., and Coauthors, 1986: WMO TROPICAL METEOROLOGY PROGRAMME (TMP). Vol. 83 of, 1427–1430.

Han, S. R., S. D. Guikema, S. M. Quiring, K. H. Lee, D. Rosowsky, and R. A. Davidson, 2009: Estimating the spatial distribution of power outages during hurricanes in the Gulf coast region. *Reliab. Eng. Syst. Saf.*, **94**, 199–210, doi:10.1016/j.ress.2008.02.018.

Hart, R. E., 2003: A cyclone phase space derived from thermal wind and thermal asymmetry. *Mon. Weather Rev.*, **131**, 585–616, doi:10.1175/1520-0493(2003)131<0585:ACPSDF>2.0.CO;2.

Hasler, N., D. Werth, and R. Avissar, 2009: Effects of tropical deforestation on global hydroclimate: A multimodel ensemble analysis. *J. Clim.*, **22**, 1124–1141, doi:10.1175/2008JCLI2157.1.

Heidke, P., 1926: Berechnung des Erfolges und der Güte der Windstärkevorhersagen im Sturmwarnungsdienst. *Geogr. Ann.*, **8**, 301, doi:10.2307/519729. https://www.jstor.org/stable/519729?origin=crossref.

Henderson-Sellers, A., and Coauthors, 1998: Tropical Cyclones and Global Climate Change: A Post-IPCC Assessment. *Bull. Am. Meteorol. Soc.*, **79**, 19–38, doi:10.1175/1520-0477(1998)079<0019:TCAGCC>2.0.CO;2.

Hendricks, E. A., M. T. Montgomery, and C. A. Davis, 2004: The Role of “Vortical” Hot Towers in the Formation of Tropical Cyclone Diana (1984). *J. Atmos. Sci.*, **61**, 1209–1232, doi:10.1175/1520-0469(2004)061<1209:TROVHT>2.0.CO;2. http://journals.ametsoc.org/doi/abs/10.1175/1520-0469%282004%29061%3C1209%3ATROVHT%3E2.0.CO%3B2.

Hiesl, P., and S. L. Rodriguez, 2019: Quantifying the impact of a flood and hurricane event on tree farms in South Carolina: A survey. *Forests*, **10**, doi:10.3390/f10070546.

Hill, K. A., and G. M. Lackmann, 2008: Analysis of idealized tropical cyclone simulations using the Weather Research and Forecasting Model: Sensitivity to turbulence parameterization and grid spacing. *Mon. Weather Rev.*, **preprint**, 1, doi:10.1175/2008mwr2220.

Holland, G. J., 1997: The Maximum Potential Intensity of Tropical Cyclones. *J. Atmos. Sci.*, **54**, 2519–2541, doi:10.1175/1520-0469(1997)054<2519:TMPIOT>2.0.CO;2. http://journals.ametsoc.org/doi/abs/10.1175/1520-0469%281997%29054%3C2519%3ATMPIOT%3E2.0.CO%3B2.

Hong, S.-Y., Y. Noh, and J. Dudhia, 2006: A New Vertical Diffusion Package with an Explicit Treatment of Entrainment Processes. *Mon. Weather Rev.*, **134**, 2318–2341, doi:10.1175/MWR3199.1. http://journals.ametsoc.org/doi/abs/10.1175/MWR3199.1.

Hong, X., M. J. Leach, and S. Raman, 1995: Role of vegetation in generation of mesoscale circulation. *Atmos. Environ.*, **29**, 2163–2176, doi:10.1016/1352-2310(94)00241-C.

Hunter, L. M., 2005: Migration and environmental hazards. *Popul. Environ.*, **26**, 273–302, doi:10.1007/s11111-005-3343-x.

Jiménez, P. A., J. Dudhia, J. F. González-Rouco, J. Navarro, J. P. Montávez, and E. García-Bustamante, 2012: A Revised Scheme for the WRF Surface Layer Formulation. *Mon. Weather Rev.*, **140**, 898–918, doi:10.1175/MWR-D-11-00056.1. http://journals.ametsoc.org/doi/abs/10.1175/MWR-D-11-00056.1.

Jones, S. C., and Coauthors, 2003: The Extratropical Transition of Tropical Cyclones: Forecast Challenges, Current Understanding, and Future Directions. *Weather Forecast.*, **18**, 1052–1092, doi:10.1175/1520-0434(2003)018<1052:tetotc>2.0.co;2.

Jordan, C. L., 1958: Mean Soundings for the West Indies Area. *J. Meteorol.*, **15**, 91–97, doi:10.1175/1520-0469(1958)015<0091:MSFTWI>2.0.CO;2. http://journals.ametsoc.org/doi/abs/10.1175/1520-0469%281958%29015%3C0091%3AMSFTWI%3E2.0.CO%3B2.

Jordan, M. R., and C. A. Clayson, 2008: Evaluating the usefulness of a new set of hurricane classification indices. *Mon. Weather Rev.*, **136**, 5234–5238, doi:10.1175/2008MWR2449.1.

Kaplan, J., and M. DeMaria, 1995: A Simple Empirical Model for Predicting the Decay of Tropical Cyclone Winds after Landfall. *J. Appl. Meteorol.*, **34**, 2499–2512, doi:10.1175/1520-0450(1995)034<2499:ASEMFP>2.0.CO;2. https://journals.ametsoc.org/doi/pdf/10.1175/1520-0450%281995%29034%3C2499%3AASEMFP%3E2.0.CO%3B2.

Kaplan, J., and M. Demaria, 2001: On the decay of tropical cyclone winds after landfall in the New England Area. *J. Appl. Meteorol.*, **40**, 280–286, doi:10.1175/1520-0450(2001)040<0280:OTDOTC>2.0.CO;2.

Kehoe, J., S. Raman, and R. Boyles, 2010: Characteristics of landfalling tropical cyclones in North Carolina. *Mar. Geod.*, **33**, 394–411, doi:10.1080/01490419.2010.518059.

Keller, J. H., and Coauthors, 2018: The Extratropical Transition of Tropical Cyclones. Part II: Interaction with the Midlatitude Flow, Downstream Impacts, and Implications for Predictability. *Mon. Weather Rev.*, **147**, 1077–1106, doi:10.1175/mwr-d-17-0329.1.

Kellner, O., D. Niyogi, M. Lei, and A. Kumar, 2012: The role of anomalous soil moisture on the inland reintensification of Tropical Storm Erin (2007). *Nat. Hazards*, **63**, 1573–1600, doi:10.1007/s11069-011-9966-6.

Kessler, E., 1969: On the distribution and continuity of water substance in atmospheric circulations. *Meteorol. Monogr.*, **10**, 88 pp., doi:http://dx.doi.org/10.1016/0169-8095(94)00090-Z.

Kidder, S. Q., and Coauthors, 2005: The Tropical Rainfall Potential (TRaP) Technique. Part I: Description and Examples. *Weather Forecast.*, **20**, 456–464, doi:10.1175/WAF860.1. http://journals.ametsoc.org/doi/abs/10.1175/WAF860.1.

Kieu, C., 2015: Hurricane maximum potential intensity equilibrium. *Q. J. R. Meteorol. Soc.*, **141**, 2471–2480, doi:10.1002/qj.2556.

Kieu, C. Q., and Z. Moon, 2016: Hurricane intensity predictability. *Bull. Am. Meteorol. Soc.*, **97**, 1847–1857, doi:10.1175/BAMS-D-15-00168.1.

Kimball, S. K., 2006: A modeling study of hurricane landfall in a dry environment. *Mon. Weather Rev.*, **134**, 1901–1918, doi:10.1175/MWR3155.1.

Klein, P. M., P. A. Harr, and R. L. Elsberry, 2000: Extratropical transition of western North Pacific tropical cyclones: An overview and conceptual model of the transformation stage. *Weather Forecast.*, **15**, 373–395, doi:10.1175/1520-0434(2000)015<0373:ETOWNP>2.0.CO;2.

Knapp, K. R., M. C. Kruk, D. H. Levinson, H. J. Diamond, and C. J. Neumann, 2010: The international best track archive for climate stewardship (IBTrACS). *Bull. Am. Meteorol. Soc.*, **91**, 363–376, doi:10.1175/2009BAMS2755.1.

——, ——, ——, ——, and ——, 2018: International Best Track Archive for Climate Stewardship (IBTrACS) Project, Version 4. doi:https://doi.org/10.25921/82ty-9e16. Accessed 02 January 2021.

Ladwig, W., 2019: *wrf-python (version 1.3. 1)[Software]*. Tech. rep., UCAR, NCAR, Boulder, Colorado, USA, available at: https://github …,.

Larson, J., Y. Zhou, and R. W. Higgins, 2005: Characteristics of landfalling tropical cyclones in the United States and Mexico: Climatology and interannual variability. *J. Clim.*, **18**, 1247–1262, doi:10.1175/JCLI3317.1.

Lee, T. J., and R. A. Pielke, 1992: Estimating the soil surface specific humidity. *J. Appl. Meteorol.*, **31**, 480–484, doi:10.1175/1520-0450(1992)031<0480:ETSSSH>2.0.CO;2.

Li, R. C. Y., and W. Zhou, 2015: Interdecadal changes in summertime tropical cyclone precipitation over Southeast China during 1960-2009. *J. Clim.*, **28**, 1494–1509, doi:10.1175/JCLI-D-14-00246.1.

Li, X., G. Zhao, J. Nielsen-Gammon, J. Salazar, M. Wigmosta, N. Sun, D. Judi, and H. Gao, 2020: Impacts of urbanization, antecedent rainfall event, and cyclone tracks on extreme floods at Houston reservoirs during Hurricane Harvey. *Environ. Res. Lett.*, **15**, doi:10.1088/1748-9326/abc4ff.

Li, Y., K. K. W. Cheung, and J. C. L. Chan, 2015: Modelling the effects of land-sea contrast on tropical cyclone precipitation under environmental vertical wind shear. *Q. J. R. Meteorol. Soc.*, **141**, 396–412, doi:10.1002/qj.2359.

Lin, C.-Y., and E. J. Cha, 2021: Hurricane Freshwater Flood Risk Assessment Model for Residential Buildings in Southeast US Coastal States Considering Climate Change. *Nat. Hazards Rev.*, **22**, 04020061, doi:10.1061/(asce)nh.1527-6996.0000442.

Liou, Y. C., T. C. C. Wang, and P. Y. Huang, 2016: The Inland eyewall reintensification of Typhoon Fanapi (2010) documented from an observational perspective using multiple-doppler radar and surface measurements. *Mon. Weather Rev.*, **144**, 241–261, doi:10.1175/MWR-D-15-0136.1.

Liu, L., J. Xu, Y. Wang, and Y. Duan, 2019: Contribution of Recycling of Surface Precipitation to Landfalling Tropical Cyclone Rainfall: A Modeling Study for Typhoon Utor (2013). *J. Geophys. Res. Atmos.*, **124**, 870–885, doi:10.1029/2018JD029380.

Lowe, M. P., 2012: SENSITIVITY ANALYSIS OF HURRICANE EVACUATION CASUALTIES AND COSTS IN FLORIDA. The Pennsylvania State University The, .

Lowe, S. R., J. E. Rhodes, L. Zwiebach, and C. S. Chan, 2009: The impact of pet loss on the perceived social support and psychological distress of hurricane survivors. *J. Trauma. Stress*, **22**, 244–247, doi:10.1002/jts.20403. http://doi.wiley.com/10.1002/jts.20403.

Lu, P., N. Lin, K. Emanuel, D. Chavas, and J. Smith, 2018: Assessing hurricane rainfall mechanisms using a physics-based model: Hurricanes Isabel (2003) and Irene (2011). *J. Atmos. Sci.*, **75**, 2337–2358, doi:10.1175/JAS-D-17-0264.1.

Malkus, J. S., and H. Riehl, 1960: On the Dynamics and Energy Transformations in Steady-State Hurricanes. *Tellus*, **12**, 1–20, doi:10.3402/tellusa.v12i1.9351. https://www.tandfonline.com/doi/full/10.3402/tellusa.v12i1.9351.

Manuel, J., 2013: The Long Road to Recovery: Environmental Health Impacts of Hurricane Sandy. *Environ. Health Perspect.*, **121**, 48–48, doi:10.1289/ehp.121-a152. https://ehp.niehs.nih.gov/doi/10.1289/ehp.121-a152.

Manzato, A., 2007: A note on the maximum Pierce skill score. *Weather Forecast.*, **22**, 1148–1154, doi:10.1175/WAF1041.1.

McKernan, J., and K. V. Mulcahy, 2008: Hurricane katrina: A cultural chernobyl. *J. Arts Manag. Law Soc.*, **38**, 217–232, doi:10.3200/JAML.38.3.217-232.

McWilliams, J. C., L. P. Graves, and M. T. Montgomery, 2003: A formal theory for vortex Rossby waves and vortex evolution. *Geophys. Astrophys. Fluid Dyn.*, **97**, 275–309, doi:10.1080/0309192031000108698.

Miller, C., M. Gibbons, K. Beatty, and A. Boissonnade, 2013: Topographic speed-up effects and observed roof damage on Bermuda following Hurricane Fabian (2003). *Weather Forecast.*, **28**, 159–174, doi:10.1175/WAF-D-12-00050.1.

Misuri, A., V. Casson Moreno, N. Quddus, and V. Cozzani, 2019: Lessons learnt from the impact of hurricane Harvey on the chemical and process industry. *Reliab. Eng. Syst. Saf.*, **190**, 106521, doi:10.1016/j.ress.2019.106521. https://doi.org/10.1016/j.ress.2019.106521.

Moller, J. D., and M. T. Montgomery, 2000: Tropical cyclone evolution via potential vorticity anomalies in a three-dimensional balance model. *J. Atmos. Sci.*, **57**, 3366–3387, doi:10.1175/1520-0469(2000)057<3366:TCEVPV>2.0.CO;2.

Monteverdi, J. P., and R. Edwards, 2010: The Redevelopment of a Warm-Core Structure in Erin: A Case of Inland Tropical Storm Formation. *E-Journal Sev. Storms Meteorol.*, **5**, 1–18. http://ejssm.org/ojs/index.php/ejssm/article/viewArticle/65.

Montgomery, M. T., and R. J. Kallenbach, 1997: A theory for vortex Rossby-waves and its application to spiral bands and intensity changes in hurricanes. *Q. J. R. Meteorol. Soc.*, **123**, 435–465, doi:10.1256/smsqj.53809.

Montgomery, M. T., and R. K. Smith, 2014: Paradigms for tropical cyclone intensification. *Aust. Meteorol. Oceanogr. J.*, **64**, 37–66, doi:10.1002/qj.

Montgomery, M. T., and R. K. Smith, 2020: Comments on "An Evaluation of Hurricane Superintensity in Axisymmetric Numerical Models." *J. Atmos. Sci.*, **77**, 1887–1892, doi:10.1175/JAS-D-19-0175.1. http://journals.ametsoc.org/doi/10.1175/JAS-D-19-0238.1.

Montgomery, M. T., M. E. Nicholls, T. a. Cram, and a. B. Saunders, 2006: A Vortical Hot Tower Route to Tropical Cyclogenesis. *J. Atmos. Sci.*, **63**, 355–386, doi:10.1175/JAS3604.1.

Montgomery, M. T., N. van Sang, R. K. Smith, and J. Persing, 2009: Do tropical cyclones intensify by WISHE? *Q. J. R. Meteorol. Soc.*, **135**, 1697–1714, doi:10.1002/qj.459.

Mrowiec, A. A., S. T. Garner, and O. M. Pauluis, 2011: Axisymmetric Hurricane in a Dry Atmosphere: Theoretical Framework and Numerical Experiments. *J. Atmos. Sci.*, doi:10.1175/2011JAS3639.1.

Nair, U. S., and Coauthors, 2019: Influence of Land Cover and Soil Moisture based Brown Ocean Effect on an Extreme Rainfall Event from a Louisiana Gulf Coast Tropical System. *Sci. Rep.*, **9**, 17136, doi:10.1038/s41598-019-53031-6. http://www.nature.com/articles/s41598-019-53031-6.

National Weather Service (NWS), 2018a: *Storm Data*. https://www.nws.noaa.gov/directives/sym/pd01016005curr.pdf.

——, 2018b: *Storm Data*. https://www.nws.noaa.gov/directives/sym/pd01016005curr.pdf.

Needham, H. F., B. D. Keim, and D. Sathiaraj, 2015: A review of tropical cyclone-generated storm surges: Global data sources, observations, and impacts. *Rev. Geophys.*, **53**, 545–591, doi:10.1002/2014RG000477.

O'Brien, R. M., 2007: A caution regarding rules of thumb for variance inflation factors. *Qual. Quant.*, **41**, 673–690, doi:10.1007/s11135-006-9018-6.

Ookouchi, Y., M. Segal, R. C. Kessler, and R. A. Pielke, 1984: Evaluation of soil moisture effects on the generation and modification of mesoscale circulations. *Mon. Weather Rev.*, **112**, 2281–2292, doi:10.1175/1520-0493(1984)112<2281:EOSMEO>2.0.CO;2.

Peirce, C. S., 1884: The numerical measure of the success of predictions. *Science (80-.).*, **ns-4**, 453–454, doi:10.1126/science.ns-4.93.453-a. https://www.sciencemag.org/lookup/doi/10.1126/science.ns-4.93.453-a.

Persing, J., and M. T. Montgomery, 2003: Hurricane superintensity. *J. Atmos. Sci.*, **60**, 2349–2371, doi:10.1175/1520-0469(2003)060<2349:HS>2.0.CO;2.

Powell, M. D., P. J. Vickery, and T. A. Reinhold, 2003: Reduced drag coefficient for high wind speeds in tropical cyclones. *Nature*, **422**, 279–283, doi:10.1038/nature01481. http://www.nature.com/articles/nature01481.

Quintanar, A. I., R. Mahmood, A. Suarez, and R. Leeper, 2016: Atmospheric sensitivity to roughness length in a regional atmospheric model over the Ohio–Tennessee River Valley. *Meteorol. Atmos. Phys.*, **128**, 315–330, doi:10.1007/s00703-015-0415-z.

Rao, N. N., V. B. Rao, S. S. V. S. Ramakrishna, and B. R. S. Rao, 2019: Moisture Budget of the Tropical Cyclones Formed over the Bay of Bengal: Role of Soil Moisture After Landfall. *Pure Appl. Geophys.*, **176**, 441–461, doi:10.1007/s00024-018-1964-0.

Rappaport, E. N., 2000: Loss of life in the United States associated with recent atlantic tropical cyclones. *Bull. Am. Meteorol. Soc.*, **81**, 2065–2073, doi:10.1175/1520-0477(2000)081<2065:LOLITU>2.3.CO;2.

Ren, F., G. Wu, W. Dong, X. Wang, Y. Wang, W. Ai, and W. Li, 2006: Changes in tropical cyclone precipitation over China. *Geophys. Res. Lett.*, **33**, 2–5, doi:10.1029/2006GL027951.

da Rocha, H. R., C. A. Nobre, J. P. Bonatti, I. R. Wright, and P. J. Sellers, 1996: A vegetation-atmosphere interaction study for Amazonia deforestation using field data and a ‘single column’ model. *Q. J. R. Meteorol. Soc.*, **122**, 567–594, doi:10.1002/qj.49712253102. http://doi.wiley.com/10.1256/qj.03.130.

Rogers, R. F., P. D. Reasor, J. A. Zawislak, and L. T. Nguyen, 2020: Precipitation processes and vortex alignment during the intensification of a weak tropical cyclone in moderate vertical shear. *Mon. Weather Rev.*, **148**, 1899–1929, doi:10.1175/MWR-D-19-0315.1.

Rotunno, R., and K. Emanuel, 1987: An Air-Sea Interaction Theory for Tropical Cyclones. Part2: Evolutionary Study Using a Nonhydrostatic Axisymmetric Numerical Model. *J. Atmos. Sci.*, **44**, 542–561.

Rousseau-Rizzi, R., and K. Emanuel, 2019: An evaluation of hurricane superintensity in axisymmetric numerical models. *J. Atmos. Sci.*, **76**, 1697–1708, doi:10.1175/JAS-D-18-0238.1.

——, and ——, 2020: Reply to "Comments on 'An Evaluation of Hurricane Superintensity in Axisymmetric Numerical Models.'" *J. Atmos. Sci.*, **77**, 1893–1896, doi:10.1175/JAS-D-19-0248.1. http://journals.ametsoc.org/doi/10.1175/JAS-D-19-0248.1.

Ryan, B. J., R. C. Franklin, F. M. Burkle, K. Watt, P. Aitken, E. C. Smith, and P. Leggat, 2015: Analyzing the Impact of Severe Tropical Cyclone Yasi on Public Health Infrastructure and the Management of Noncommunicable Diseases. *Prehosp. Disaster Med.*, **30**, 28–37, doi:10.1017/S1049023X1400137X.

Seabold, S., and J. Perktold, 2010: Statsmodels: Econometric and Statistical Modeling with Python. *Proc. 9th Python Sci. Conf.*, 92–96, doi:10.25080/majora-92bf1922-011.

Sen, O. L., Y. Wang, and B. Wang, 2004: Impact of Indochina deforestation on the east Asian summer monsoon. *J. Clim.*, **17**, 1366–1380, doi:10.1175/1520-0442(2004)017<1366:IOIDOT>2.0.CO;2.

Shen, W., I. Ginis, and R. Tuleya, 2002: A numerical investigation of land surface water on landfalling hurricanes. *J. Atmos. …*, **59**, 789–802, doi:10.1175/1520-0469(2002)059<0789:ANIOLS>2.0.CO;2. http://journals.ametsoc.org/doi/full/10.1175/1520-0469(2002)059%3C0789:ANIOLS%3E2.0.CO;2.

Shepherd, J. M., 2005: A review of current investigations of urban-induced rainfall and recommendations for the future. *Earth Interact.*, **9**, doi:10.1175/EI156.1.

——, A. Grundstein, and T. L. Mote, 2007: Quantifying the contribution of tropical cyclones to extreme rainfall along the coastal southeastern United States. *Geophys. Res. Lett.*, **34**, 1–5, doi:10.1029/2007GL031694.

Shepherd, M., A. Thomas, J. Santanello, P. M. Lawston, and J. Basara, 2021: Evidence of warm core structure maintenance over land: A case study analysis of cyclone Kelvin. *Environ. Res. Commun.*, doi:10.1088/2515-7620/abf39a. https://iopscience.iop.org/article/10.1088/2515-7620/abf39a.

Shimada, U., H. Owada, M. Yamaguchi, T. Iriguchi, M. Sawada, A. K. Aonashi, M. Demaria, and K. D. Musgrave, 2018: Further improvements to the statistical hurricane intensity prediction scheme using tropical cyclone rainfall and structural features. *Weather Forecast.*, **33**, 1587–1603, doi:10.1175/WAF-D-18-0021.1.

Smith, R. K., and M. T. Montgomery, 2015: Toward Clarity on Understanding Tropical Cyclone Intensification. *J. Atmos. Sci.*, **72**, 3020–3031, doi:10.1175/JAS-D-15-0017.1. http://journals.ametsoc.org/doi/10.1175/JAS-D-15-0017.1.

——, ——, and S. Vogl, 2008: A critique of Emanuel's hurricane model and potential intensity theory. *Q. J. R. Meteorol. Soc.*, **134**, 551–561, doi:10.1002/qj.241. http://onlinelibrary.wiley.com/doi/10.1002/qj.71/abstract.

Stephenson, D. B., 2000: Use of the "odds ratio" for diagnosing forecast skill. *Weather Forecast.*, **15**, 221–232, doi:10.1175/1520-0434(2000)015<0221:UOTORF>2.0.CO;2.

Stewart, S. R., and R. Berg, 2019: National Hurricane Center tropical cyclone report: Hurricane Florence (AL062018). *Natl. Hurric. Cent.*, 1–98.

https://www.nhc.noaa.gov/data/tcr/AL152017_Maria.pdf.

Stull, R. B., 2009: *An introduction to boundary layer meteorology*. Springer Science & Business Media,.

Subramanian, S., 2016: Modeling the impact of land surface feedbacks on post landfall tropical cyclones.

Sud, Y. C., W. K.-M. Lau, G. K. Walker, J.-H. Kim, G. E. Liston, and P. J. Sellers, 1996: Biogeophysical Consequences of a Tropical Deforestation Scenario: A GCM Simulation Study. *J. Clim.*, **9**, 3225–3247, doi:10.1175/1520-0442(1996)009<3225:BCOATD>2.0.CO;2. http://journals.ametsoc.org/doi/10.1175/1520-0442(1996)009%3C3225:BCOATD%3E2.0.CO;2.

Tang, S., R. K. Smith, M. T. Montgomery, and M. Gu, 2016: Numerical study of the spin-up of a tropical low over land during the Australian monsoon. *Q. J. R. Meteorol. Soc.*, **142**, 2021–2032, doi:10.1002/qj.2797.

Tang, X., and F. Zhang, 2016: Impacts of the diurnal radiation cycle on the formation, intensity, and structure of Hurricane Edouard (2014). *J. Atmos. Sci.*, **73**, 2871–2892, doi:10.1175/JAS-D-15-0283.1.

——, Z. M. Tan, J. Fang, E. B. Munsell, and F. Zhang, 2019: Impact of the diurnal radiation contrast on the contraction of radius of maximum wind during intensification of Hurricane Edouard (2014). *J. Atmos. Sci.*, **76**, 421–432, doi:10.1175/JAS-D-18-0131.1.

Tao, D., K. Emanuel, F. Zhang, R. Rotunno, M. M. Bell, and R. G. Nystrom, 2019: Evaluation of the Assumptions in the Steady-State Tropical Cyclone Self-Stratified Outflow Using Three-Dimensional Convection-Allowing Simulations. *J. Atmos. Sci.*, **76**, 2995–3009, doi:10.1175/jas-d-19-0033.1.

Tewari, M., and Coauthors, 2004: Implementation and verification of the unified noah land surface model in the WRF model. *Bull. Am. Meteorol. Soc.*, 2165–2170, doi:10.1007/s11269-013-0452-7.

Tonkin, H., G. J. Holland, N. Holbrook, and A. Henderson-Sellers, 2000: An evaluation of thermodynamic estimates of climatological maximum potential tropical cyclone intensity. *Mon. Weather Rev.*, **128**, 746–762, doi:10.1175/1520-0493(2000)128<0746:AEOTEO>2.0.CO;2.

Touma, D., S. Stevenson, S. J. Camargo, D. E. Horton, and N. S. Diffenbaugh, 2019: Variations in the Intensity and Spatial Extent of Tropical Cyclone Precipitation. *Geophys. Res. Lett.*, **46**, 13992–14002, doi:10.1029/2019GL083452.

Tu, J. Y., J. M. Chen, L. Wu, and C. Z. Chi, 2020: Inter-decadal and inter-annual variability of meridional tropical cyclone activity during September–October in the northwestern North Pacific after 1998. *Int. J. Climatol.*, **40**, 1686–1702, doi:10.1002/joc.6295.

Tuleya, R. E., and Y. Kurihara, 1978: A Numerical Simulation of the Landfall of Tropical Cyclones. *J. Atmos. Sci.*, **35**, 242–257, doi:10.1175/1520-0469(1978)035<0242:ANSOTL>2.0.CO;2. http://journals.ametsoc.org/doi/abs/10.1175/1520-0469(1978)035%3C0242:ANSOTL%3E2.0.CO;2.

Wang, D., and Y. Lin, 2020: Size and Structure of Dry and Moist Reversible Tropical Cyclones. *J. Atmos. Sci.*, **77**, 2091–2114, doi:10.1175/jas-d-19-0229.1.

Weinkle, J., C. Landsea, D. Collins, R. Musulin, R. P. Crompton, P. J. Klotzbach, and R. Pielke, 2018: Normalized hurricane damage in the continental United States 1900–2017. *Nat. Sustain.*, **1**, 808–813, doi:10.1038/s41893-018-0165-2. https://doi.org/10.1038/s41893-018-

0165-2.

Wen, G., G. Huang, H. Huang, C. Liu, and X. Bi, 2019: Observed rainfall asymmetry of tropical cyclone in the process of making landfall in Guangdong, south China. *Int. J. Climatol.*, **39**, 3379–3395, doi:10.1002/joc.6027.

Wilks, D. S., 2006: *Statistical methods in the atmospheric sciences*. Academic press,.

Wingo, M. T., and D. J. Cecil, 2010: Effects of vertical wind shear on tropical cyclone precipitation. *Mon. Weather Rev.*, **138**, 645–662, doi:10.1175/2009MWR2921.1.

Wood, B. W., W. Goff, and M. Nesbitt, 2001: Pecans and hurricanes. *HortScience*, **36**, 253–258, doi:10.21273/hortsci.36.2.253.

Yoo, J., J. A. Santanello, M. Shepherd, S. Kumar, P. Lawston, and A. M. Thomas, 2020: Quantification of the land surface and brown ocean influence on tropical cyclone intensification over land. *J. Hydrometeorol.*, **21**, 1171–1192, doi:10.1175/JHM-D-19-0214.1.

Zhang, F., and K. Emanuel, 2016: On the Role of Surface Fluxes and WISHE in Tropical Cyclone Intensification. *J. Atmos. Sci.*, doi:10.1175/JAS-D-16-0011.1.

Zhang, W., G. Villarini, G. A. Vecchi, and J. A. Smith, 2018: Urbanization exacerbated the rainfall and flooding caused by hurricane Harvey in Houston. *Nature*, **563**, 384–388, doi:10.1038/s41586-018-0676-z. http://dx.doi.org/10.1038/s41586-018-0676-z.

Zhang, Y., J. A. Smith, L. Luo, Z. Wang, and M. L. Baeck, 2014: Urbanization and rainfall variability in the Beijing metropolitan region. *J. Hydrometeorol.*, **15**, 2219–2235, doi:10.1175/JHM-D-13-0180.1.

Zhu, L., and S. M. Quiring, 2013: Variations in tropical cyclone precipitation in Texas (1950 to 2009). *J. Geophys. Res. Atmos.*, **118**, 3085–3096, doi:10.1029/2012JD018554.

——, O. W. Frauenfeld, and S. M. Quiring, 2013: Seasonal tropical cyclone precipitation in Texas: A statistical modeling approach based on a 60 year climatology. *J. Geophys. Res. Atmos.*, **118**, 8842–8856, doi:10.1002/jgrd.50663.

Zhu, P., 2008: Impact of land-surface roughness on surface winds during hurricane landfall. *Q. J. R. Meteorol. Soc.*, **134**, 1051–1057, doi:10.1002/qj.265. http://doi.wiley.com/10.1002/qj.265.

Zhuge, X.-Y., J. Ming, and Y. Wang, 2015: Reassessing the Use of Inner-Core Hot Towers to Predict Tropical Cyclone Rapid Intensification*. *Weather Forecast.*, **30**, 1265–1279, doi:10.1175/waf-d-15-0024.1.

Appendices

Appendix A. Land Surface Model simulation

In order to justify deactivating the land surface model (LSM) in the experiments, a simulation with an active LSM was used. The LSM chosen was the NOAH LSM (Tewari et al. 2004) though the Stefan-Boltzmann was deactivated by setting the emissivity to 0 to prevent one-way radiation leakage not associated with the radiation parameterization. Other than the LSM, the settings described in Table 2 were applied to a BG-U0.2 surface with a vertically isothermal soil temperature profile over loam soil with a constant soil moisture profile. Figure 34 shows the maximum wind speed for all of the simulations including the LSM simulation. The LSM has a drastic effect on the maximum wind speed. This is a response to the sudden decrease in the mean enthalpy flux (Figure 35). Unlike the role of friction described in CHAPTER 2 THE INFLUENCE OF SOIL MOISTURE AND SURFACE ROUGHNESS ON AN IDEALIZED TROPICAL CYCLONE[1]there is a clear decrease in both latent heat flux (Figure 36) and precipitation (Figure 37). Interestingly, but not deserving of much discussion, the surface (skin temperature) did increase a small amount in the LSM simulation (Figure 38) due to the negative sensible heat flux (Figure 39), which was seen in all of the other uniform BG simulations. The increase in skin temperature due to a TC is more unrealistic than having a constant temperature. We argue that this is part of the justification for the deactivation of the LSM for the experiments in the theoretical treatment of this dissertation.

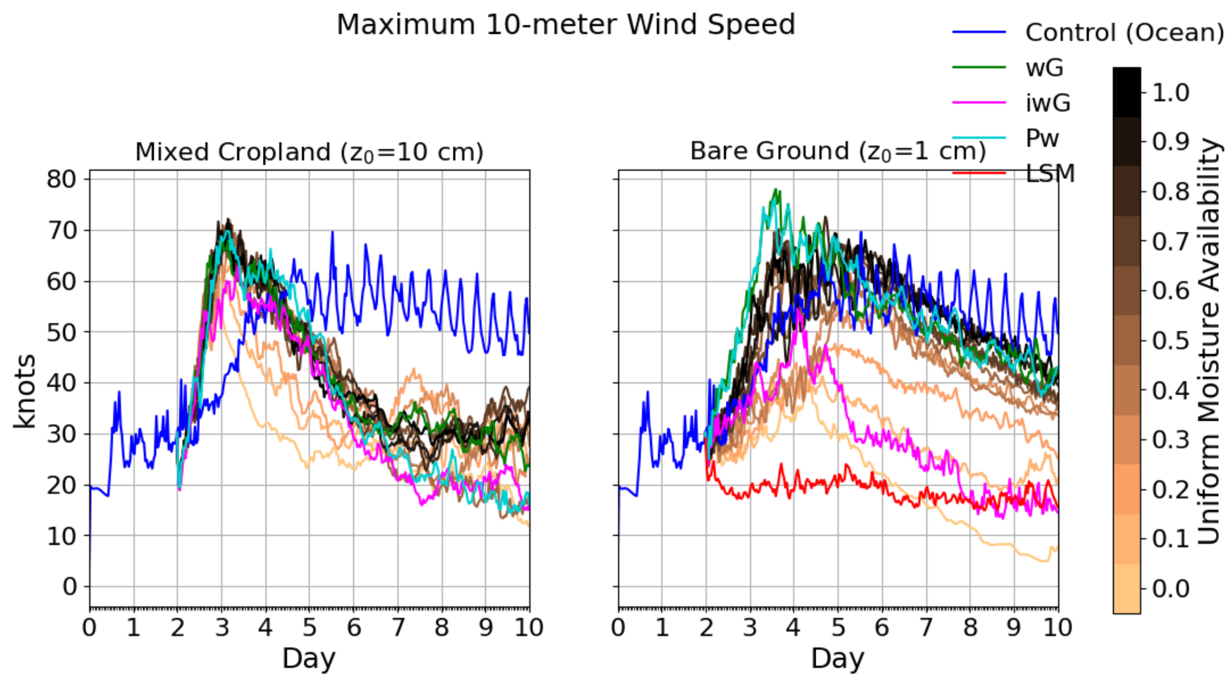

Figure 34: Maximum wind speed for all of the simulations, including the land surface model.

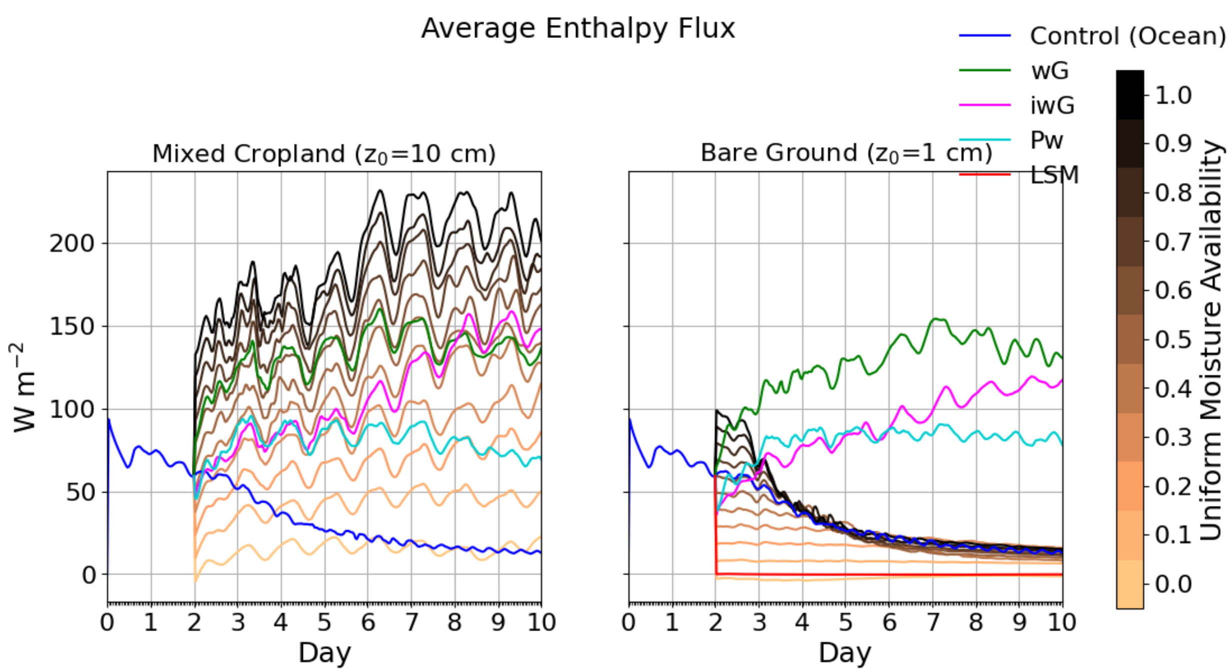

Figure 35: Mean enthalpy flux for all of the simulations, including the LSM simulation.

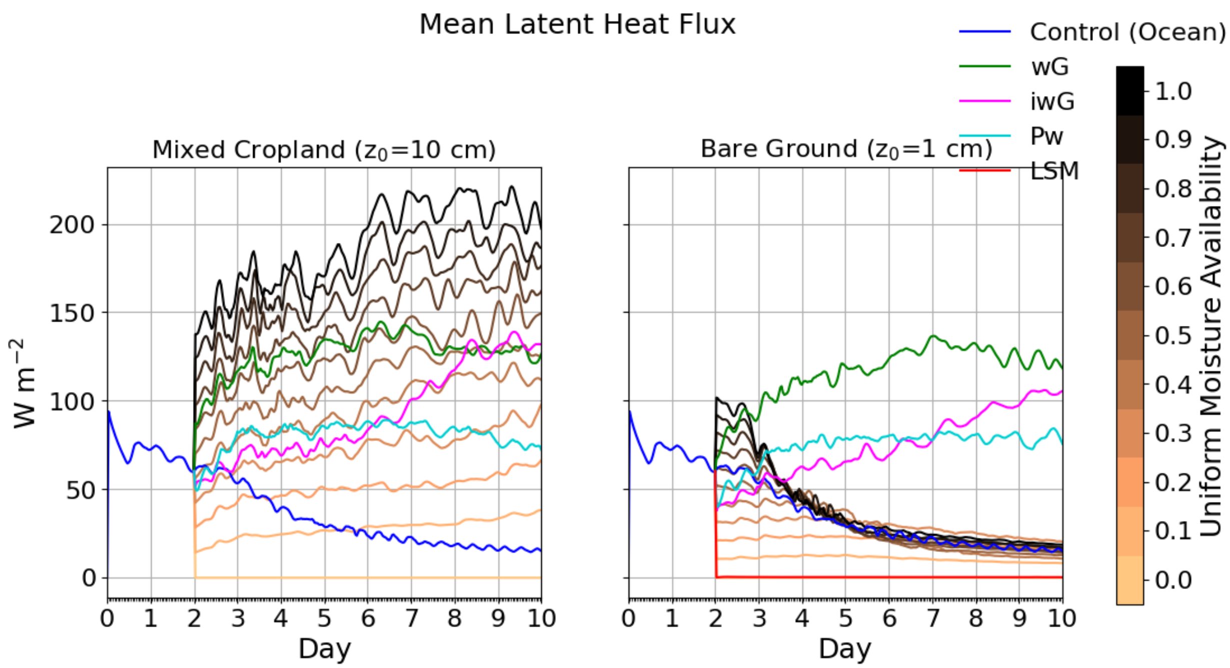

Figure 36: Mean latent heat flux for all of the simulations, including the LSM.

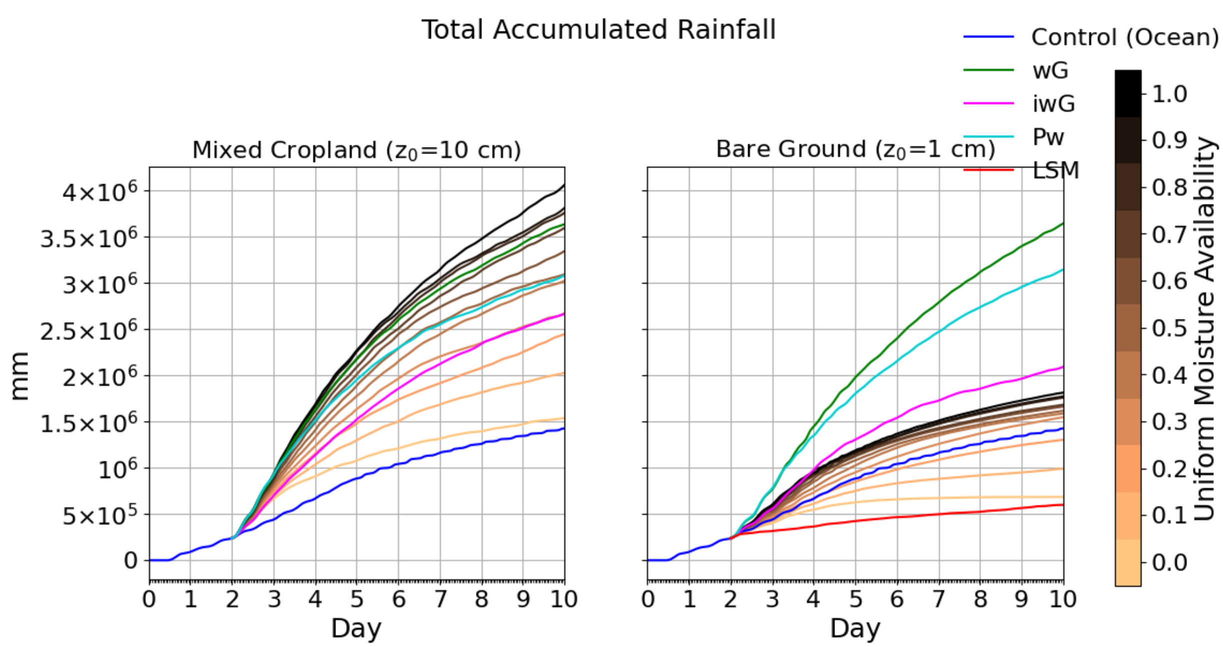

Figure 37: Total accumulated precipitation for all of the simulations, including the LSM.

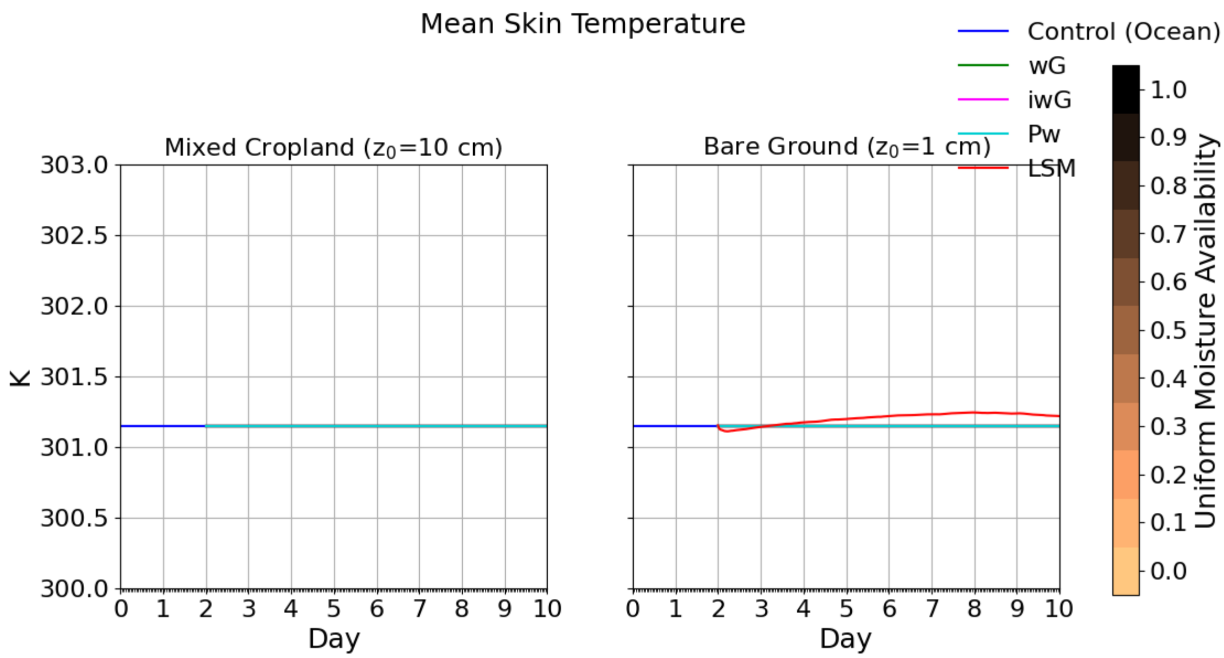

Figure 38: Mean skin temperature for all of the simulations, including the LSM simulation.

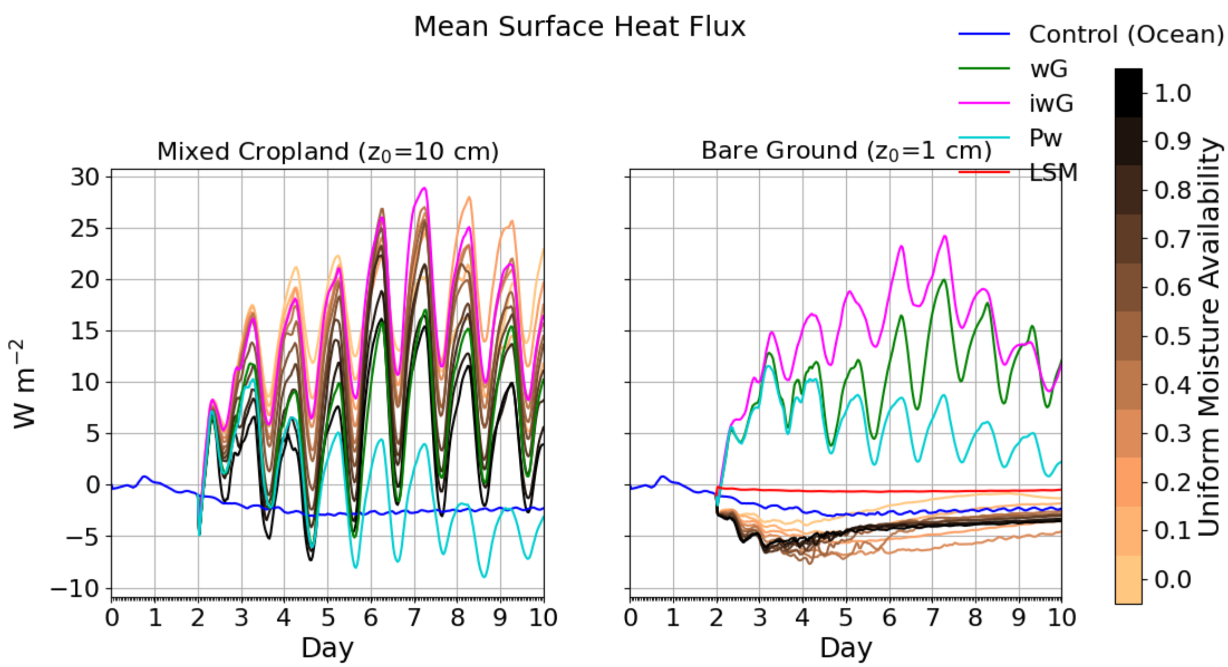

Figure 39: Surface sensible heat flux for all simulations, including the LSM simulation.

Appendix B. Derivation of Moisture Flux Sensitivity to Roughness Length

The kinematic moisture flux, $\overline{w'q'}$, is a function of z_0, by the way of

$$\overline{w'q'} = C_k U M \Delta q$$

where U is the near-surface wind speed, ρ is the air density, Δq is the difference between the atmospheric moisture and saturated moisture of the surface, and C_k is the roughness dependent enthalpy transfer coefficient. Considering that the enthalpy transfer coefficient and wind speed are

$$U = \frac{u_*}{k}\log\left(\frac{z_{ref}}{z_0}\right)$$

$$C_k = \left[\frac{k}{\log\left(\frac{z_{ref}}{z_0}\right)}\right]^2$$

the equation for $\overline{w'q'}$ may be written as

$$\overline{w'q'} = M\Delta q\,\frac{ku_*}{\log\left(\frac{z_{ref}}{z_0}\right)}$$

. Thus, the change of the moisture flux to changes in roughness length may be written as

$$\frac{\partial\overline{w'q'}}{\partial z_0} = \frac{M\Delta q k u_*}{z_0\left[\log\left(\frac{z_{ref}}{z_0}\right)\right]^2}$$

and rewritten as

$$\frac{\partial\overline{w'q'}}{\partial z_0} = \frac{\overline{w'q'}}{z_0\log\left(\frac{z_{ref}}{z_0}\right)}$$

. A more rigorous variation may be derived, but in addition to using the Businger-Dyer functions, a parameterization for the water vapor roughness length would need to be used.

Appendix C. Table of Tropical Cyclones that Underwent TCMI

Table 7: Tropical Cyclones that Underwent TCMI

Non-North Atlantic Storms	**North Atlantic Storms**

Season	Name	Number of TCMI events	Season	Name	Number of TCMI events
1981	EDDIE	17	1980	ALLEN	1
1984	FREDA	7	1982	CHRIS	2
1987	IRMA	6	1983	ALICIA	1
1989	KEN-LOLA:LOLA	12	1985	DANNY	13
1990	LOLA	1	1985	ELENA	6
1991	DAPHNE	14	1986	BONNIE	2
1995	BOBBY	3	1988	FLORENCE	3
1996	JACOB	1	1988	GILBERT	11
1996	KIRSTY	18	1989	CHANTAL	3
1996	ETHEL	12	1992	ANDREW	1
1996	HERB	4	1994	ALBERTO	10
1997	RACHEL	22	1994	BERYL	5
1997	AMBER	2	1995	DEAN	13
1999	BILLY	1	1995	ERIN	15
2000	ROSITA	2	1995	JERRY	3
2001	WINSOME	5	1996	FRAN	10
2001	ABIGAIL	2	1997	DANNY	12
2002	SINLAKU	1	1998	CHARLEY	2
2003	DELFINA	2	1998	FRANCES	2
2005	SANVU	1	1999	BRET	1
2007	GEORGE	1	1999	DENNIS	2
2007	JACOB	1	2001	BARRY	6
2008	NOT_NAMED	1	2002	ISIDORE	4
2010	LAURENCE	4	2003	BILL	6
2010	PHET	1	2003	CLAUDETTE	2
2010	GIRI	1	2003	GRACE	4
2011	YASI	20	2004	FRANCES	7
2018	HILDA	8	2004	IVAN	3
2018	KELVIN	2	2005	ARLENE	8
2018	YAGI	1	2005	DENNIS	45
			2005	KATRINA	2
			2005	RITA	2
			2007	ERIN	14
			2008	DOLLY	12
			2008	EDOUARD	1
			2008	FAY	3
			2008	GUSTAV	9
			2008	IKE	2
			2010	NOT_NAMED	3

			2010	HERMINE	11
			2012	ISAAC	5
			2015	BILL	17
			2017	CINDY	6
			2017	HARVEY	4
			2017	IRMA	5
			2018	ALBERTO	15
			2018	FLORENCE	2
			2018	GORDON	10
			2019	BARRY	3
			2020	AMANDA:CRISTOBAL	6
			2020	LAURA	5